NOVEL POLYMER TRANSPARENT ULTRASOUND TRANSDUCERS FOR

PHOTOACOUSTIC IMAGING APPLICATIONS

A Dissertation

by

HE HU

Submitted to the Office of Graduate and Professional Studies of
Texas A&M University
in partial fulfillment of the requirements for the degree of

DOCTOR OF PHILOSOPHY

Chair of Committee,	Jun Zou
Committee Members,	Chin Bing Su
	Jim Xiuquan Ji
	Javier A. Jo
Head of Department,	Miroslav M. Begovic

August 2016

Major Subject: Electrical Engineering

ABSTRACT

Recently, photoacoustic imaging has emerged as a new hybrid biomedical

imaging technique, which provides rich optical contrast information at deep ultrasound

penetration depth not achievable with conventional optical imaging techniques. It is

expected to find applications ranging from fundamental biological research to clinical

diagnosis. In photoacoustic imaging, short pulsed-laser illumination is used to generate

high-frequency and wide-band ultrasound waves (i.e., photoacoustic signals) inside the

imaging target to be detected by a single-element ultrasound transducer or a transducer

array. However, one fundamental issue in current photoacoustic imaging system design

is the opaque structure of the ultrasound transducer, which prevents effective and

efficient light delivery onto the imaging target and oftentimes results in lower imaging

performance and complex and bulky hardware configurations.

To address this issue, new optically-transparent polymer ultrasound transducer

and transducer array based on polyvinylidene fluoride (PVDF) have been investigated

and their applications in photoacoustic microscopy (PAM) and photoacoustic

tomography (PAT) have been demonstrated in this research. Specifically, two

microfabrication processes were developed for making transparent PVDF transducers

from solid bulk films and liquid precursors. The electrical properties of the transparent

PVDF transducers were studied. Impedance matching and amplification circuits were

designed accordingly to provide optimal photoacoustic signal conditioning and

acquistition. Based on the developed transparent PVDF single-element transducer and

transducer array, both PAM and PAT imaging experiment setups have been built, respectively. Their imaging performance, such as sensitivity, contrast, spatial resolution and penetration depth has been characterized with optical phantoms. Preliminary ex-vivo imaging experiments on animal tissues and in-vivo imaging experiments on live small animals have been conducted to demonstrate the feasibility of photoacoustic imaging based on optically-transparent ultrasound transducers. The experimental results show that using optically-transparent ultrasound transducers can significantly improve the light delivery efficiency and reduce the complexity of the imaging system, which will be especially useful for the clinical translation of photoacoustic imaging.

DEDICATION

To my parents

ACKNOWLEDGEMENTS

I would like to thank my committee chair and also my research advisor, Dr. Jun Zou, and my committee members, Drs. Su Chin, Jim Ji and Javier Jo, for their guidance and support throughout the course of this research.

Thanks also go to my friends and colleagues in the department for making my time at Texas A&M University a great experience.

Finally, thanks to my parents for their encouragement and supports through these years.

TABLE OF CONTENTS

LIST OF FIGURES

LIST OF TABLES

1. INTRODUCTION

1.1 Photoacoustic imaging technology

In the past 10 years, photoacoustic imaging has become one of fastest growing biomedical imaging techniques [1-7]. In photoacoustic imaging, non-ionizing laser pulses are delivered onto biological tissues, and a portion of the delivered energy will be absorbed by the tissues and converted into heat. The resulting transient thermoelastic expansion and wideband (up to tens of MHz) ultrasound emission can be detected with a single-element ultrasound transducer or a transducer array. The collected photoacoustic signals can be further analyzed for image reconstruction (Fig. 1.1) [8]. Photoacoustic imaging provides some unique advantages which cannot be achieved by conventional optical or ultrasound imaging. Compared with conventional optical imaging, photoacoustic imaging can achieve relatively large penetration depth. Compared with conventional ultrasound imaging, it can provide optical contrast information which cannot be obtained from acoustic imaging technologies. Recent studies have shown that photoacoustic imaging can be used for different applications, such as tumor angiogenesis monitoring, blood oxygenation mapping, functional brain imaging, skin melanoma detection, methemoglobin measuring, etc.[9].
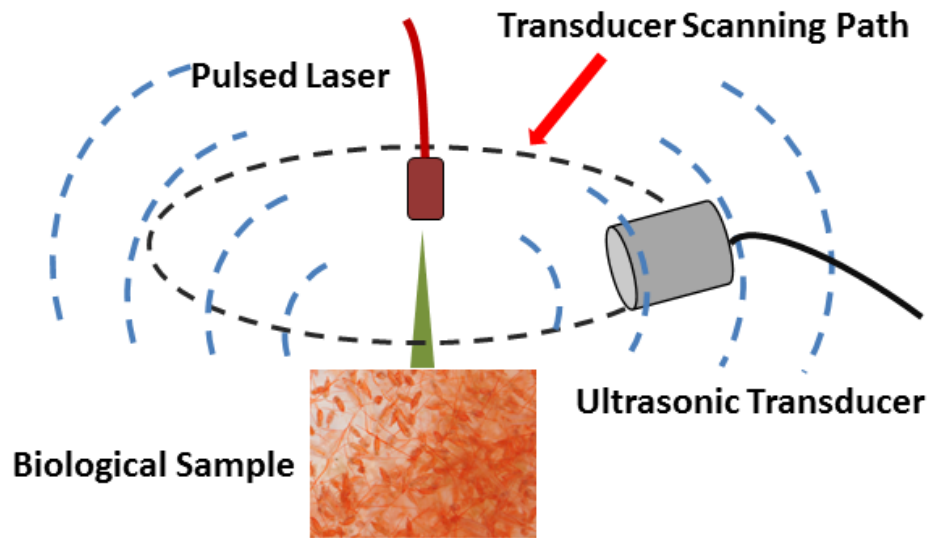
Fig. 1.1. Photoacoustic effect.

1.2 Current photoacoustic imaging techniques and systems

Due to the above unique advantages, many photoacoustic imaging systems have been developed. They can be divided into two types: photoacoustic microscopy (PAM) and photoacoustic tomography (PAT). The difference between these two is: the PAM system uses a focused ultrasound detector with 2D point-by-point scanning to collect the photoacoustic signals, so no imaging reconstruction is needed; while the PAT system uses an unfocused ultrasound detector (array) to receive the photoacoustic signals, and the final image is reconstructed by some special algorithm.

1.2.1 Current PAM systems

The development of PAM systems started from acoustic-resolution photoacoustic microscopy (AR-PAM) (Fig.1.2). A loosely focused pulsed laser beam is used to illuminate the imaging target (usually a biological sample). A focused ultrasound

2

transducer is used to collect the photoacoustic signals from the focal spot on the imaging

target. The lateral resolution of the photoacoustic images obtained from AR-PAM is

determined by the focal spot size of the ultrasound transducer. The imaging depth

depends on the focal depth of the transducer [10].
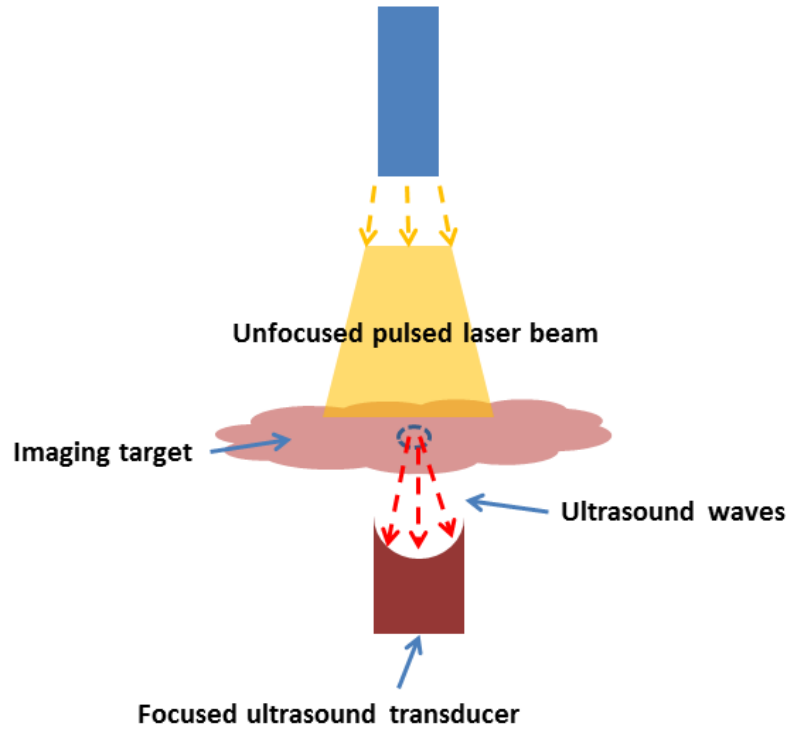
Fig. 1.2. Configuration of a typical AR-PAM system

Optical-resolution photoacoustic microscopy (OR-PAM) system (Fig. 1.3) was

developed based on AR-PAM. In an OR-PAM system, a focused pulsed laser beam is

used to illuminate the imaging target. The excited ultrasound waves are received by a

ultrasound transducer (focused or unfocused). The lateral resolution of the final

photoacoustic image is determined by the laser focal spot size which is usually much

smaller than that of an ultrasound transducer. Therefore, OR-PAM has a higher lateral

3

resolution than that of an AR-PAM [11-12]. However due to light scattering in biological tissues, the imaging depth of OR-PAM is less than that of AR-PAM.
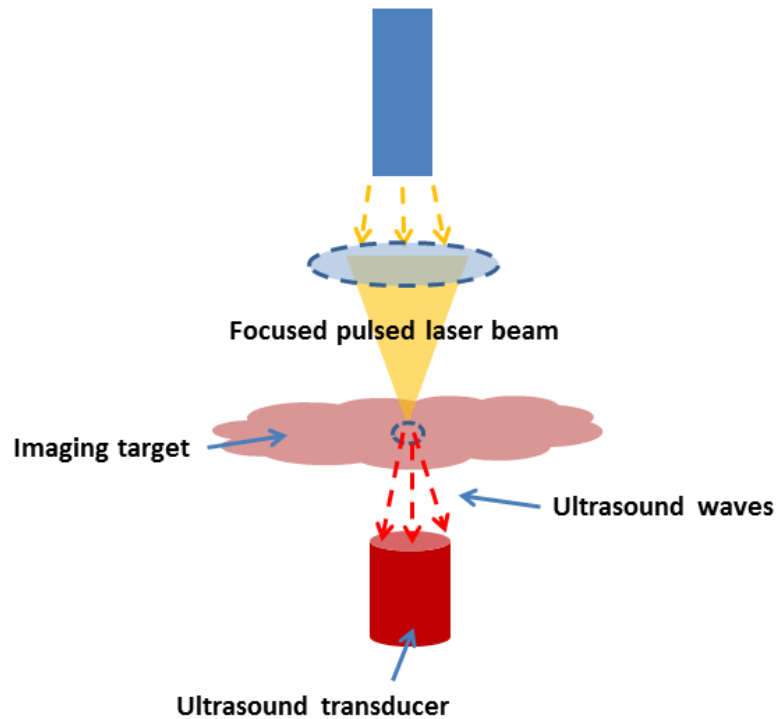
Fig. 1.3. Configuration of a typical OR-PAM system

1.2.2　Current PAT systems

　　In current development of PAT imaging systems, a popular configuration is shown in Fig. 1.4. It uses a linear scanning ultrasound transducer to receive the photoacoustic signals [13]. A single-element ultrasound transducer is mechanically scanned over the surface of the imaging target. And a pulsed laser beam is used to illuminate the imaging target and excite the photoacoustic waves. The transducer scanning path can also be a ring (Fig. 1.1) instead of a straight path.

4
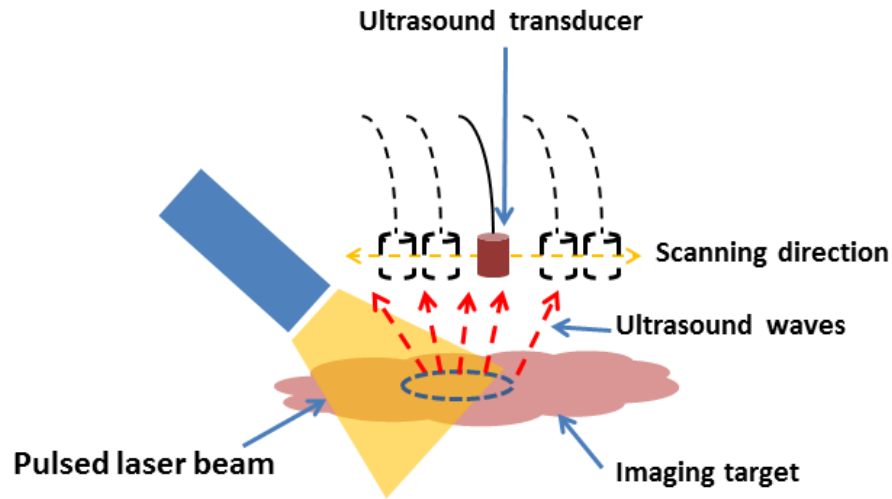
Fig. 1.4. Configuration of a mechanical scanning PAT imaging system.

Ultrasound transducer arrays have been widely used in ultrasound imaging field. Combining a straight or ring ultrasound transducer arrays with the pulse laser delivery system, the advantage of the PAT imaging system is that it avoids mechanical scanning for B-scan imaging. And for 3D imaging, only linear mechanical scanning is required. Therefore, the imaging speed is much faster than that of the raster scanning with a single element ultrasound transducer. Fig. 1.5 shows a whole body PAT imaging system using an ultrasound transducer ring array. The imaging target (a mouse body) was positioned in the ultrasound transducer ring array. The illumination laser was shot onto the mouse body and the excited photoacoustic signal was received by the transducer array. The ring array could move up and down to get the PAT images of different slices of the body. Then a 3D PAT image of the whole body could be reconstructed.
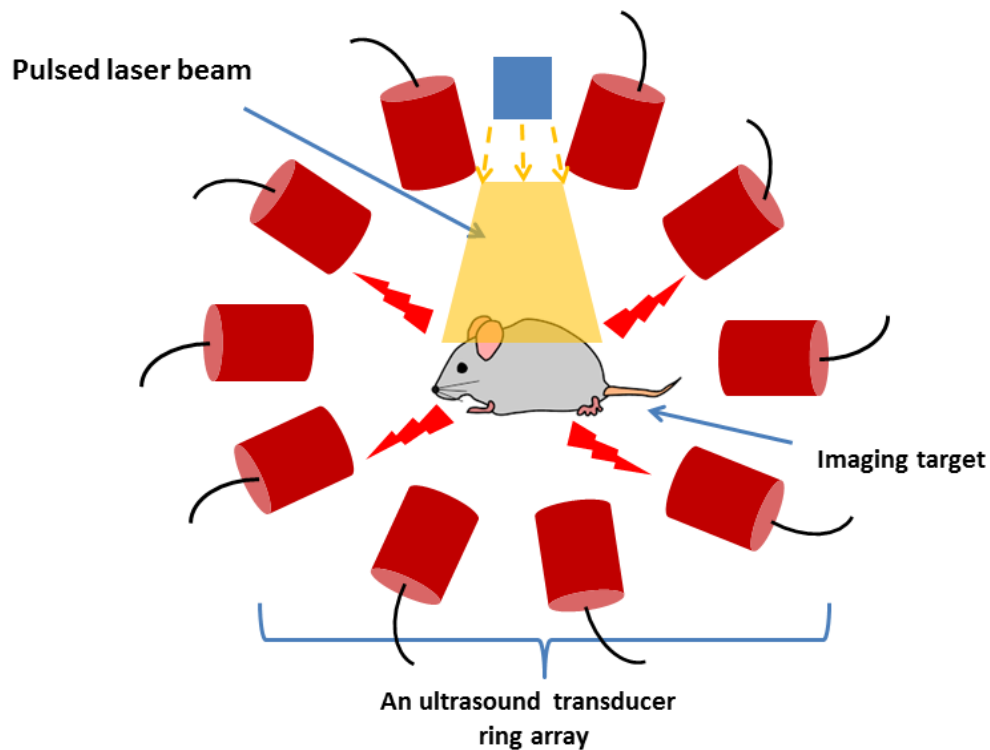
Fig. 1.5. Configuration of a PAT whole body imaging system using an ultrasound ring transducer array.

In a typical PAT imaging system [14] for handheld *in-vivo* biomedical studies, a pulse laser fiber bundle was aligned with a traditional ultrasound transducer array. Optical-fiber bundles are used to deliver the pulse laser (Fig. 1.6). Recently, researchers also came up with different simplified photoacoustic imaging system configurations. For example, J. Tang et al have developed a wearable PAT brain system using an ultrasound transducer ring array (Fig. 1.7) [15]. In this system, the ultrasound transducers are aligned in a ring pattern, and the excitation laser shoots through the ring to the imaging target. The photoacoustic signals are received by the transducer ring array.
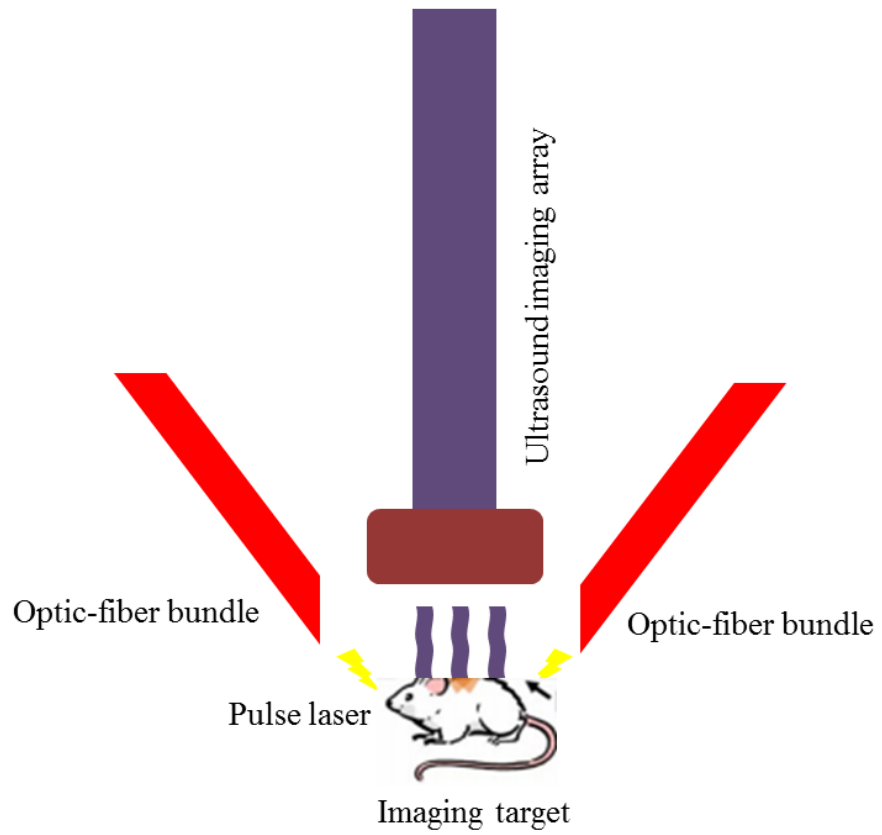
Fig. 1.6. Configuration of a PAT imaging system using a linear ultrasound transducer array.
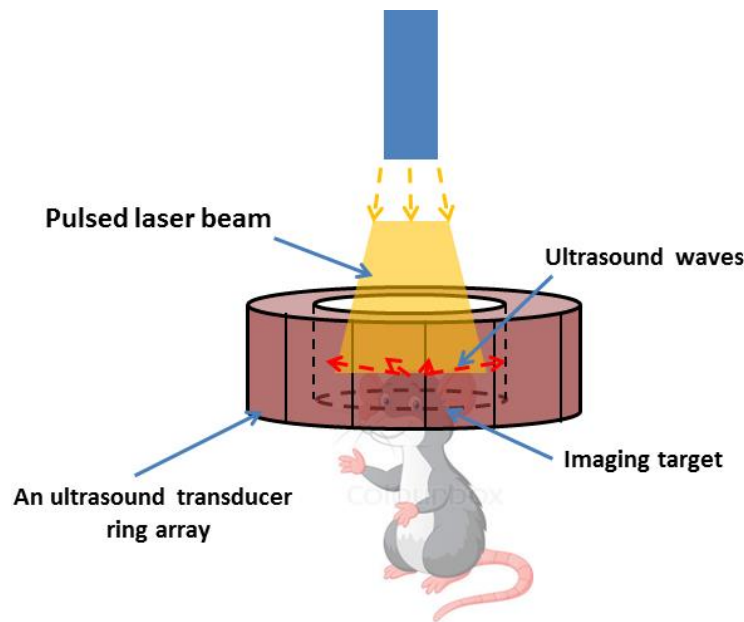
Fig. 1.7. Configuration of a PAT brain imaging system using an ultrasound ring transducer array.

1.3   Motivation

The current photoacoustic imaging systems have a common issue: the ultrasound transducers used in the systems are not optically transparent. Fig. 1.8 shows the imaging head configurations of three typical PAM systems. In the first configuration (Fig. 1.8(a)), the ultrasound transducer is positioned away from the laser focused spot so that it would not block the laser beam. In the second configuration (Fig. 1.8(b)), an optical prism is used to change the path of the pulsed laser so that the transducer could be fixed normally above the imaging target without blocking the laser path. In the third configuration (Fig. 1.8(c)), in stead of changing the laser path, acoustic prisms are used to change the path of the ultrasound waves. In this way, the situation is equivalent to that the ultrasound

transducer is put normally above the imaging target. Considering the above three

configurations, the current PAM systems' configurations are quite complex. It is mainly

due to the difficulty on assembling the excited laser system with the traditional

ultrasound transducers which are not optically transparent to the laser beams used in

photoacoustic imaging system. As a result, the excitation lasers could not shoot through

the ultrasound transducers to the imaging targets, which limits the excitation efficiency

and makes the system more complicated. For the current PAT systems, the same

problem exists. For example, in Fig. 1.5, the optical fiber bundles which deliver the

excitation pulsed laser to the target have to be positioned on both sides of the transducer

array.
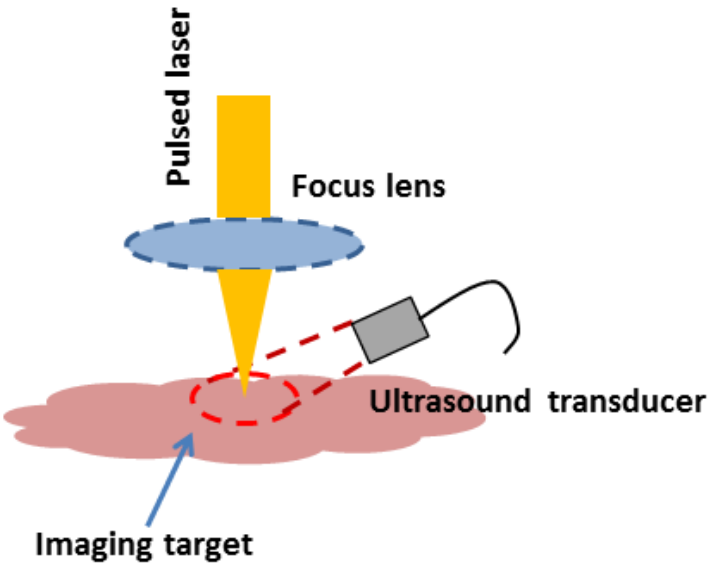
(a) PAM system 1;

Fig. 1.8. Three typical PAM imaging head configurations:(a)(b)(c).
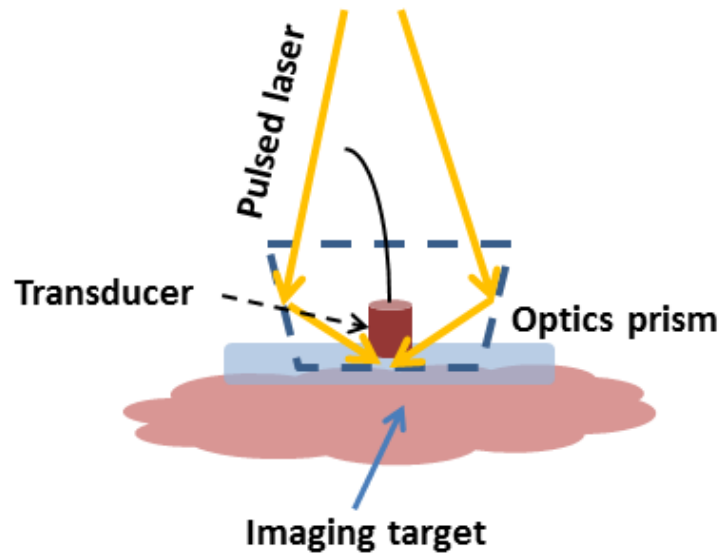
(b) PAM system 2;
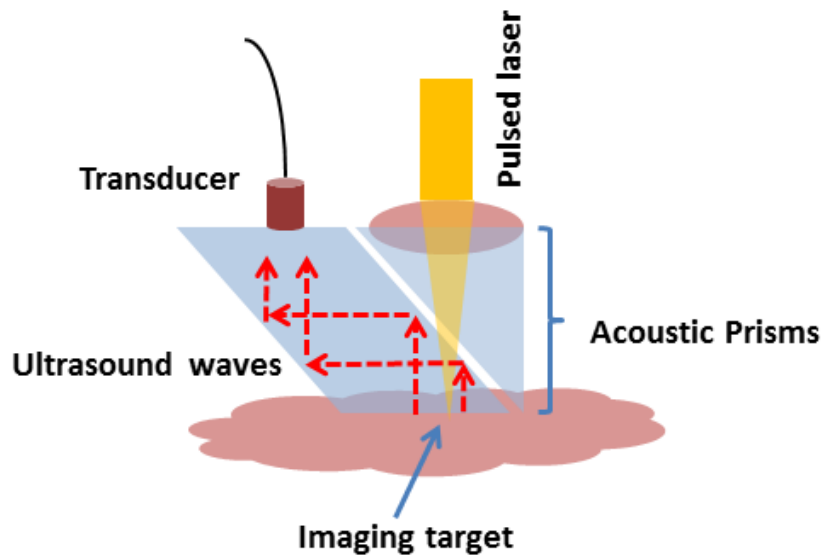
(c) PAM system 3;

Fig. 1.8. Continued.

This research focuses on developing a transparent ultrasound transducer that is suitable for being used in photoacoustic imaging systems. Such that the excitation laser pulse can directly transmit through the ultrasound transducer and reach the tissue surface at a normal incidence angle. This can increase the illumination efficiency and therefore detection sensitivity and penetration depth. Using the transparent ultrasound transducers, the photoacoustic imaging system will have a much simpler configuration, which will provide more opportunities for integrating the photoacoustic imaging technology into portable or wearable clinical devices.

1.4   Summary of work

In section 2, two microfabrication processes for making polymer transparent ultrasound transducers are presented. Current ultrasound transducer fabrication technologies are reviewed. Several types of popular piezoelectric materials for making transducers are compared for identifying suitable materials for developing transparent ultrasound transducers.

In section 3, the electrical signal conditioning and amplification interface between transparent transducers and the data acquisition system are introduced. Impedance matching methods are discussed. In order to improve the energy transmission efficiency and sensitivity of the ultrasound transducers, an efficient impedance matching network between the transparent transducer and the electronic amplification circuits was studied. The electronic properties of developed transducers were measured. Several impedance matching networks were analyzed and compared through circuit simulations.

After these studies, a pre-amplifier circuit with impedance matching network was built and tested.

In section 4, a photoacoustic microscopy (PAM) system using a single-element PVDF transparent ultrasound transducers is presented. To verify the feasibility of applying this system to photoacoustic microscopy techniques, both phantom and *in-vivo* imaging tests were conducted with this system. The imaging performance, such as spatial resolution, sensitivity uniformity and contrast were also evaluated.

In section 5, a PAT system using a 1D transparent PVDF ultrasound transducer array is presented. A special image processing and reconstruction method was developed for this PAT imaging system. Through phantom and *ex-vivo* imaging tests, the imaging performance of the PAT array imaging system were evaluated.

2. TRANSPARENT PVDF ULTRASOUND TRANSDUCER AND TRANSDUCER ARRAY

2.1   Introduction to piezoelectric ultrasound transducers

Piezoelectric materials have been widely used to make high frequency (>20 MHz) (HF) ultrasound transducers in different imaging applications, where high frequency ultrasound transducers with high resolution are needed. As an imaging technique that induces smallest damage to tested bodies or tissues, ultrasound imaging technology is suitable for inspecting human organs, such as skin, eye and vascular structure. However, the resolution of current ultrasound transducers becomes an issue when we want to get more detailed information about small structures in the body. The resolution of ultrasound image usually includes: the axial resolution (determined by the pulse width) and the lateral resolution (determined by the beam width). A rough estimation of these two parameters is shown below:

$$\text{Axial resolution: AR} = \frac{c}{2f_c BW} \ (2.1)$$

$$\text{Lateral resolution: LR} = F\frac{c}{f_c} \ (2.2)$$

In the above two equations, c is the speed of the ultrasound in the medium, BW is the bandwidth of the transducer, f_c is the center frequency of the transducer, λ is the wavelength of the ultrasound wave. F is the F-number which is the ratio of the focal distance to the aperture dimension. From the above two equations it can be shown that an increase in the central frequency of the transducer will improve both the lateral and

the axial resolution of the ultrasound image. An example is given in [16]: if the frequency of the transducer is increased to 50MHz and the F is 1.9, bandwidth of 60%, the axial and lateral resolution can reach 25 μm. And the depth of the penetration for most tissues would be 8~9 mm at 50 MHz.

In case of photoacoustic imaging, the resolutions of the image are also determined by the frequency of the ultrasound transducers in the similar fashion. Therefore, many techniques and methods have been developed to produce ultrasound transducers with higher frequencies.

2.2   Comparison of commonly used piezoelectric materials

Since the goal of this research is to develop a transparent ultrasound transducer, first the active material used in this transducer should have an excellent optical tranmission rate within the pulse laser wavelength range. Current ultrasound transducers usually employ the lead zirconate titanate (PZT) as the active element. PZT has very good piezoelectric properties, which however is not optically transparent. In recent years, $LiNbO_3$ (LNO) has become a new substitute piezoelectric material for ultrasound transducers. It not only has very good piezoelectric properties but also a good transparency to the visible light, which makes it widely used in both ultrasond and optics research fields.

Q. F. Zhou et al. have proposed two methods for designing HF ultrasound transducers. In [17], an HF ultrasound transducer based on LNO inversion layer has been developed. The thickness of the active element is about 100 μm. Test results demonstrated that the central frequency of this transducer was about 50-60 MHz. They

also proposed in [18] that an HF transducer could be built based on PZT films on the silicon substrates. In this method, sol-gel PZT solutions were spin-coated on silicon substrates to form a 30 μm thick film. And then the films were annealed at 750℃ by a rapid thermal annealing (RTA) process. The test results showed that a lateral resolution of 33 μm could be achieved. And the central frequency of the transducer could reach 103 MHz.

LNO and PZT are two piezoelectric materials commonly used in making ultrasound transducers. But the microfabrication process is usually very complicated for these two types of materials. H. Guo et al. have developed a broadband graded ultrasound transducer [19] which used graded piezoelectric $PbTiO_3$ ceramics as the active element in the transducer. The advantage of this material is that the manufacture process becomes simpler and more effective. And in addition, the bandwidth of this transducer reached 92 % while the typical value is only 56 % for HF transducers based on other techniques.

$[Pb(Mg_{1/3}Nb_{2/3})O_3]_{0.63}[PbTiO_3]_{0.37}$ (PMN-PT) is another popular piezoelectric material used for making HF ultrasound transducers in recent years. X. Li et al developed a 80 MHz intravascular ultrasound transducer [20] based on PMN-PT free-standing film. The fabrication method was a precursor coating based approach. The final bandwidth was about 65%.

Another potential candidate material is the transparent piezoelectric polymer material, such as, polyvinylidene fluoride (PVDF). While other materials, like nylon and PVC exhibit the effect, none are as highly piezoelectric as PVDF and its copolymers.

15

Like some other poly(vinyl chloride) (PVC) ferroelectric materials, PVDF is also

pyroelectric, producing electrical charge in response to a change in temperature. PVDF

strongly absorbs infrared energy in the 7-20 μm wavelengths, while in the visible light

region and near infrared region, it is highly transparent (around 80%) (Fig. 2.1). Tables

2.1 and 2.2 list the major properties of PVDF and two popular piezoelectric ceramic

materials.
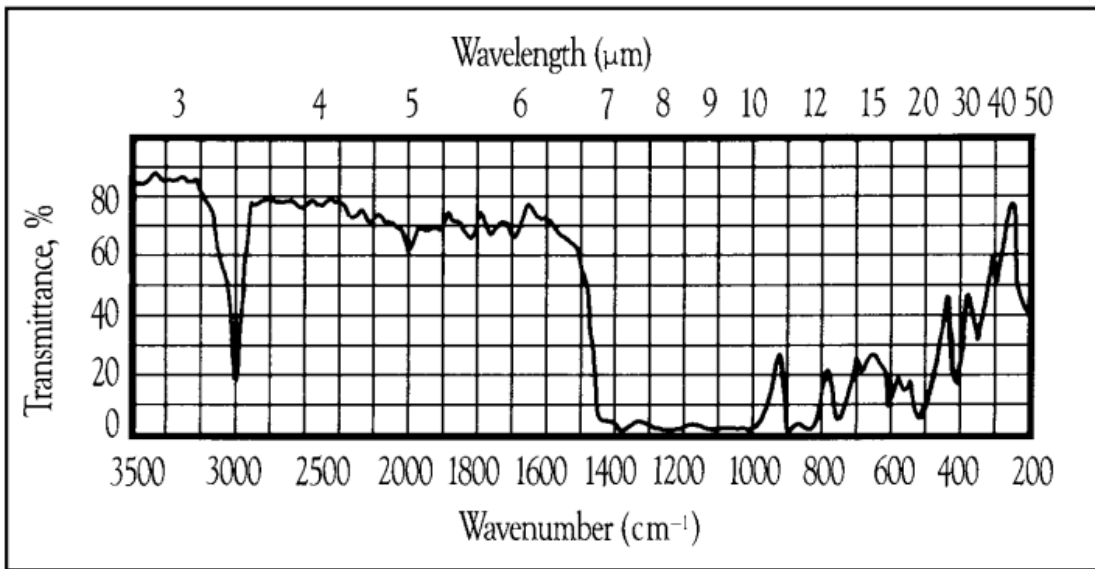
Fig. 2.1. Typical abosorption spectrum of PVDF [21].

Table 2.1. Comparison of piezoelectric materials.

Property	Units	PVDF Film	PZT	BaTiO$_3$
Density	$10^3 kg/m^3$	1.78	7.5	5.7
Relative Permittivity	$\varepsilon/\varepsilon_0$	12	1200	1700
d_{33} constant	$(10^{-12})C/N$	33	374	160
k_{33} constant	% at 1 KHz	12	70.5	85
Acoustic Impedance	$(10^6)kg/m^2 \cdot sec$	2.7	30	30

From Table 2.1, the advantages and limitations of PVDF over the popular piezoelectric materials are clearly shown. One major advantage of PVDF over piezo ceramic is that its acoustic impedance is much closer to that of water [$1.48 \times (10^6)kg/m^2 \cdot sec$] , human tissue [$1.68 \times (10^6)kg/m^2 \cdot sec$] ,and other organic materials. The acoustic impedance of piezo film is only about 2.6 times that of water, whereas piezo ceramics are typically 11 times greater. So the acoustic energy's transmission rate is much higher across the PVDF-water interface. It can be 2.63 times higher than the energy transmission rate across PZT-water interface. Thus, a close impedance match permits more efficient transduction of acoustic signals from transducer to the surrounding medium, like water.

Table 2.2. Physical property comparison of LNO and PVDF.

Property	Units	PVDF Film	36° rotated Y-cut LN
Density	kg/m^3	1.78	4.65
Relative Permittivity	$\varepsilon/\varepsilon_0$	12	28.7
d_{33} constant	$(10^{-12})C/N$	-33	6
g_{33} constant	$(10^{-3})Vm/N$	-330	2.3
Electromechanical Coupling Factor k_t	%	14	48.5
Transmission Range (Wavelength)	μm	0.4-6.5	0.4-5.0
Acoustic Impedance	$(10^6)kg/m^2 \cdot sec$	2.7	34.1

Compared with LNO, the benefits of using PVDF as the active element of the transducer is that it has higher piezo constants and also its acoustic impedance is much close to that of water. The advantage of LNO over PVDF lies in that it has a higher electromechanical coupling factor, which enables more electric charge energy to transform to mechanical vibration energy. Both of them have good transparency in the laser's wavelength range which is usually from 0.4μm to 1.5μm. Since one goal of this research is to simplify the traditional photoacoustic imaging system, PVDF is choosen to work as the piezoelectric element material used in the transparent transducer. Because its acoustic impedance value close to that of water, no complex matching and backing layer will be needed.

Developing HF ultrasound transducers using PVDF as the active element materials has a long history. M.D. Sherar et al. proposed a model called Krimholtz-Leedom-Matthei (KLM) model [22] for designing PVDF ultrasound transducers

operating in the 100MHz range. However, one drawback of PVDF is that its low

thickness mode coupling coefficient (k_T) which is between 0.1 and 0.2. The consequence

is that PVDF transducers have very poor sensitivity if their design is not optimized. The

KLM model shows a good predication on the PVDF transducers' performance when

they work over the frequency range from 40 MHz to 140 MHz. To compare the

advantages and disadvantages of different materials used as the active element materials

for making high frequency transducers, the major performance specs of a few

transducers made with different materials are listed in Table 2.3.

Table 2.3. Characteristics of ultrasound transducers made of different piezoelectric

materials.

Materials	Insertion loss (dB)	Central frequency (MHz)	Bandwidth (MHz)
$PbTiO_3$	18.0	63	16.9
Fiber Composite	17.4	52	26.9
LNO	20.1	60	30.5
PVDF	31.0	54	47.9

(The data are simulated results based on the KLM model.)

A detailed comparison between the theoretical simulation and measured results is

provided by K. A. Snook et al [23]. It can be seen that PVDF-based transducers have

low electromechanical coupling efficient and high insertion loss. For transducers made

of LNO or $PbTiO_3$, their sensitivity is higher. However, their acoustic impedance is

much different from media like water. Thus, more complex configuration is needed to

build transducers using these materials. The bandwidth of transducers made of PVDF is wider than others.

2.3   PVDF-based ultrasound transducer development

PVDF, as a type of semicrystalline polymers with at least four crystalline phases, is well-known for its piezoelectric properties. The four crystalline phases include nonpolar α-phase, polar β-phase, polar γ-phase and so on. When PVDF cools down from the melt, the crystalline is the nonpolar α-phase. In order to get the polar β-phase PVDF film, a poling process is necessary. Y. J. Park et al. have studied PVDF microfabrication and micromolding methods using different solvents [24], which provides a good foundation for developing integrated PVDF sensors.

Working as the active element in an ultrasound transducer, PVDF films have many advantages which make it different from the traditional piezoelectric materials used in transducers. Novel types of PVDF ultrasound transducers have been developed based on these special properties.

First, PVDF film is an ideal material for making focused ultrasound transducers. For ultrasound related imaging applications, focused ultrasound transducers can provide a higher lateral resolution. However, it is costly and complicated to make a focused transducer using the PZT material as the active element. Usually, an acoustic lens is employed in front of the active element to focus the acoustic energy, which makes the configuration of the ultrasound transducer even more complicated. PVDF has the following advantages which make it a suitable piezoelectric material for making focused ultrasound transducers: 1) its flexibility allows the material to be easily conformed to a

spherical shape; 2) its low acoustic impedance creates a good matching conditions to both the backing material and the coupling medium. A line-focus ultrasound transducer was built based on PVDF films[25]. In this design, the line-focus transudcer was made by bending a PVDF film onto a cylindrical concave surface. And then the backing materials were added. In this way, the desired focal length could be controlled by using different sizes of cylindrical tubes or rods.

The second application of PVDF is to make integrated ultrasound transducers. The thickness of PVDF films used for making ultrasound transducers is usually at the micrometer level, which is the dimension of the most semiconductor devices. And also PVDF related microfabrication methods have been developed and optimized for different applications. Therefore, integrated ultrasound transducers which combine both PVDF piezoelectric films and field-effect transistors are being developed and have already proved useful in many application fields.

In the integrated PVDF ultrasound transducers, the low sensitivity is a problem. X. R. Zheng et al. have develped an improved sensitivity integrated PVDF ultrasound sensor [26]. In this sensor, the gate electrode of the field-effect transistor was placed over an isolated epitaxial region, and a polymide film was used to pad the extended gate electrode. This structure decreased the gate capacitance and increased the sensitivity of the transducer. According to the test results, a sensivtivity improvement of over 13 dB was achieved as compared with the normal piezoelectric-oxide-semiconductor field-effect transistor.

The third application of PVDF on the ultrasound transducer development is to make transducer arrays. Ultrasound transducer arrays are popular in the medical imaging field. With the success of the integrated PVDF sensors, different types of PVDF ultrasound transducer arrays are being developed. Y. Wang et al. have developed a PVDF sensor array[27] directly on a 25 μm thick aluminum-metalized polarized PVDF film using a laser micro-machining technique. The response time of this sensor array reached 31 ns which was much faster than similar sensors. S. Lee et al. also developed a laser machining method [28] of PVDF based piezoelectric films for microsensors and micro-electro-mechanical systems (MEMS).

2.4   Fabrication of single-element transparent PVDF ultrasound transducer

Two microfabrication methods have been developed for making single-element transparent ultrasound transducers based on PVDF. They started with different raw materials.

2.4.1   Fabrication process based on pre-fabricated piezoelectric PVDF films

In piezoelectric PVDF films, most of the electric dipoles' orient along certain direction. When external mechanical stress or forces are applied onto these films, charges will accumulate on the two surfaces. If an external monitoring circuit is connected to the two surfaces, a piezoelectric voltage signal will be detected. It is also a mechanical energy to electric energy transformation process, which happens in all piezoelectric materials. Two types of pre-fabricated piezoelectric PVDF films were obtained from two providers separately: 28μm thick PVDF film from Measurement

Specialties Inc. (Hampton, VA, United States) and 9μm thick one from Piezotech S.A.S

(Pierre-Benite Cedex, France). Major properties of these two films are listed in Table 2.4.

Table 2.4. Comparison of two types of PVDF piezoelectric films.

	Property	Unit	Value
28μm thick PVDF film from Measurement Specialties Inc.	Piezoelectric strength constant, d_{33}	pC/N	13.5
	Electromechanic coupling factor K_T	%	17
	Acoustic impedance	$(10^6)kg/m^2 \cdot sec$	4.2
	Speed of sound	m/s	2300
9μm thick PVDF film from Piezotech S.A.S	Piezoelectric strength constant, d_{33}	pC/N	16
	Electromechanic coupling factor K_T	%	10 to 15
	Acoustic impedance	$(10^6)kg/m^2 \cdot sec$	2.5
	Speed of sound	m/s	1400

The material of the electrodes is ITO, which is a transparent conductive dielectric material commonly used in solar cells.

The fabrication process is shown in the following diagram (Fig. 2.2): 1. the process started from a poled PVDF film. It was cut into pieces of suitable sizes. 2. In order to define the regions for ITO electrodes, shadow masks were prepared. The PVDF film was sandwiched between two shadow masks. 3. Through RF sputtering process, the ITO electrodes were formed on the two surfaces of the PVDF film. 4. The second group of shadow masks for forming the metal electrode were used to sandwich the PVDF film. 5. Though DC sputtering process, the metal electrodes were formed on the surfaces of the PVDF film. 6. After step 5, a free-standing transparent ultrasound transducer was generated. Finally, the film was laminated on the surface of a glass substrate using a small droplet of epoxy.
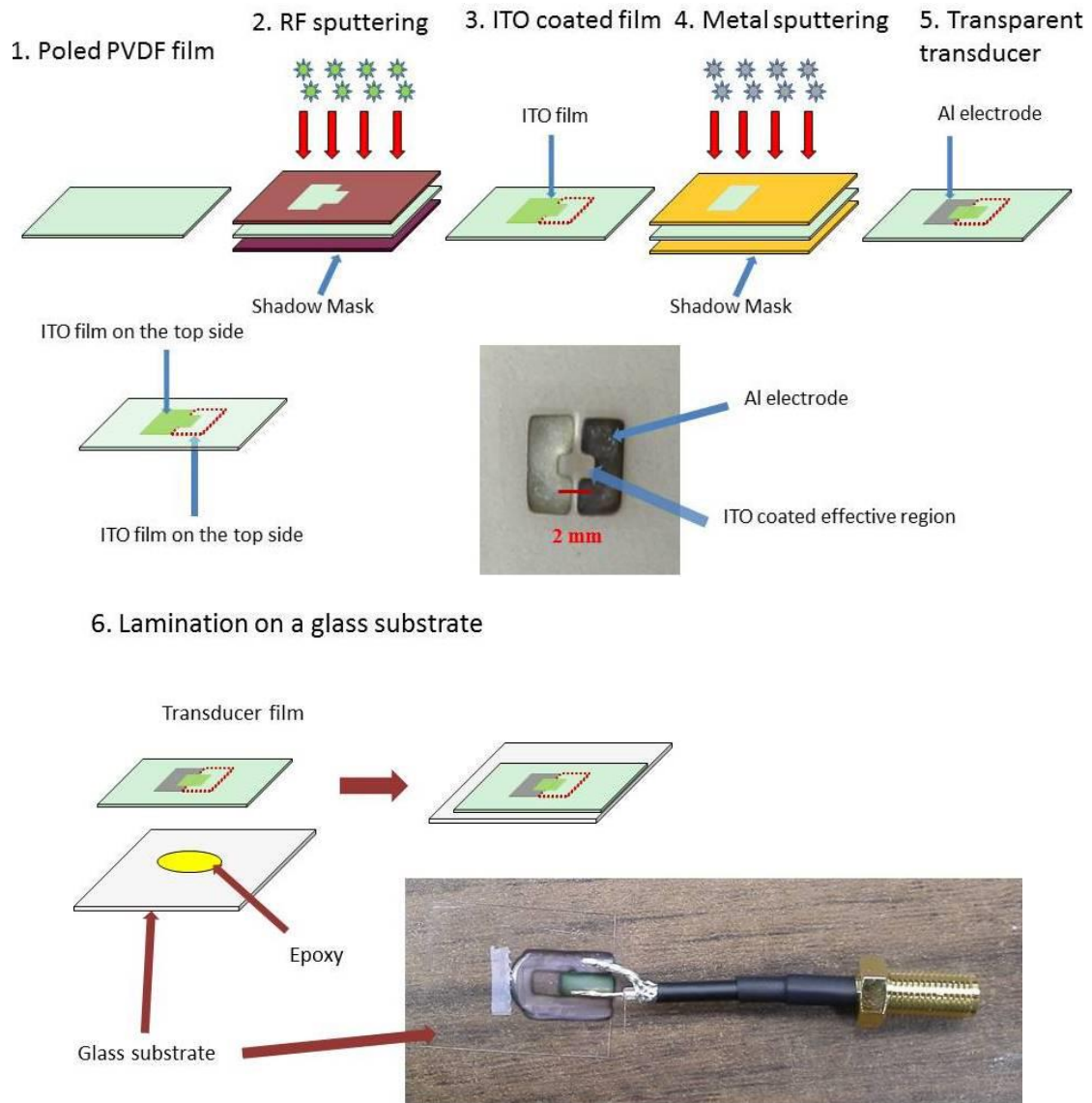
Fig. 2.2. Fabrication process of transparent ultrasound transducers based on PVDF

piezoelectric films.

The transmission coefficient of the transparent PVDF transducer film is shown in

Fig. 2.3. It can be seen that after coating ITO electrode layers to the PVDF film, its

optical transmission rate over the wavelength range (0.4μm to 1.4μm) is still above 70%.
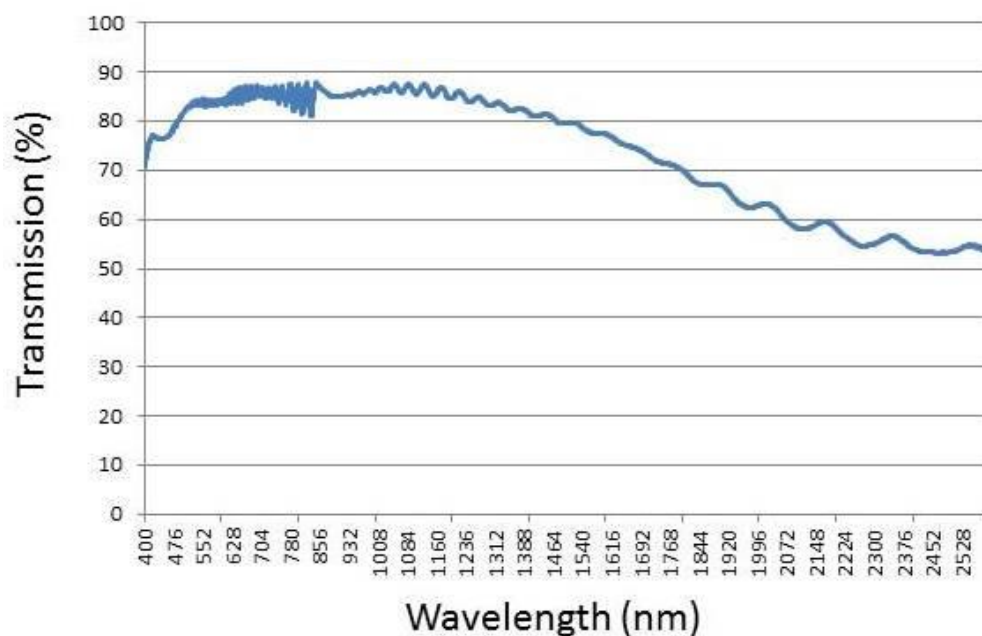
Fig. 2.3. Transmission ratio of the microfabricated PVDF ultrasound transducer.

Through this method, a high quality transparent ultrasound transducer was made. However, two issues still remain: 1. Thickness of the final film is fixed, which depends on the thickness of the original PVDF film. Therefore, the resonant frequency of the final transducer cannot be controlled in the fabrication process. 2. It is hard to integrate the transducers fabricated through this method into Lab-on-a-chip devices. Therefore, to solve the above problems, a second fabrication method using PVDF precursor was developed.

2.4.2   Fabrication process based on PVDF precursor

In this method, the fabrication process started from the PVDF precursor powder (Sigma-Aldrich, St. Louis, MO) (Fig. 2.4): 1. PVDF powder was dissolved in the N,N-Dimethylformanide (DMF) solvent. The weight ratio of the solution was 2.0%. 2. A

26

glass substrate was coated by ITO electrode. Then the mixture solution was spin-coated on this glass substrate. 3. Through the drying process in a hot oven, a thin PVDF film was formed on the surface of the glass substrate. 4. After forming the PVDF film on the glass substrate, the top electrodes were deposited onto the PVDF film through the sputtering process. (Fig. 2.5) 5. The PVDF film was poled by applying a strong electric field to the film for 8−10 hours (Fig. 2.6).
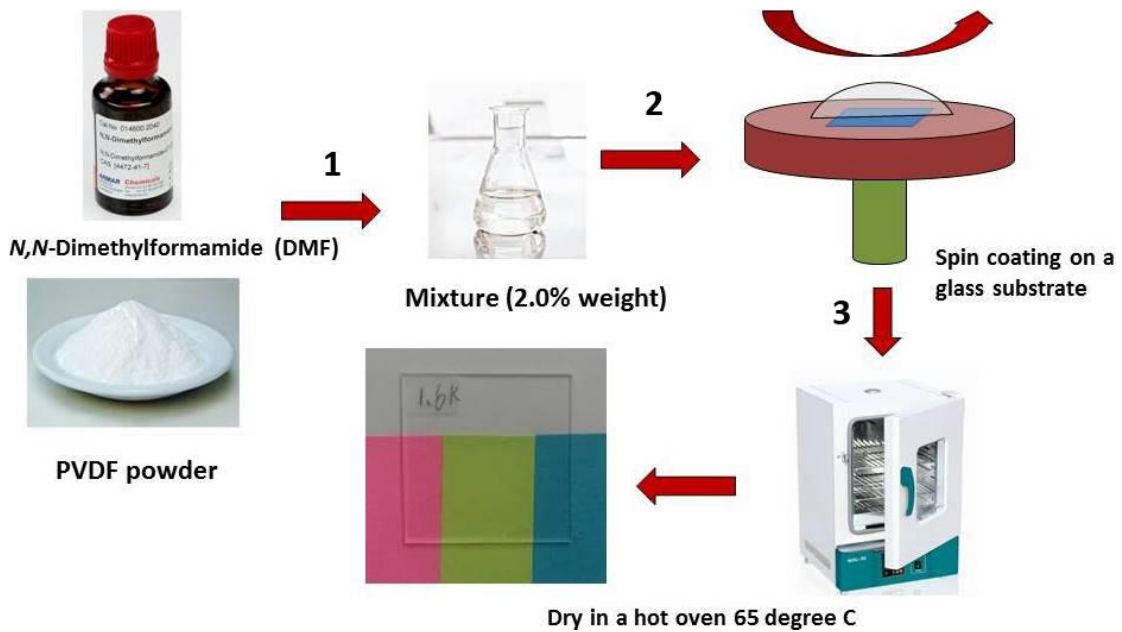
Fig. 2.4. PVDF film fabrication process starting from PVDF precursor
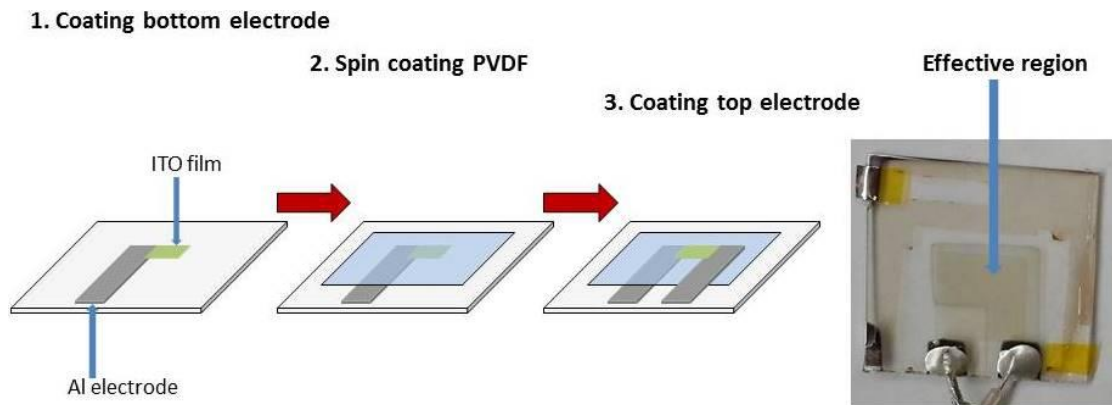
Fig. 2.5. Electrodes fabrication process
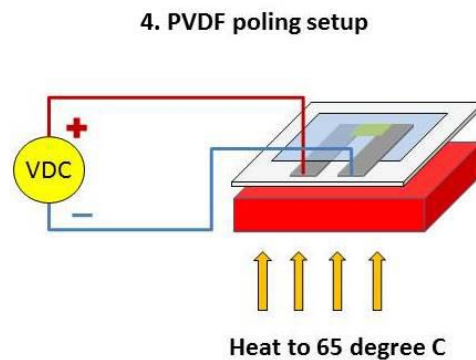
Fig. 2.6. PVDF poling process

In this method, the thickness of the final transducer can be controlled. The spin speed in the spin coating step determines the thickness of the PVDF film. Therefore, the resonant frequency of the final transducer can be controlled.

The spin speed in the spin coating step was characterized. Since the thickness of the final PVDF film determines the resonant frequency of the transducer, the spin speed should be well-controlled. Here, 1.1 g PVDF powder was mixed with 10 mL DMF

solvent. Then the mixture was poured onto the surface of the glass slides (2.5 cm by 2.5 cm). Next, the glass slides were spinned at different speeds. The spin speed profiles were shown in Fig. 2.7. First, the spin speed was increased to the spread speed, and after 10s the speed was increased to the final spin speed and held for 30s. After spin coating, the glass slides were baked in 65℃ oven. After the PVDF films were formed on the surface of the glass slides, the thickness of the films was measured. The thickness of the final PVDF films is listed in Table 2.5.
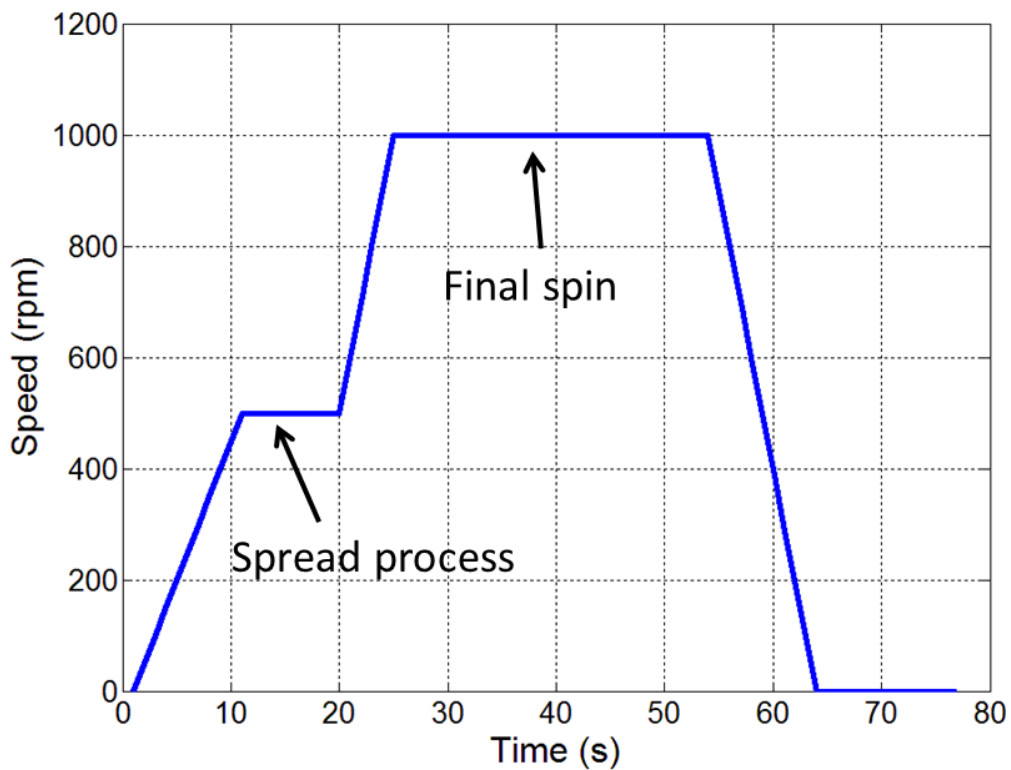
Fig. 2.7. Spin coating speed profile.

Table 2.5. The thickness of PVDF films using different spin coating speeds.

Spread speed(rpm)	Spin speed(rpm)	Final thickness (µm)
500	800	3.0
500	1000	2.0
500	1200	1.2
500	1400	1.1
500	1600	1.0

2.4.3   PVDF poling methods

The piezoelectric properties of the materials come from the induced polarization. In the α-phase PVDF film, the dipoles orient along different directions. In order to induce the piezoelectric property to the film, the PVDF film needs to be polarized. The polarization is usually conducted at higher temperatures through a strong electric field. Then the temperature is lowered to in the presence of the electric field so that the domains in the PVDF film are maintained in the polarized state. There are two commonly used poling methods on poling PVDF films: the corona poling and the electrode poling.

The setup of the corona poling setup is shown in Fig. 2.8. At the bottom of the setup there is a heating plate which can control the temperature of the setup and heat the film when the poling happens. On the top of the beating plate there is the electrode which is connected to the anode of the voltage source. The film to be poled is attached to the surface of the bottom electrode (cathode). Over the PVDF film, there is a metallic grid which is used to control the magnitude of the poling electric field. A corona tip

(usually a needle) is placed over the grid and connected to the cathode of the corona

voltage source (8-10kV).
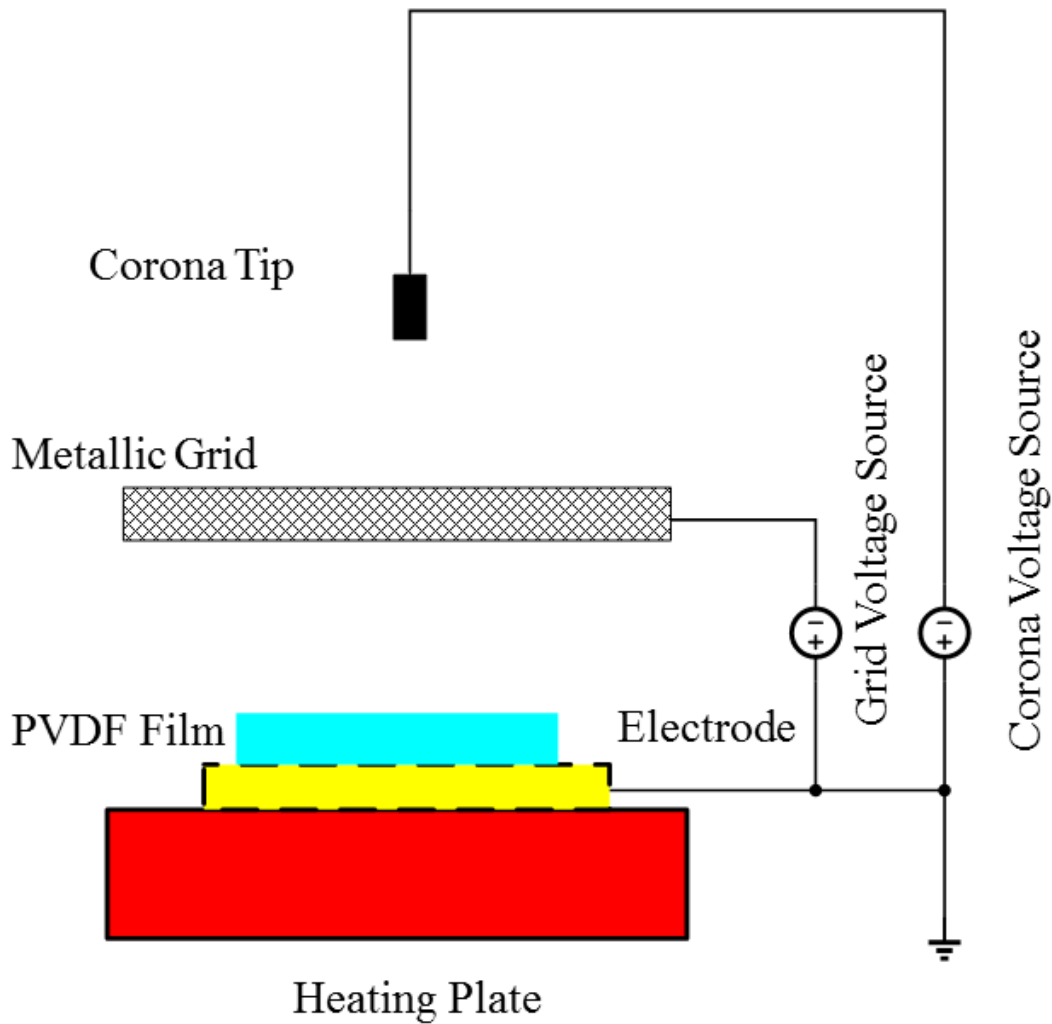
Fig. 2.8. Corona poling setup.

When the poling process is conducted, the corona tip discharges, and the dry air

around the tip is ionized. The ionized particles are accelerated to the ground which is the

bottom electrode of the PVDF film. However, the ionized flow is blocked by the PVDF film. And the charges of the ionized flow accumulate on the surface of the PVDF film. Then an electric field is generated between the deposited charges and the bottom electrode layer. The PVDF film is poled in this field. The amount of the deposited charge is controlled by the metallic grid, which also determines the magnitude of the poling electric field. The advantage of corona poling is that a large area film could be poled without using a big area electrode. The disadvantage is that the setup is relatively complicated and requires optimization.

The most popular poling method is the electrode poling. The setup is shown in Fig. 2.9. First, the whole system is immersed in insulating fluid in the heating system. Before that, the PVDF film to be poled will be first coated by conducting electrode layers on both sides of the film, for instance, 100 nm aluminum layers. The coating methods can be evaporation, sputtering and so on. The electrodes are connected to the voltage source. Since there may be arc generation during the poling process, the whole setup is immersed in the insulating fluid. A good contact of the electrodes to the PVDF film is necessary. The poor contact may lead to the non-uniformity of the poling electric field or the dielectric breakdown at some points. The advantage of this system is that the setup is relatively simple.
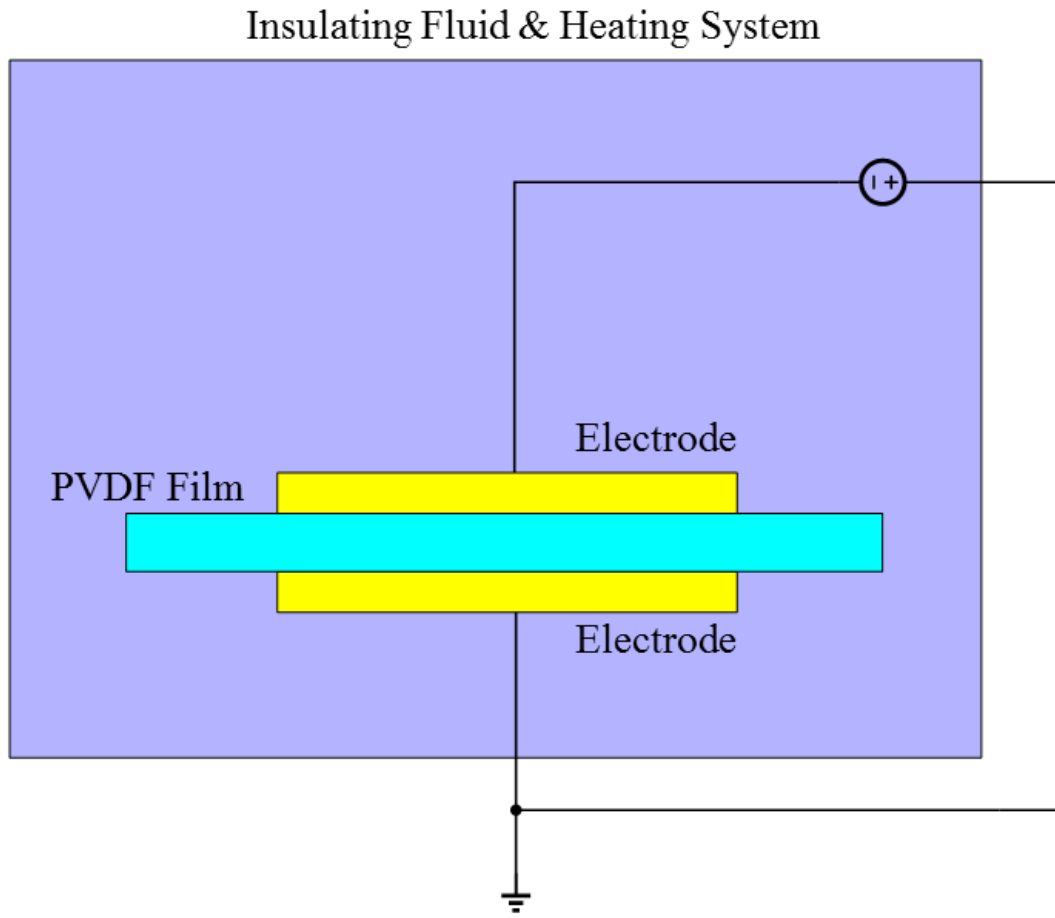
Fig. 2.9. Electrode poling setup.

In this research, a poling setup similar to the one used in the second poling method was chosen to complete the PVDF poling process. Fig. 2.6 shows the poling setup. The difference is that no insulating fluid is used in this setup.

The poling process is as follows: 1. PVDF film (conductive electrode layer coated) to be poled was put on a heating plate and connected to a DC power supply which could provide a 360 V DC bias voltage; 2. DC bias voltage was gently and slowly increased from 0 V to 360 V; 3. temperature of the heating plate was increased to 90 °C;

4. poling process last for 4 hours; 5. heating plate was cooled down to the room temperature after 4 hours' poling; 6. bias voltage was decreased to 0 V gradually.

2.4.4   ITO electrode fabrication

As the direct electrode material on the surface of the PVDF film, the quality of ITO layers plays a significant role on the photoacoustic signal received by the ultrasound tranducer. In this research, the ITO layers were deposited using RF sputtering. The deposition rate and the conductivity of the final films were measured and compared in order to optimize the related process parameters during the deposition. The conductivity of the final film is determined by the quality of the film.

Major process parameters that affect the despotion rate and film quality include deposition process pressure, RF power, gas mixture and substrate temperature. Since the PVDF film is a thin polymer film, high temperature will lead to the film's melting or losing the piezoelectricity. In this study, the deposition substrate was kept at the room temperature.

Two types of gases often used for RF sputtering are argon(Ar) and oxygen(O_2). Reference [29] also provides information about the effect of O_2 on the quality of the ITO film after the deposition. In the first test, the process pressure was set to be 3 mTorr and the RF power was set to be 100W. The final ITO thickness was set to be 240 nm. Different O_2 concentrations in the Ar-O_2 mixture wre tested. The ITO deposition rate and the sheet resistance of the ITO film were measured. The results are listed in Table 2.6.

Table 2.6. ITO deposition rate and film quality at different O2 concentrations.

O_2 concentration in Ar-O_2 mixture (%)	Deposition rate (Å/s)	Sheet resistance ($\Omega/square$)
0.1	0.30	45
0.5	0.12	38
1.0	0.10	55
2.0	0.08	96
4.0	0.07	120

Based on Table 2.6, the O_2 concentration in Ar-O_2 mixture was chosen to be less than 0.5% to result in an acceptable deposition rate and electrical conductivity. The deposition rate decreased quickly with the increment of the O_2 concentration. And also the sheet resistance of the ITO film increased following the same trend. The O_2 concentration should be kept at a low level during the deposition process.

Next, the effect of process pressure was tested. The O_2 concentration was set to be 0.1%, and the RF power was set to be 100W. The final thickness of the ITO layer was set to be 240nm. Different process pressures were used in the deposition. The deposition rate and the sheet resistance of the ITO layer were measured. The results are listed in Table 2.7.

Table 2.7. ITO deposition rate and film quality at different process pressures.

Process chamber pressure (mTorr)	Deposition rate (Å/s)	Sheet resistance ($\Omega/square$)
1.0	0.35	96
2.0	0.32	67
3.0	0.30	45
4.0	0.21	110

Based on Table 2.7, the optimal process chamber pressure was chosen to be 3 mTorr. As the process pressure increased, the deposition rate decreased quickly. But below 3 mTorr, the sheet resistance of the ITO layer increased when the process pressure decreased. Considering the quality of the film, the 3 mTorr was the best value for the process pressure.

Finally, the effect of the RF power on the quality of the ITO layers was tested. The O_2 concentration was set to be 0.1%, and the process chamber pressure was set to be 3 mTorr. The final thickness of the ITO layer was set to be 240nm. Three RF power values were tested: 100W, 150W and 200W. The results are listed in Table 2.8.

Table 2.8. ITO deposition rate and film quality under different RF powers.

RF power (W)	Deposition rate (Å/s)	Sheet resistance ($\Omega/square$)
100	0.30	45
150	0.34	44
200	0.40	48

Higher RF power will increase the deposition rate significantly, while the sheet resistance can still be kept at a very low level. But high RF power (greater than 150W) is also proved to increase the temperature of the PVDF film greatly. Since too much heat will make the PVDF film lose its piezoelectricity, the RF power should be kept at 100W.

2.5 Fabrication of 1D transparent PVDF ultrasound transducer array

In the above research work, a single element transparent PVDF transducer was made. Following the similar fabrication process, a 1D transparent PVDF ultrasound transducer array were made. Fig. 2.10 shows the 1D transparent PVDF ultrasound transducer array. It contains 16 elements, and the width of each element is 1 mm. The spacing between two neighboring elements is 0.4 mm. The width of transparent window of each element is 5.0 mm.
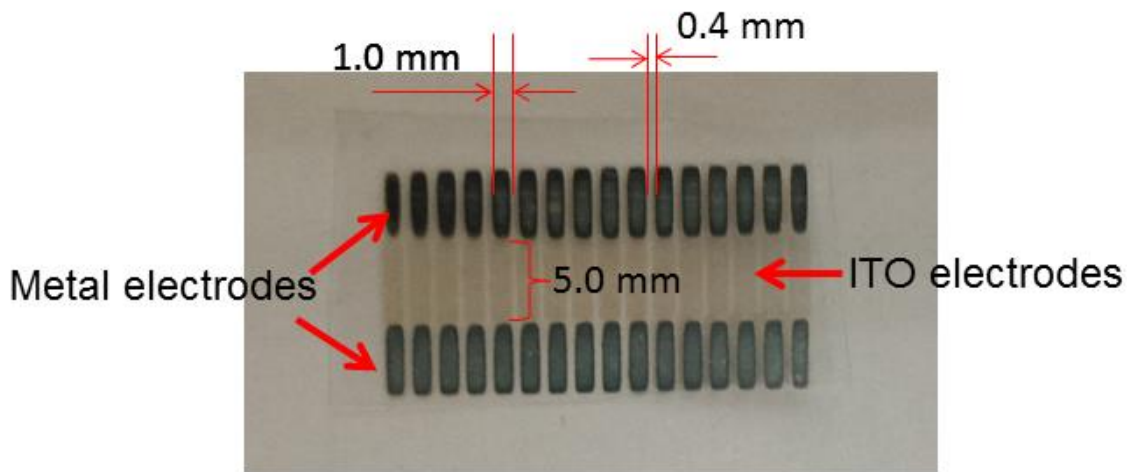
Fig. 2.10. 1D transparent PVDF ultrasound transducer array.

For making the transducer elements in the array, two groups of shadow masks were used: one group for ITO deposition and the other group for metal electrode deposition. The final transducer was a sandwiched structure. The diagram of the configuration of one transducer element is shown in Fig. 2.11. The central part was the ITO coated PVDF piezoelectric film. Since both ITO and PVDF film were transparent, the central part was the main part of this transducer. Laser shot through this transparent window to the target. On the top and bottom of the central window, there were metal (gold) coated regions. The metal layer on the ITO layer was used to increase the conductivity of the transducer electrodes.
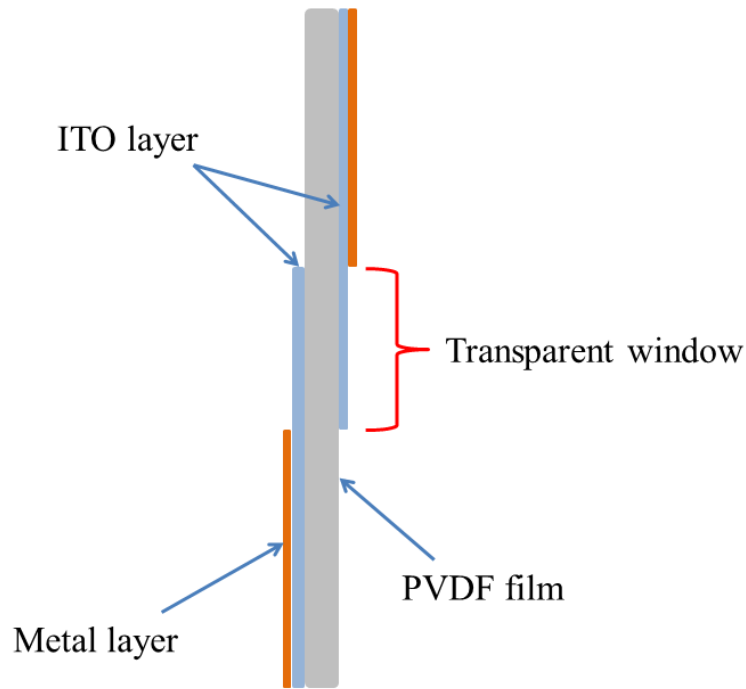
Fig. 2.11. Configuration of one transducer in the 1D PAT array.

2.6   Summary

In this section, two micromachined methods for fabricating PVDF based transparent transducers were developed. First, several types of piezoelectric materials were reviewed to provide a technical background for selecting the active element material for the transparent transducers. After choosing PVDF as the active material used in this transducer, two fabrication methods on making PVDF based transparent ultrasound transducer were developed. The PVDF poling method was studied and developed. Finally, a transparent ultrasound transducer array was developed for PAT applications.

3. SIGNAL AMPLIFICATION AND DATA ACQUISITION FOR TRANSPARENT PVDF ULTRASOUND TRANSDUCER

3.1   Electrical modeling of transparent PVDF ultrasound transducers

According to the transmission line theory, the transparent ultrasound transducer developed in the last section can be considered as a 2-port network [30-33] that is connected to the pre-amplifier through a coaxial cable. In order to realize high signal transmission efficiency from the transducer to the pre-amplifier, the input impedance of the pre-amplifier needs to be matched to the output impedance of the transparent ultrasound transducer.

The output impedance of two types of transparent ultrasound transducers was measured through the following steps: 1. the transducer was made with the microfabrication process described in Section 2.3; 2. two copper wires were soldered to the two electrodes of the transducer through E-solder 3022 (Von Roll Inc.); 3. the impedance analyzer (E4990A Impedance Analyzer) was used to measure the output impedance of the transducer. Table 3.1 shows the property information of the two types of transducers measured.

Table 3.1. The properties of two types of transparent ultrasound transducers

Property	Unit	Transducer 1	Transducer 2
Material	-	PVDF piezoelectric film from Measurement Specialties. Inc.	PVDF piezoelectric film from Piezotech S.A.S
Thickness	μm	28	9
ITO layer thickness	nm	300	300
Metal electrode	-	Aluminum	Aluminum
Transducer effective area	mm^2	3×3	2×2

The component model in the circuit theory used for this device is shown in Fig. 3.1. The 2-port device was modeled as a resistor in serial with a capacitor.
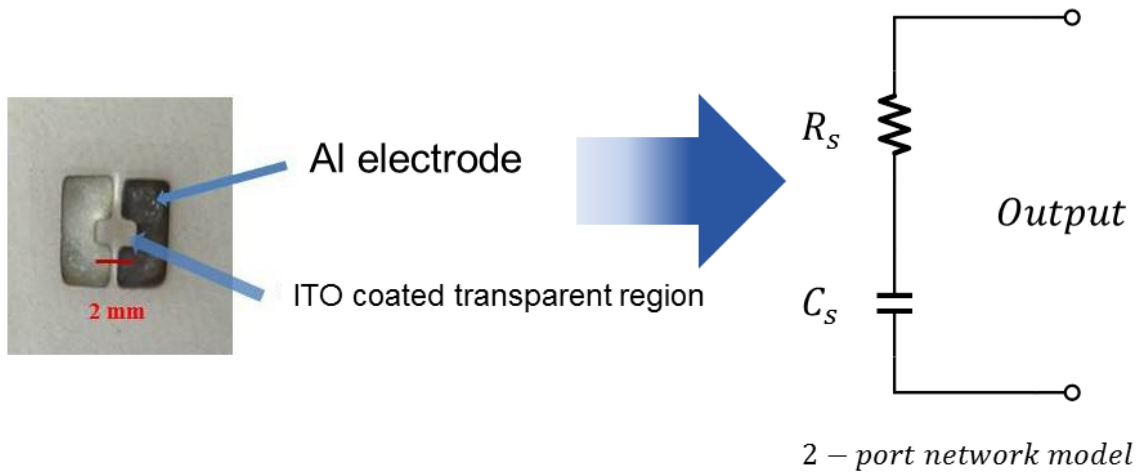
Fig. 3.1. Circuit model of the transparent ultrasound transducer.

The output impedance measurement results are shown in Fig. 3.2. The output impedance of the transducer was a frequency dependent value. Since the resonance

frequencies of the two transducers were 20MHz (transducer 1) and 30MHz (transducer 2) respectively, the impedance should be matched at these two frequencies. The measured impedance values at 20MHz and 30MHz are shown in Table 3.2.
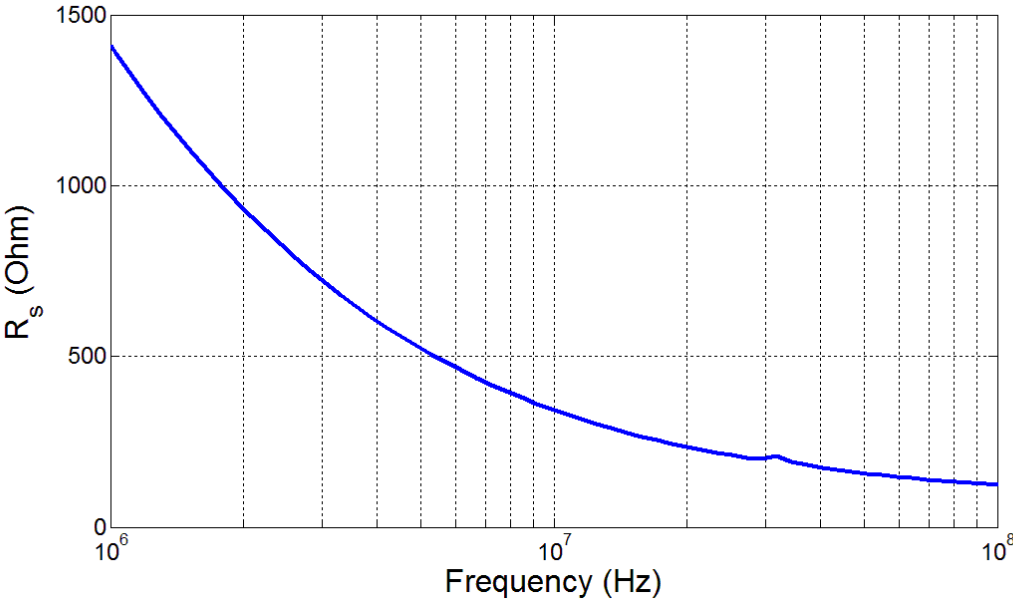
(a)

Fig. 3.2. Impedance parameters of two transducers: (a) serial resistance vs. frequency of transducer 1; (b) serial capacitance vs. frequency of transducer 1; (c) serial resistance vs. frequency of transducer 2; (d) serial capacitance vs. frequency of transducer 2.
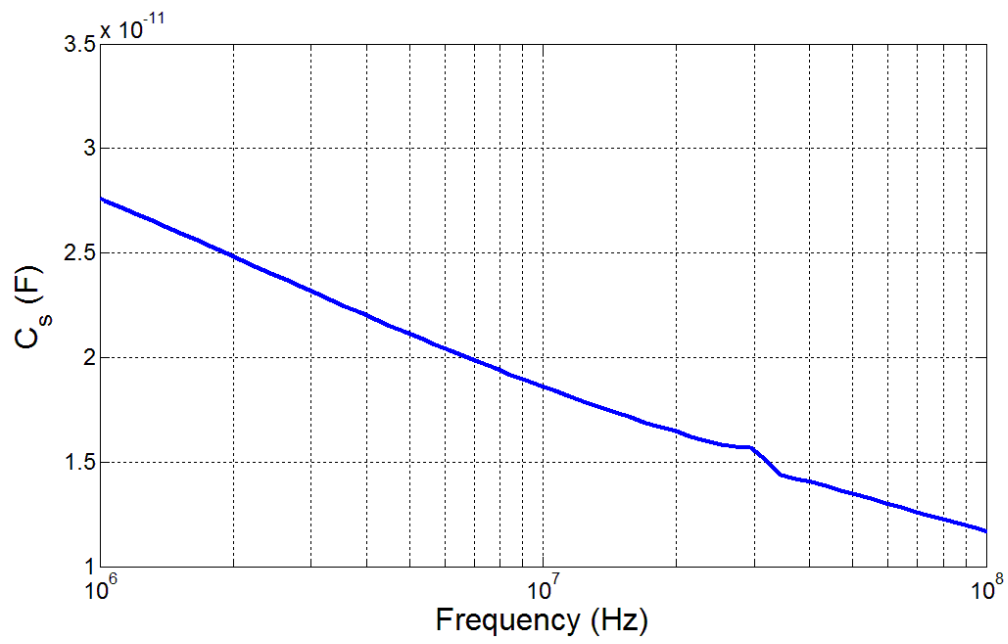
(b)
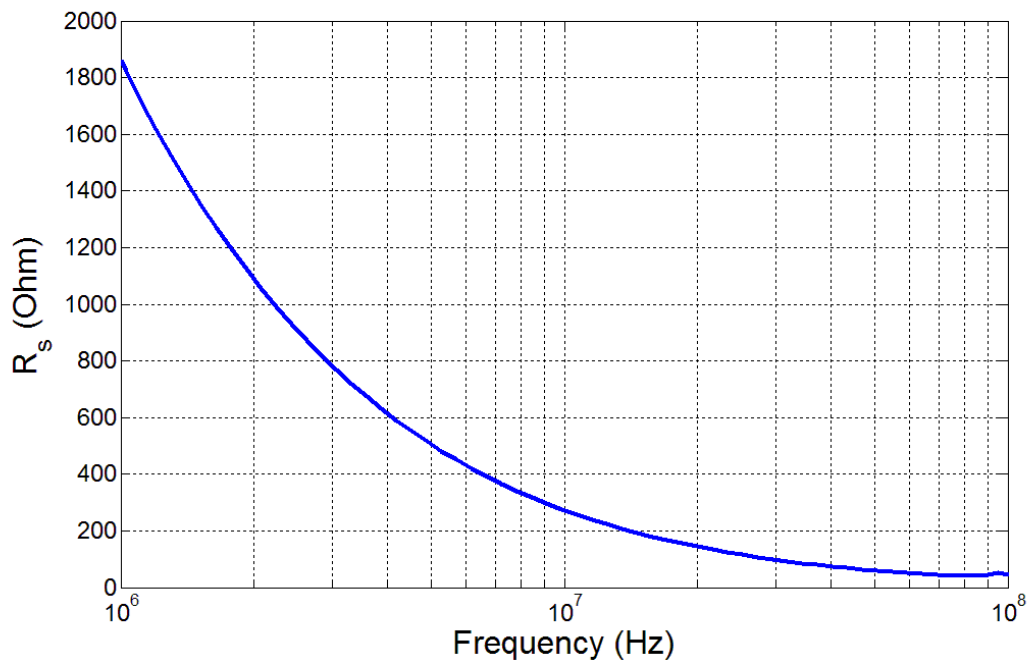
(c)

Fig. 3.2. Continued.
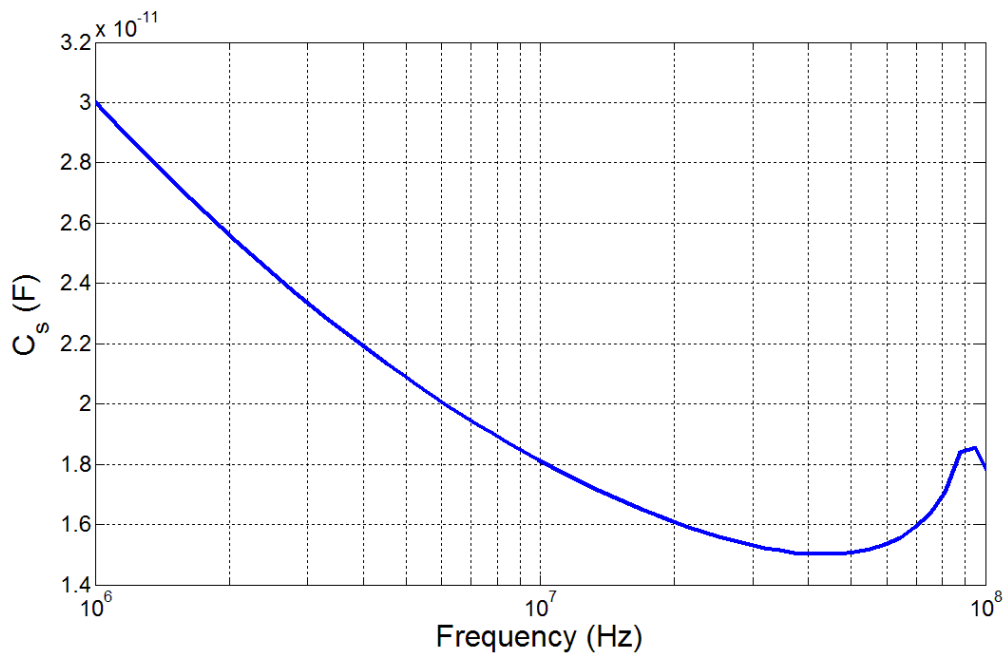
(d)

Fig. 3.2. Continued.

Table 3.2. Measured output impedance of the two transducers.

Frequency	Parameter	Transducer 1	Transducer 2
20MHz	R_s	234.01Ω	143.58Ω
	C_s	16.56pF	16.11pF
	X	−480.51Ω	−490.15Ω
	R	234.01Ω	143.89Ω
30MHz	R_s	202.50Ω	97.58Ω
	C_s	15.65pF	15.32pF
	X	−339.27Ω	−343.88Ω
	R	202.50Ω	98.23Ω

3.2   Amplifier design and simulation

The schematic of the pre-amplifier used in the photoacoustic imaging system is shown in Fig. 3.3. In this pre-amplifier, R_2 and R_4 determine its amplification and also the noise level. The amplification can be calculated through the following equation:

$$A = 1 + \frac{R_4}{R_1} \quad (3.1)$$

It can be seen from the above equation that a big R_4 to R_1 ratio will improve the amplification of the amplifier. However, big resistance will induce more noise to the circuit. In order to optimize the values for R_4 and R_2, a photoacoustic test was done using different R_4 and R_2 values. The transducer 1 in Table 3.1 is selected. It was directly connected to the pre-amplifier in Fig. 3.3.
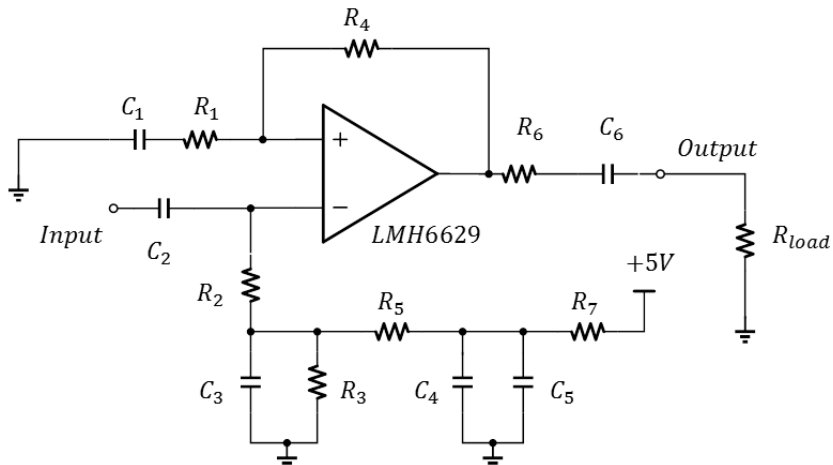
Fig. 3.3. Schematic of the pre-amplifier used in the photoacoustic imaging system.

An agar phantom containing a black tape target was used in the photoacoustic test. A 905 nm pulse laser was used as the excitation source. Its output energy was 100

nJ/pulse. The transparent transducer was positioned on the surface of the phantom and the laser shot through the transparent transducer to the target in the phantom. The output of the preamplifier was connected to an oscilloscope. The photoacoustic signal was recorded and analyzed on the oscilloscope.

Table 3.3. Values for components in the pre-amplifier.

Component Name	Value
R_1	33Ω
R_2	3.6kΩ
R_3	680Ω
R_4	3.6kΩ
R_5	680Ω
R_6	33Ω
R_7	10Ω
C_1	47nF
C_2	10nF
C_3	47nF
C_4	47nF
C_5	3.3µF
C_6	47nF

Different values of R_2 and R_4 were tested in the preamplifier. The photoacoustic signals' amplitude, pulse width and SNR are recorded in Table 3.4.

Table 3.4. Resistance optimization test results.

$R_2(\Omega)$	$R_4(\Omega)$	Photoacoustic pulse amplitude (mV)	Pulse width (ns)	Signal to noise ratio (SNR)
2.0K	6.8K	30.0	36	6.0
2.0K	3.6K	23.0	26	7.2
3.6K	3.6K	26.8	30	11.2
680	3.6K	11.6	26	3.2
3.6K	2.0K	12.8	28	3.2
2.0K	2.0K	13.6	26	2.8
68K	3.6K	30	60	6.0
6.8K	3.6K	26.8	40	8.3
2.2K	3.6K	28.8	38	10.28
2.2K	6.8K	32.0	44	6.15

From the Table 3.4, it can be seen that $R_2 = R_4 = 3.6K\Omega$, the output signal has the highest SNR while the pulse width is acceptable. The pulse width indicates the bandwidth of the signal and also the axial resolution of the photoacoustic imaging system. A shorter photoacoustic pulse gives a higher axial resolution. Therefore, considering the above factors, R_2 and R_4 were chosen to be 3.6KΩ.

The input impedance of the pre-amplifier when it was working was also measured through the impedance analyzer. The input impedance value over the frequency range (20Hz to 200MHz) is shown in Fig. 3.4. And the measured input impedance values at 20MHz and 30MHz are shown in Table 3.5.
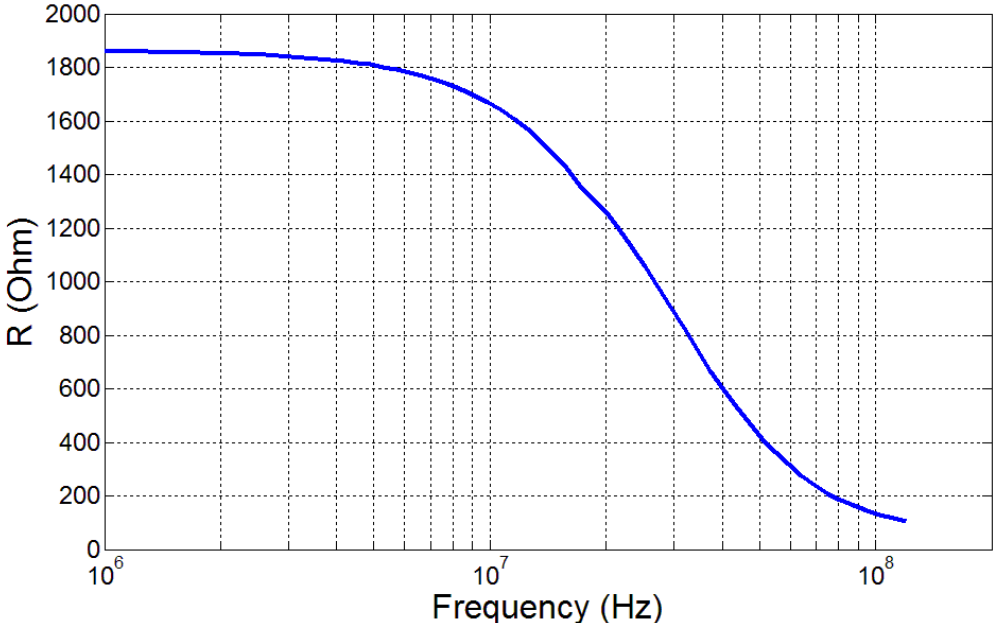
(a)

Fig. 3.4. The real part (R) (a) and imaginary part (X) (b) of the input impedance of the preamplifier.

X (Ohm) vs Frequency (Hz)
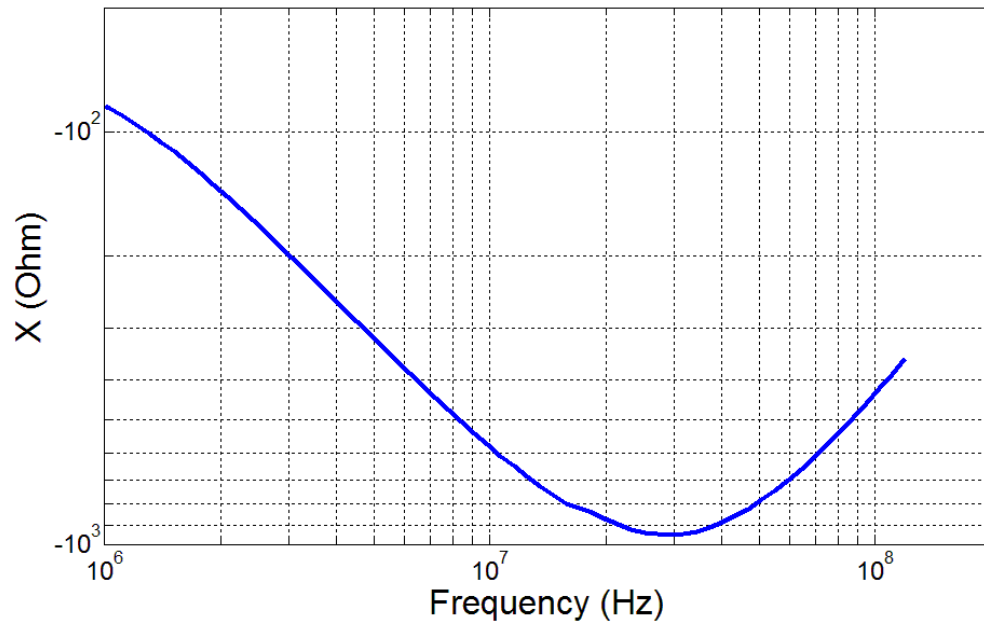
(b)

Fig. 3.4. Continued.

Table 3.5. Input impedance of the preamplifier at 20MHz and 30MHz.

Input and feedback resistance values		Impedance (Ω)	
		$R_2 = 3.6K\Omega, R_4 = 3.6K\Omega$	$R_2 = 3.6K\Omega, R_4 = 2.0K\Omega$
20MHz	R	1279	1262
	X	-1595	-869
30MHz	R	710	863
	X	-1363	-943

49

3.3   Impedance matching network design and simulation

According to the L matching network theory, one L matching network has its

bandwidth determined by the two impedances it is matching. For the impedance

matching problem in this research, a wideband matching network is suitable. The ideal

photoacoustic signal obtained from the ultrasound transducer should be a short electronic

pulse without any "ripples" in the time domain. If this signal is Fourier transformed to

frequency domain, it is a wideband signal. Therefore, an ideal matching network for the

ultrasound transducer should be a wideband network with a small Q. This kind of

matching network can be achieved by cascading several L sections. For example, in Fig.

3.5, if we need to match the source impedance R_S with the load R_L, a cascade n L

matching stages are used. The matching process is shown below.
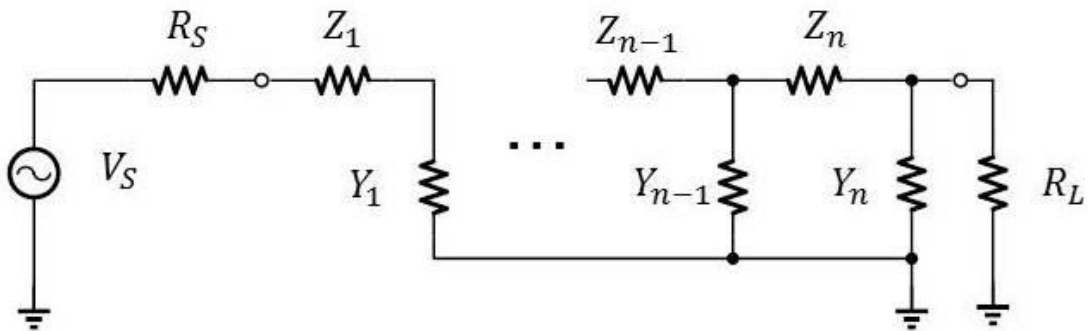
Fig. 3.5. N-level cascade L matching network.

$$R_S \rightarrow R_S \left(\frac{R_L}{R_S}\right)^{\frac{1}{n}} \rightarrow R_S \left(\frac{R_L}{R_S}\right)^{\frac{2}{n}} \rightarrow \cdots \rightarrow R_L \text{ (3.2)}$$

The Q of each section is:

$$Q^{(n)} = \sqrt{\left(\frac{R_L}{R_S}\right)^{\frac{1}{n}} - 1} \text{ (3.3)}$$

The normalized bandwidth of the matching network is:

$$\text{BW} = \frac{f_0}{Q^{(n)}} \sqrt{\sqrt[n]{2} - 1} \text{ (3.4)}$$

If we make use of the expression for the bandwidth of a cascade of tuned sections:

$$BW_n = BW_1 \sqrt{\sqrt[n]{2} - 1} \text{ (3.5)}$$

In the limit of a large number of sections, the total bandwidth approaches a number of order unity,

$$\lim_{n\to\infty} \text{BW} = \sqrt{\frac{\ln(2)}{\ln(m)}} \text{ (3.6)}$$

In the above equation, m is the ratio of the impedances that are being matched. This cascade of L network is a useful approximation of a distributed wideband matching network.

A 3-level cascade L matching network was chosen to implement the impedance matching between the transparent ultrasound transducer and the pre-amplifier. The values of components in this L matching network are shown in Fig. 3.6 and Table 3.6. The transducer was connected to the input and the output of the matching network was connected to the pre-amplifier.
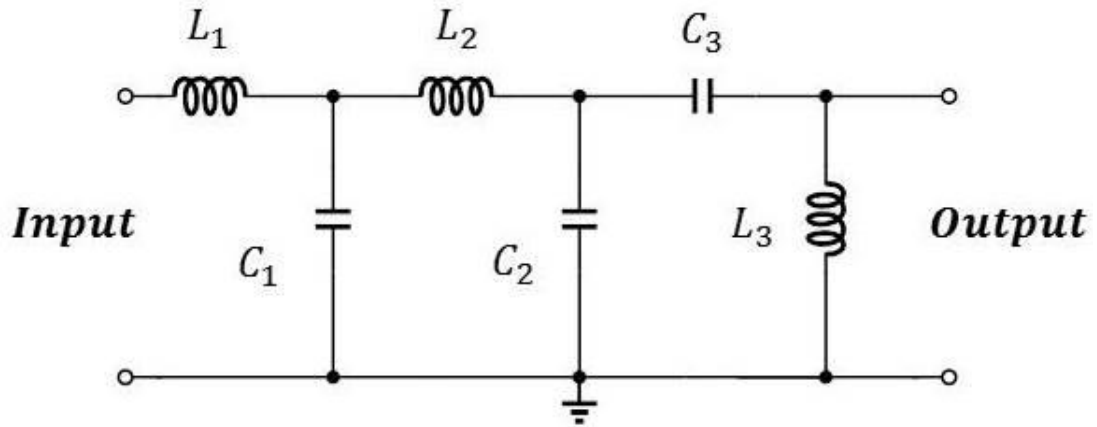
Fig. 3.6. 3-Level L matching network.

Table 3.6. Component values in the 3-level L matching network.

Component Name	Value
L_1	2.02μH
L_2	2.43μH
L_3	7.01μH
C_1	27.1pF
C_2	8.1pF
C_3	3.5pF

The gain of the pre-amplifier before and after the impedance matching was simulated. Fig. 3.7 shows the gain-frequency curves of the preamplifier with and without the 3-level L matching network.

52

-3dB bandwidth: 6.68MHz
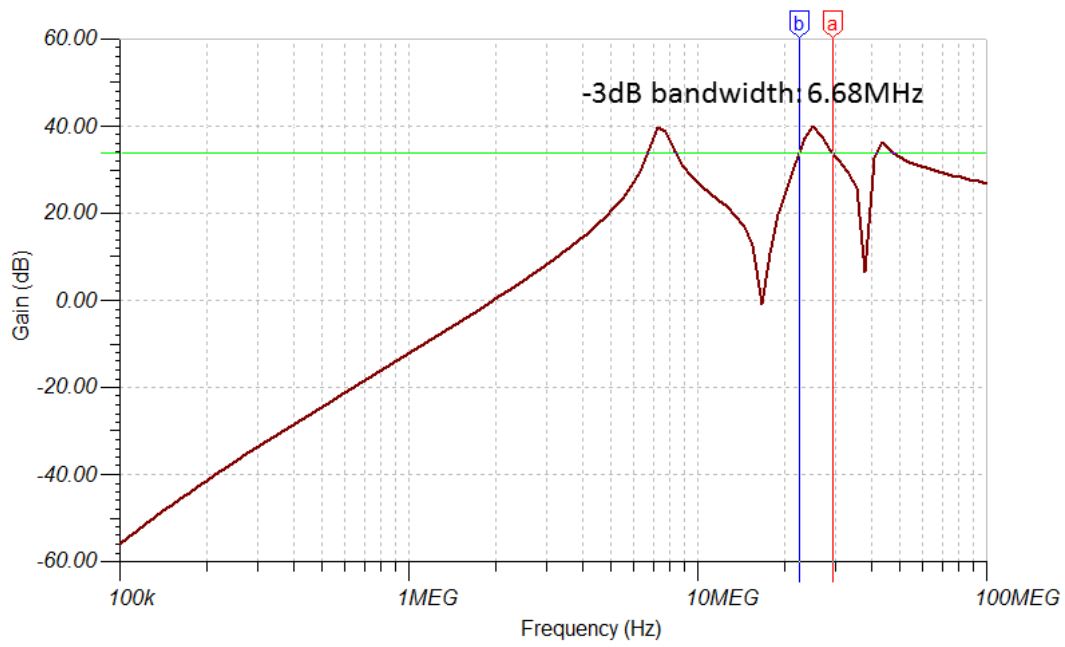
(a)

Fig. 3.7. Gain-frequency curves of the preamplifier: (a) gain of the pre-amplifier without impedance matching network; (b) gain of the pre-amplifier with the 3-level L matching network.

-3dB bandwidth: 24.52MHz
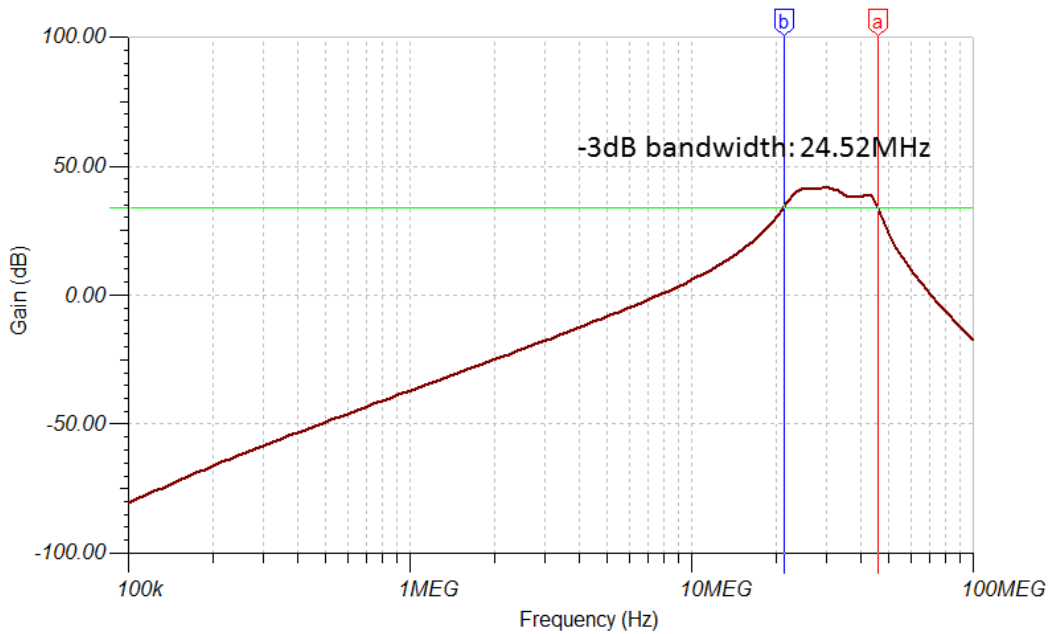
(b)

Fig. 3.7. Continued.

Since the central resonance frequency of the designed transparent transducer was around 20MHz to 30MHz, the gain of the preamplifier at the range 20MHz to 30MHz was more important. From Fig. 3.6. it can be seen that without impedance matching network, the -3dB bandwidth of the preamplifier (at the range 20MHz to 30MHz) was only about 6.68MHz. After the 3-level L matching network was added, the bandwidth reached 24.52MHz. Therefore, a good impedance matching can help improve the bandwidth of the signal greatly. A 2-level L matching network's performance was simulated for bandwidth comparison. After adding the 2-lelve L matching network, the gain-frequency performance of the preamplifier was simulated. The result is shown in Fig. 3.7. Fig. 3.8 shows the gain-frequency curve of the preamplifier using 2-level L

impedance matching network. It can be seen that the bandwidth of the 2-level L matching network was smaller than that of the 3-level L matching network.

Fig. 3.8. Gain-frequency curve of the preamplifier using 2-level L impedance matching network.

Another popular impedance matching network: π network was also studied in this research as a comparison impedance matching method. The π impedance matching network can be considered as two L-networks back to back. Compared with the design of L-network, its design is relatively flexible. It has more design freedom than that of 1-level L matching network. A low pass version π network is shown in Fig. 3.9. After

55

matching, the gain-frequency performance of the pre-amplifier was simulated. The result

is shown in Fig. 3.10.
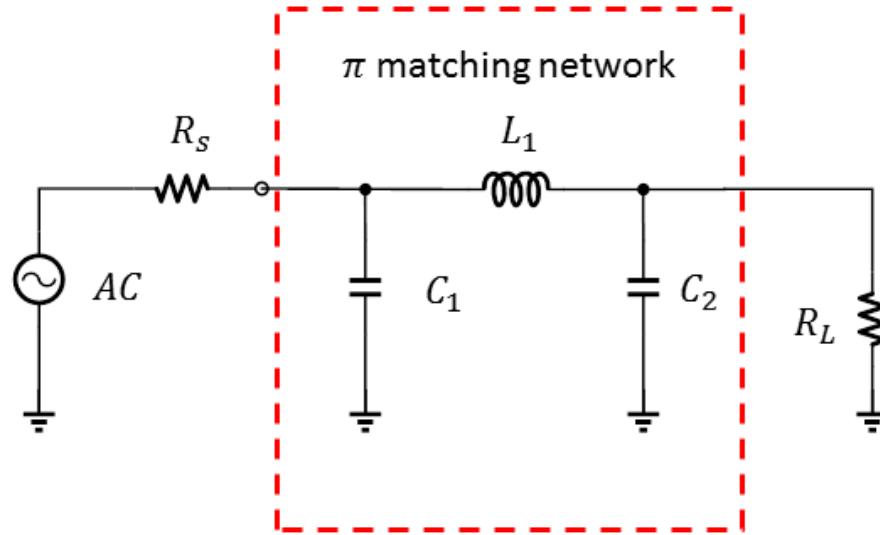
Fig. 3.9. Low pass π impedance matching network.
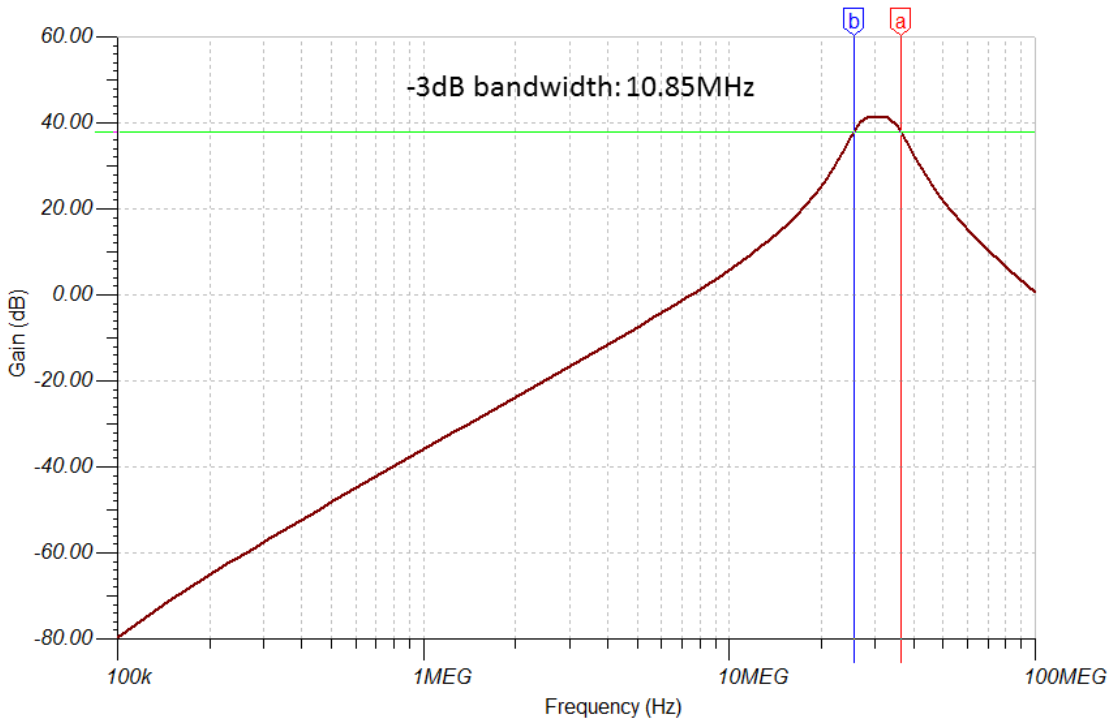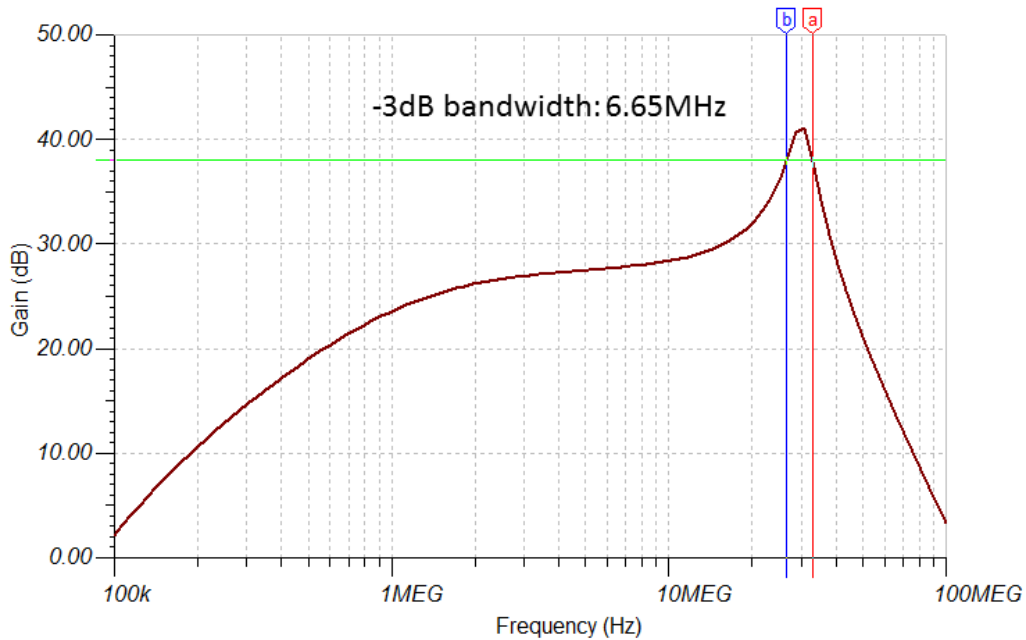
Fig. 3.10. Gain-frequency curve of the preamplifier using π impedance matching

network.

The π impedance matching network could improve the gain at the central frequency, but its bandwidth was quite limited (only 6.65MHz) compared with the 3-level L matching network. The smaller bandwidth would lower the axial resolution of the transducer. A comparison table (Table 3.7) comparing the performance of the above three impedance matching networks is shown below. Using the 3-level L matching network, an amount of amplification is sacrificed, but the bandwidth is much wider than those of the other two networks. Since the preamplifier is used to suppress the noise and improve the SNR of the signal, the wide bandwidth is more important than its amplification. In conclusion, a 3-level L matching network is a better choice than the π impedance matching network or 2-level L matching network for this application.

Table 3.7. Comparison of three impedance matching networks.

	3-level L	2-level L	Low pass π
Maximum gain (dB)	38	40	41
-3dB bandwidth (MHz)	24.52	10.58	6.65

3.4   Data acquisition interface design

In order to develop a complete data acquisition system for multiple PVDF transparent ultrasound transducers, for example an ultrasound transducer array, a data acquisition interface for PVDF transparent ultrasound transducers was designed.

After developing an impedance matching network for PVDF transparent transducers, a data acquisition system consisting of matching networks, preamplifiers, a multiplexer, a main amplifier and PC control and data acquisition programs was developed. The whole system is shown in Fig. 3.11. In the system, every transparent ultrasound transducer was connected to one impedance matching network. Then the output of matching network was connected to a preamplifier. In order to obtain signals from different channels, a multiplexer was used to select a specified channel during the data acquisition process. The main chip used in the multiplexer circuit was CD74HC4052 (Texas Instruments Inc., Dallas, TX, United States). Then the signal was sent to a main acoustic signal amplifier (5072PR, Olympus Inc., Houston, TX, United States). The amplified signal was received and recorded by the data acquisition system (NI PCIe 6320, National Instruments, Austin, TX, United States). And at the same time

the data acquisition system sent selection signals to the multiplexer to select different channels. This system could be used for the photoacoustic signal acquisition from single or multiple PVDF transparent ultrasound transducers.
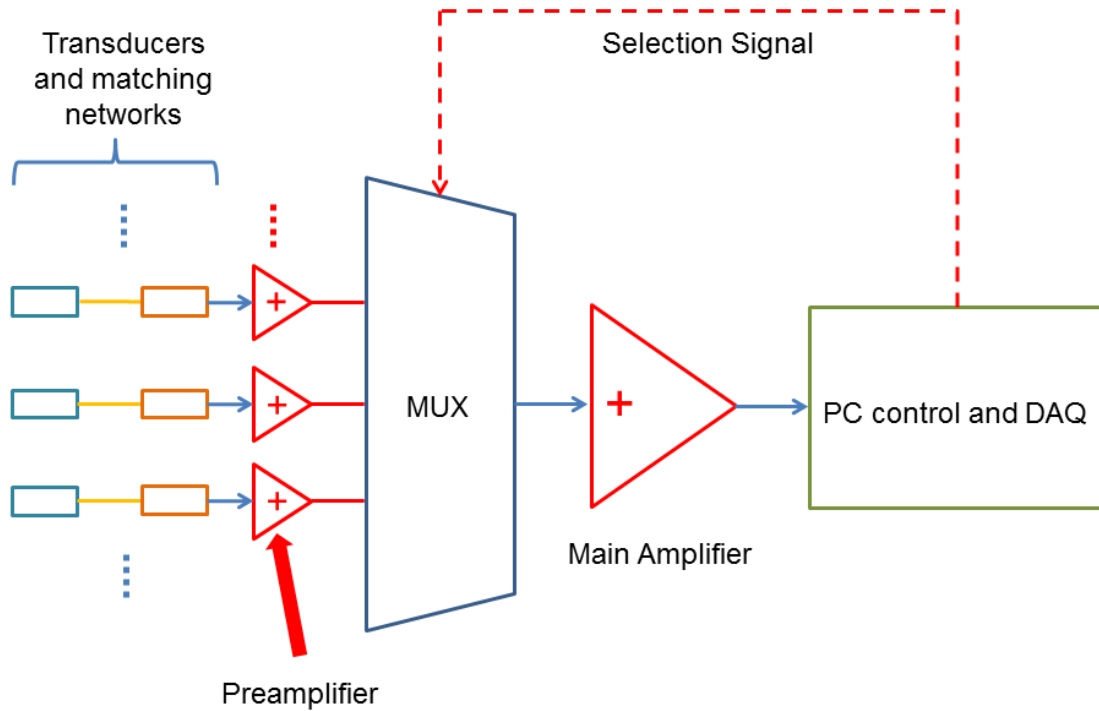
Fig. 3.11. Data acquisition interface and system for single and multiple PVDF transparent ultrasound transducers.

3.5   Summary

In this section, the electronic properties of PVDF transparent ultrasound transducers were investigated. Circuit models of PVDF transducers were developed based on measurement data. The electronic properties of the pre-amplifier which is directly connected to the PVDF transducer were investigated. Combining with the

measurement data of PVDF transducers, several impedance matching networks were designed. Through circuit performance simulation, the matching efficiencies of these networks were quantified. Based on the comparison, a 3-level L matching network was finally selected as the impedance matching network for the PVDF based transparent ultrasound transducers.

4. PHOTOACOUSTIC MICROSCOPY USING TRANSPARENT PVDF ULTRASOUND TRANSDUCER

4.1   Imaging system setup

A new PAM system based on the fabricated transparent ultrasound transducer,was built. Compared with the existing PAM systems, the new system is much simpler and more straightforward. As shown in Fig. 4.1, the pulse laser was focused with the objective lens and shot through the transparent ultrasound transducer to the target. The generated photoacoustic signals were directly detected by the transducer above the target. It reduced the energy loss and improved the efficiency of the excitation laser. The 905 nm/532 nm pulse laser system provided necessary excitation laser pulses for PAM imaging. The iris in front of the laser system was used to control the laser energy. The positive lens was used to focus the laser and couple it into the optical fiber. After the optical fiber, the laser pulse energy was further reduced using a filter. The objective was used to focus the laser beam out of the optical fiber to a 20 μm by 20 μm region which was the size of one pixel in the final PAM image. X-Y scanning stage moved the target during the imaging process, which realized the 2D scanning. The photoacoustic signal received by the transducer was transmitted to the amplifier system, which included a pre-amplifer and a main amplifier. The amplified signal was sent to the data acquisition oscilloscope. A PC connected to the data acquisition oscilloscope and the X-Y scanning stage was used to control the operation of the whole system. A photodiode (PD) with a

power and energy meter detected a laser pulse and then generated a trigger signal to the control and data acquisition system.
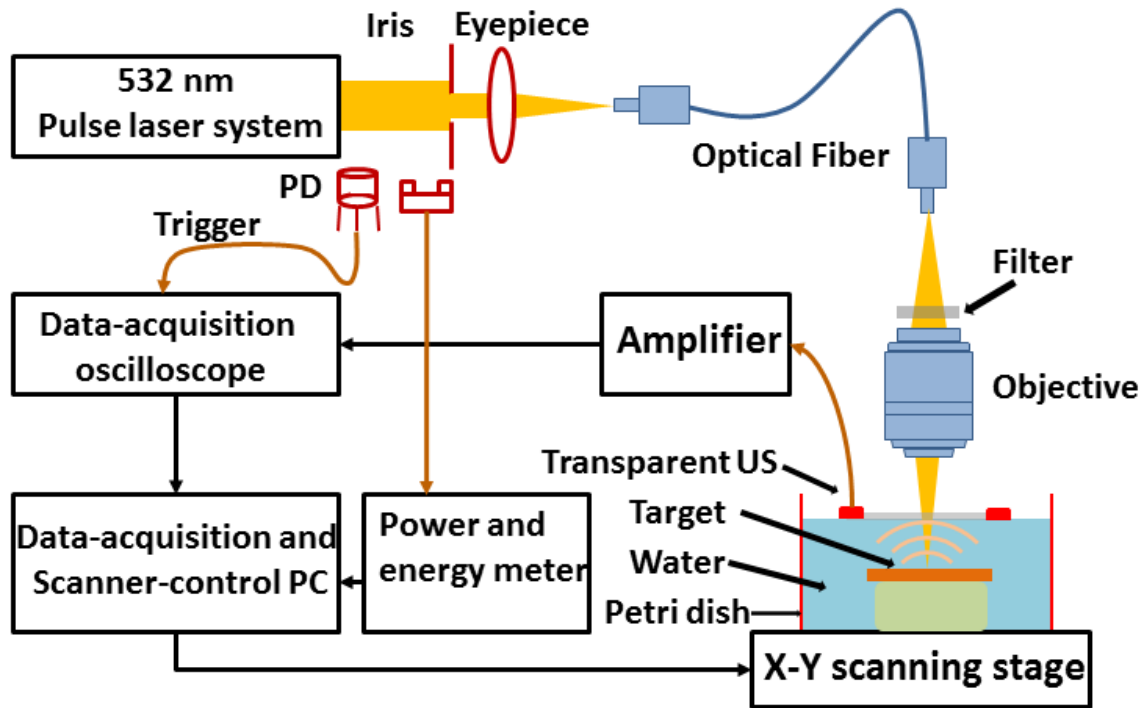
Fig. 4.1. Photoacoutisc microscopy system based on transparent ultrasound transducers.

The response of the transparent ultrasound transducer was measured first. Using a transducer made from 28um thick PVDF film, the photoacoustic signal excited by a 532nm pulse laser was measured. The time domain and frequency domain responses are shown in Fig. 4.2. From the measured results it can be seen that the photoacoustic pulse width was about 30ns and the bandwidth of the pulse was about 30MHz, which was close to the theoretical resonant frequency of the 28um thick PVDF film.
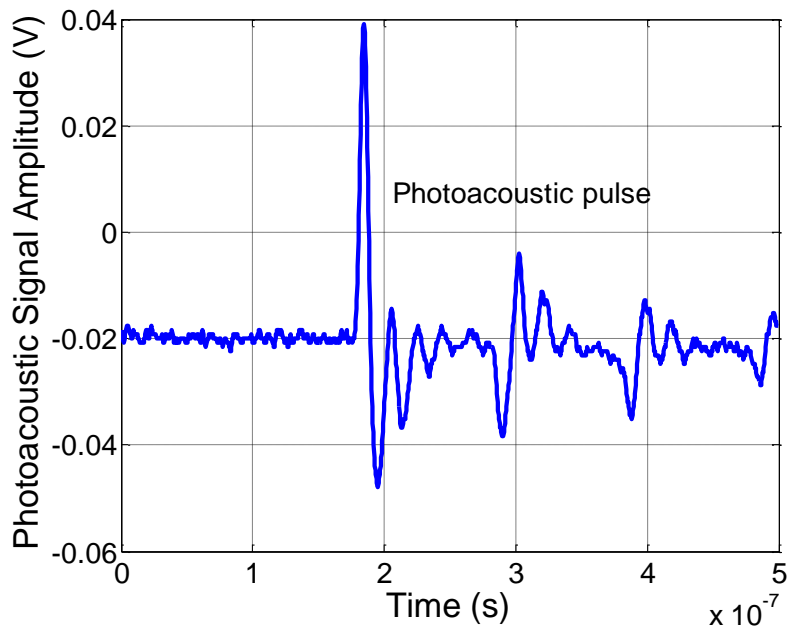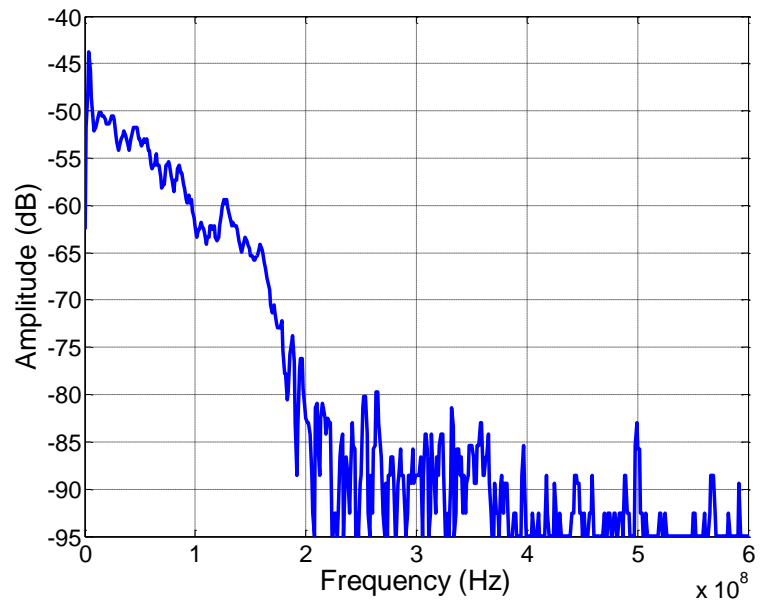
Fig. 4.2. Pulse laser excited photoacoustic pulse signal: (a) time domain; (b) frequency

domain.

63

4.2   Imaging performance characterization with optical phantom

4.2.1   Signal to noise ratio

To measure the signal to noise ratio (SNR) of the transparent ultrasound transducer, an agar phantom containing a target made of black tape was tested. The transparent transducer was made of a 9μm thick PVDF piezoelectric film. Its resonance frequency was about 50MHz. The agar phantom was made by boiling the agar-water mixture (2% weight ratio) and cooling it at the room temperature. The depth of the target in the phantom was about 2mm. During the test, the transparent transducer was attached to the surface of the agar phantom, and a small amount of DI water was added between the transducer and the phantom surface to improve the acoustic signal coupling efficiency. The 905 nm pulse laser (pulse width: 8 ns, energy: 150 nJ/pulse, repetition rate: 1 KHz) was shot through the transducer to the target in the phantom. Since the goal of this test was to measure the SNR of the transparent transducer, the output of the transducer was directly sent to the oscilloscope which was used to record and analyze the signal. A control test was also conducted using the same setup. The difference was that a "blank" phantom without any target inside was imaged in order to get the noise information of the transparent transducer. Fig. 4.3 shows the photoacoustic signal from the target phantom.
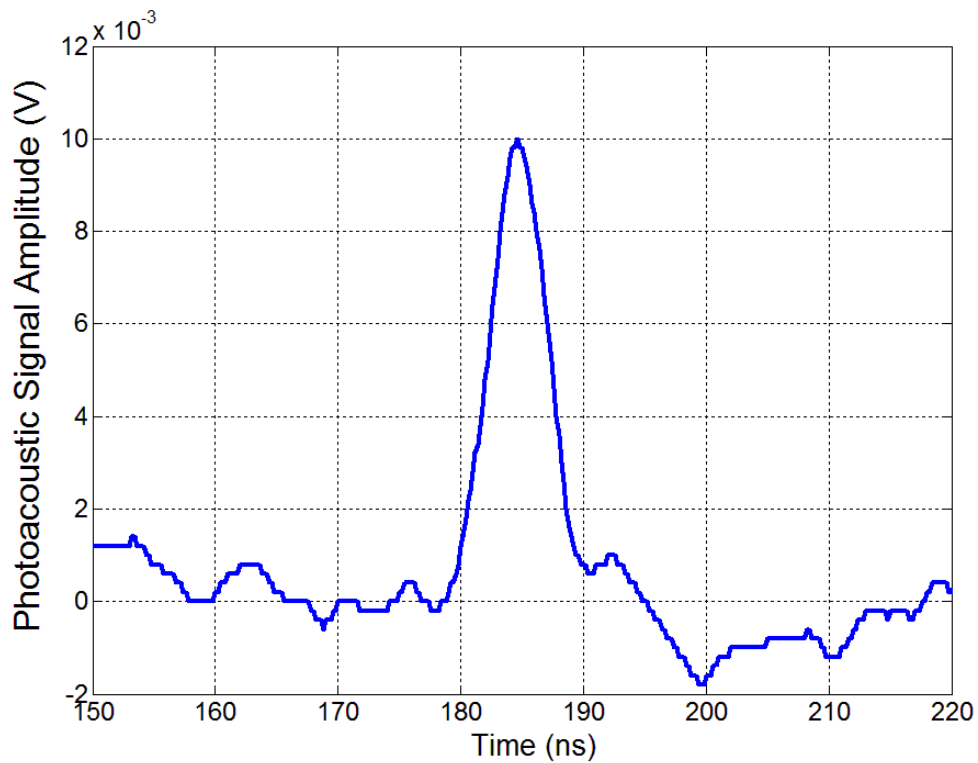
Fig. 4.3. The photoacoustic signal from black tape made target.

From Fig. 4.3, it can be seen that the amplitude of the photoacoustic pulse was about 10 mV. Its pulse width was about 10 ns, which means the axial resolution of this transducer was about 15 μm (considering the ultrasound velocity in the water is about 1500 m/s). The noise level was also measured through the results from the control test. The noise level was about 2 mV. Therefore the SNR of the transducer was about 5.

4.2.2   Spatial resolution

To measure the lateral resolution of the PAM system, a sharp blade was imaged in an agar phantom (Fig. 4.4) at varied depths with the same optical focus depth. The lateral resolution was determined by the spread function of the blade [34]. The image of

65

the blade was a line spread function. The full width of the half maximum of the line

spread function was the lateral resolution of the PAM system.
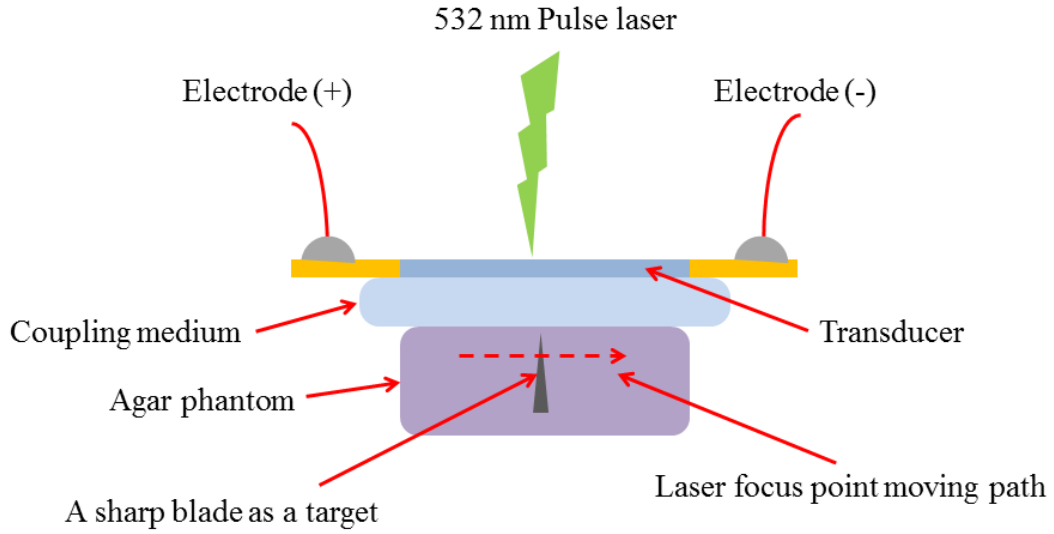
Fig. 4.4. PAM lateral resolution measurement setup.

In order to compare the effect of depth on the resolution, the lateral resolution

values on the top and the bottom illumination were also quantified following the same

method. The theoretical model used for fitting the measured results is a Gaussian beam:

$$w(z) = \sqrt{w_0^2 + \left[\frac{\lambda(z - z_0)}{\pi w_0}\right]^2} \quad (4.1)$$

$$P(x, z) = P_0\left[1 - e^{-2(x-x_0)^2/w^2(z)}\right] \quad (4.2)$$

where $w(z)$ is the lateral resolution at location z, w_0 is the focal diameter, λ is the

wavelength which is 905 nm, z_0 is the focal depth, x_0 is the location of the blade, P_0 is

the photoacoustic signal intensity at the location of the blade and $P(x, z)$ is the

photoacoustic signal intensity at location x and depth z. Fig. 4.5 shows the fitting results at different depths.
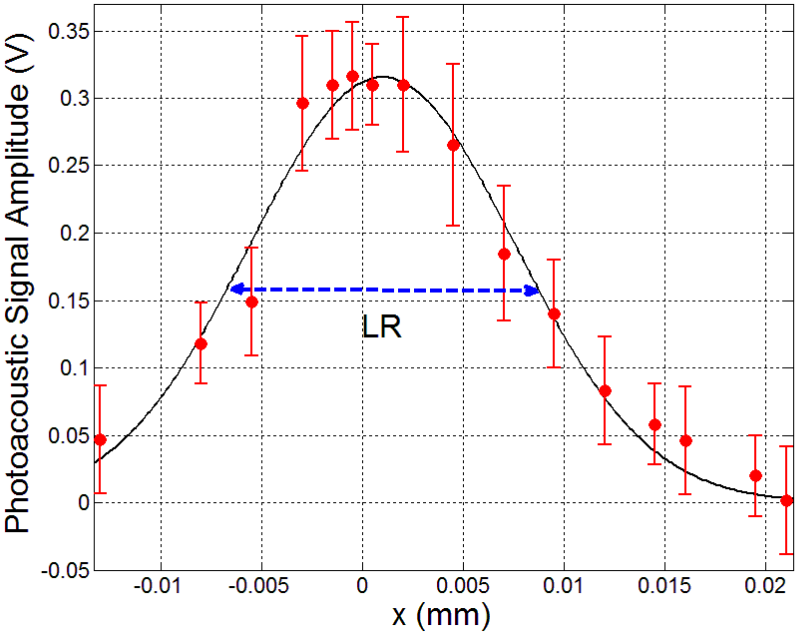
(a)

Fig. 4.5. Gaussian fitting blade cross-section photoacoustic image profiles at three different depths: (a) 1mm; (b) 0.9mm; (c)1.1mm.
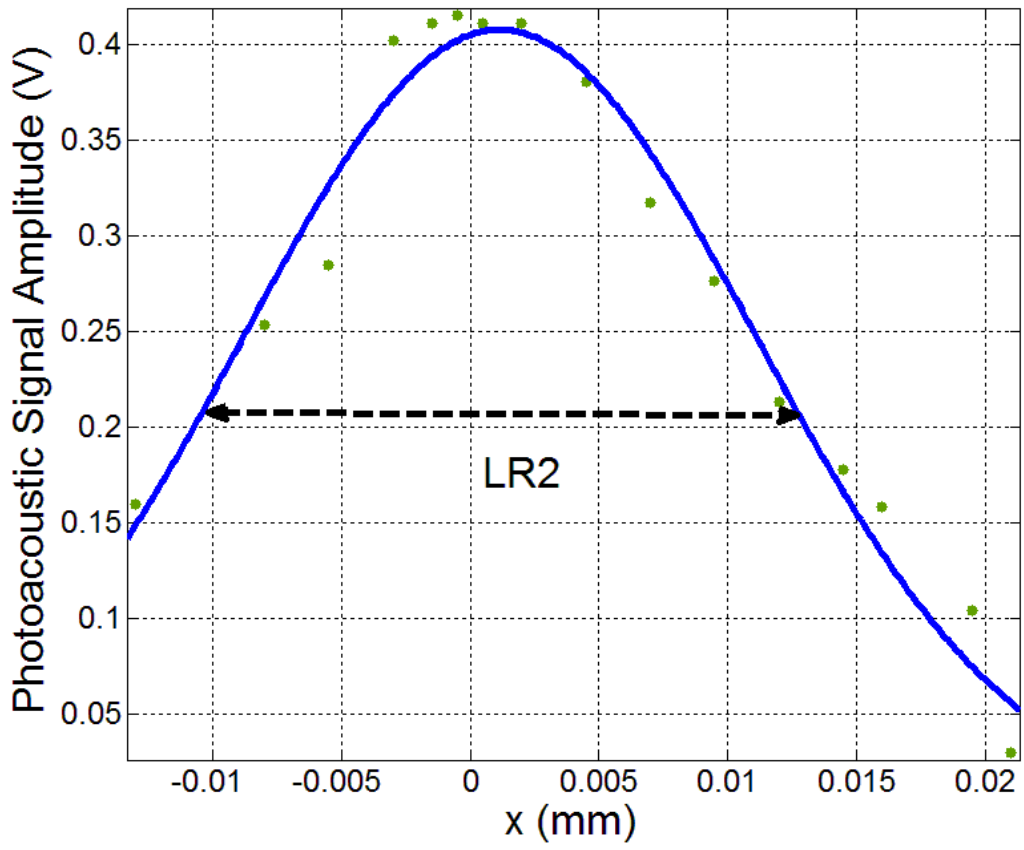
(b)

Fig. 4.5. Continued.
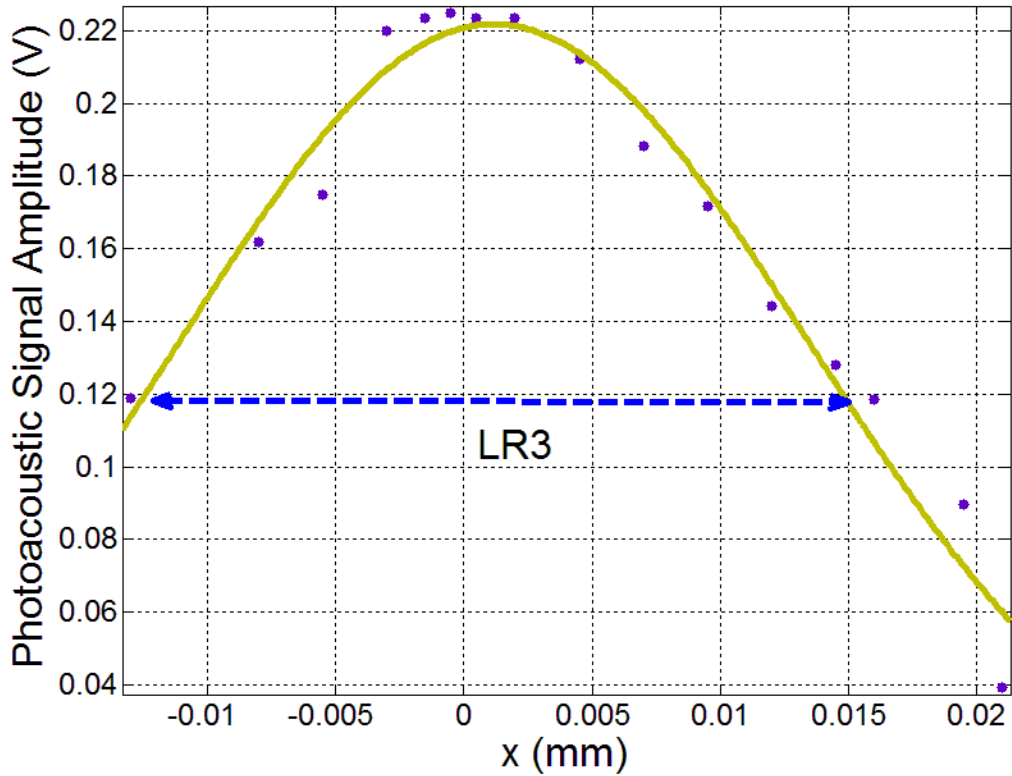
(c)

Fig. 4.5. Continued.

Since the blade was inserted into the agar phantom and distance between the

surface of the agar phantom and the blade was 1 mm, Fig. 4.5(a) shows the

photoacoustic image of the blade when the laser was exactly focused on the blade. The

lateral resolution was defined as the width of the photoacoustic intensity profile of the

blade cross-section where the intensity value was half of the maximum value. Therefore,

on the focus point, the lateral resolution of the PAM was about 15 μm, which is shown

in Fig. 4.5(a). In the region out of the focus, the Fig. 4.5(b)(c) show the lateral

resolutions of the PAM at the depths ($\mp$0.1mm of the focus depth). The lateral resolution

lowered to 23~28μm. So the focal zone of the PAM was about 0.2 mm.

4.2.3   Sensitivity uniformity

One unique property of the PAM using the transparent ultrasound transducer was

that the view-field was much wider than that of the traditional PAM system. The

transducer used in this PAM system was a 2 mm by 3 mm ITO coated PVDF

piezoelectric film. The laser could scan across this 2 mm by 3 mm area, and every point

of this area could receive photoacoustic signals. Since the ITO layer was not an ideal

conductor, the photoacoustic sensitivity across this 2 mm by 3 mm area could be non-

uniform. A test was conducted to measure the uniformity of the photoacoustic sensitivity

across this area. The test setup is shown in Fig. 4.6(a).

In order to test the uniformity of the transducer's sensitivity across the film area,

66 test points were chosen on different locations of the transducer film (Fig. 4.6(b)).

These points were distributed uniformly on the surface of the transducer used in this test.

532 nm Pulse laser

Electrode (+)

Electrode (-)

Coupling medium

Transducer

Uniform black tape as a target

(a)Side-view of the test setup

2 mm

3 mm

Test point array

ITO coated PVDF

Copper electrode
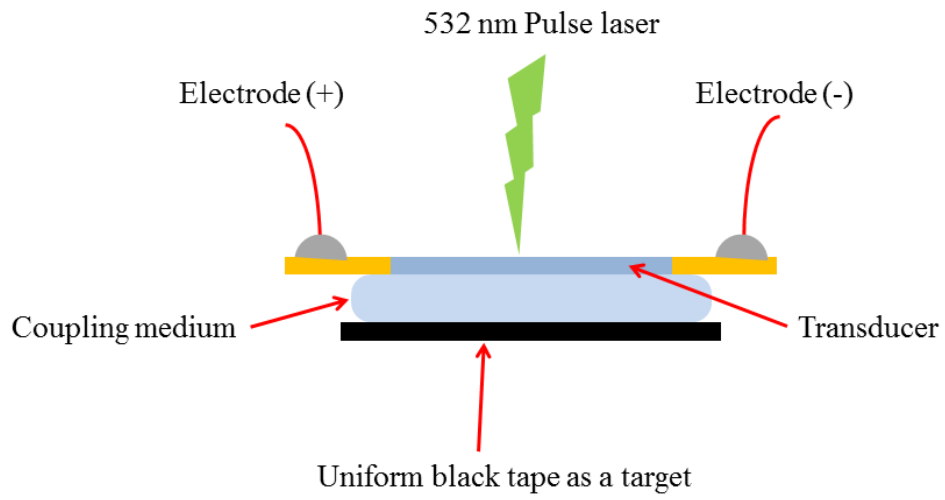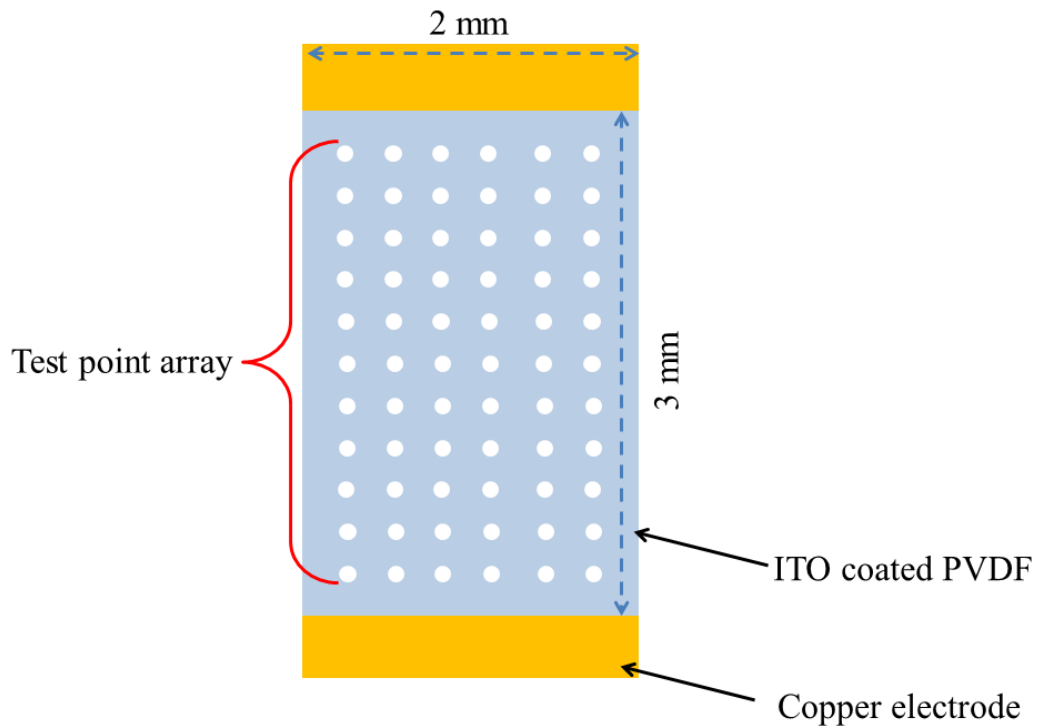
(b)Top-view of the test setup

Fig. 4.6. Sensitivity uniformity test setup: (a)side-view; (b) top-view.

After obtaining photoacoustic signals from all 66 test points, the signal strength values were normalized. The normalized strength values at different locations are shown in Fig. 4.7.
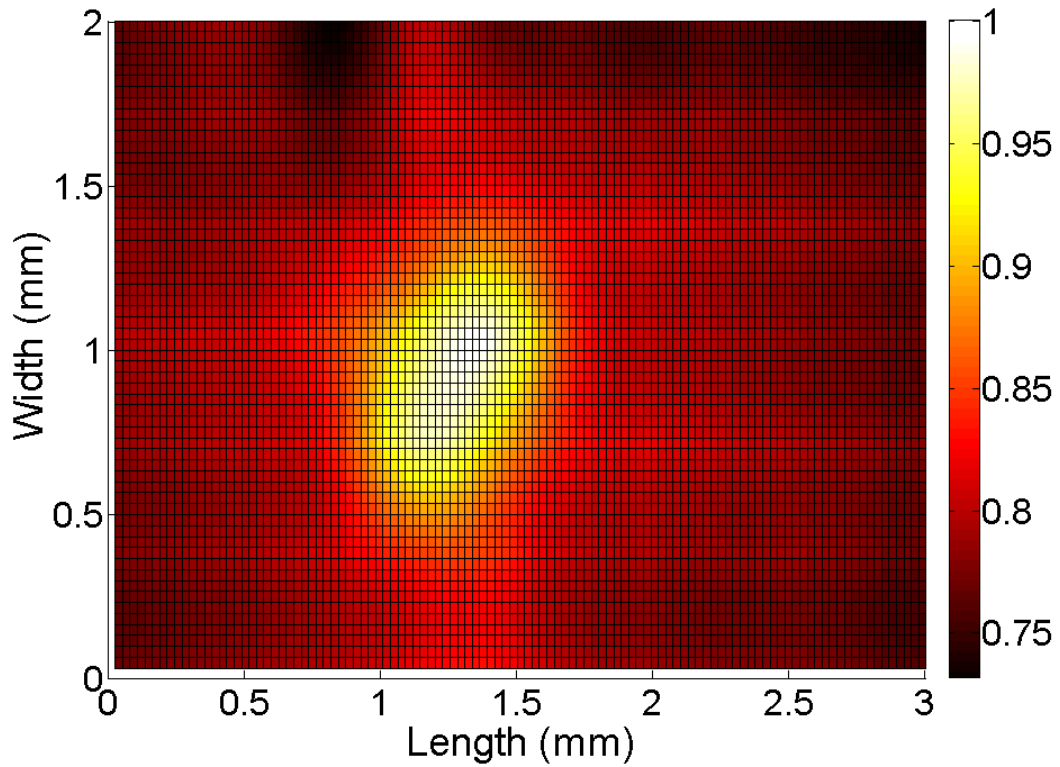
Fig. 4.7. Normalized photoacoustic signal strength at different locations of the transparent transducer.

According to the results shown in Fig. 4.7, the center part of the square transparent transducer was relatively more sensitive than the edge part. But the absolute sensitivity difference between the center part and the edge part is quite small. The standard deviation of the 66 test points was 0.019. And also the standard deviations of

different regions are calculated and listed in Table 4.1. The uniformity of the transparent

transducer is good enough to provide a wide field of view for PAM.

Table 4.1. Normalized photoacoustic sensitivity standard deviations of different regions of the transparent transducer.

Region Area (mm^2)	Sensitivity standard deviation (%)
Whole 2 × 3	1.9
Central 1.5 × 2	0.096
Central 1 × 1.5	0.015

Using the above PAM system, the first photoacoustic microscopy image based on a transparent ultrasound transducer was obtained. It is shown in the Fig. 4.8. The target imaged was a printed letter "e" on a piece of white paper. The left picture of Fig. 4.8 shows the orignal target. During the imaging process, the focused laser scanned the surface of the letter. And the step size was 20 μm. The right picture of Fig. 4.8 is the PAM image of the letter.

4.3   Preliminary in-vivo imaging experiment

Using the transparent ultrasound transducer developed in this research, an in vivo photoacoustic image of a mouse ear was obtained by researchers in Washington university, Saint Louis. It is shown in Fig. 4.9. These preliminary results demonstrated the feasibility of applying the transparent ultrasound transducer to PAM systems.
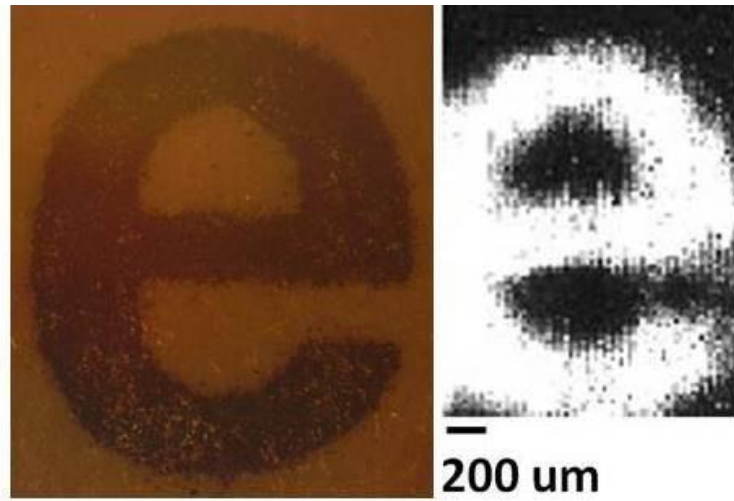
Fig. 4.8. First transparent ultrasound transducer based photoacoustic image:original

image (left); photoacoustic image (right).
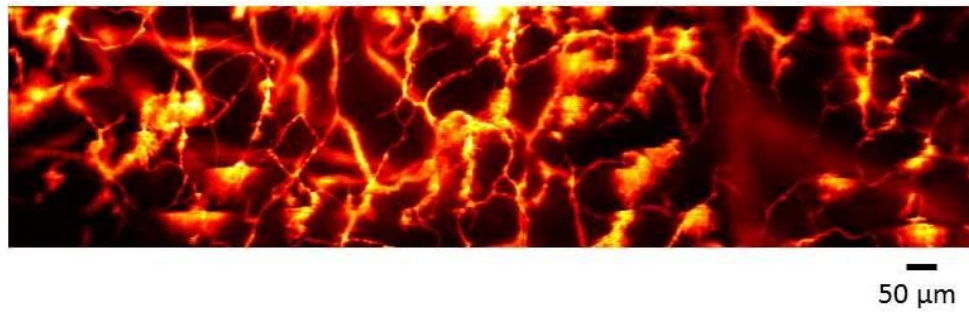
(a)

Fig. 4.9. Photoacoustic image of the mouse brain tissue: (a) full view (b) zoom-in view

showing the microscopy structures.

(b)
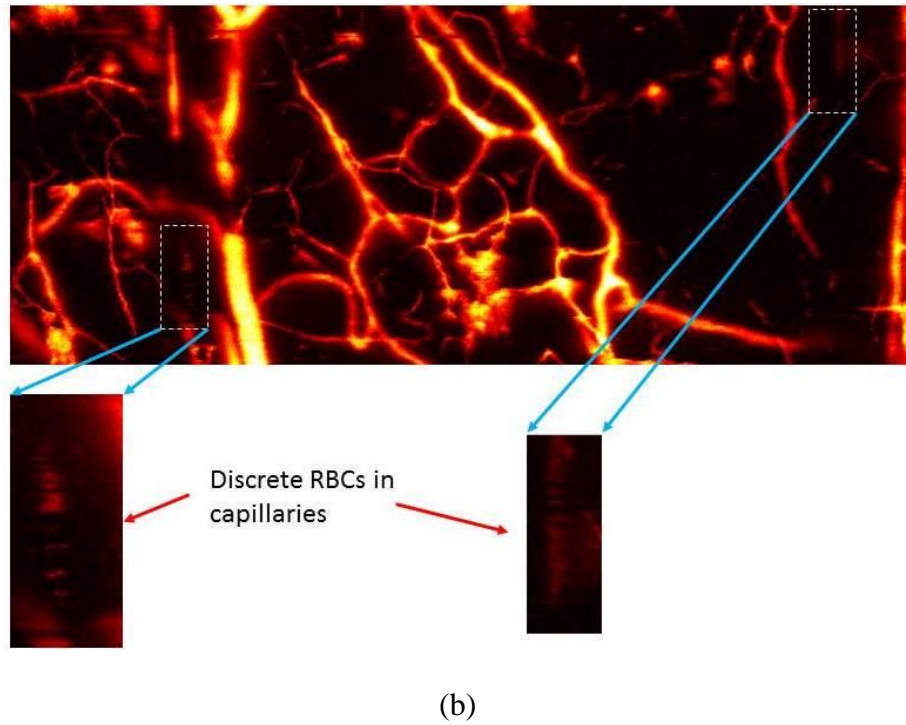
Fig. 4.9. Continued.

The full view of the photoacoustic image of a piece of mouse brain tissue is shown in Fig. 4.9(a). In the image, micro features (blood vessels) in the tissue could be clearly seen. The blood vessels with bigger diameters could also be distinguished in the background of the image. A zoom-in view of part of the full view image is shown in Fig. 4.9(b). Though zooming in, the discrete red blood cells (RBCs) could be observed in the capillaries. The results demonstrated the microscopy capability of this PAM system.

PAM imaging tests were also conducted on mouse ear tissues. Fig. 4.10. shows the PAM images of a piece of mouse ear tissue. The photoacoustic imaging head in the setup scanned across the surface of the mouse ear tissue. The scan step size was 5 μm.

The field view of this image was 1 mm by 1 mm. The illumination pulse laser was a 570

nm pulse laser.
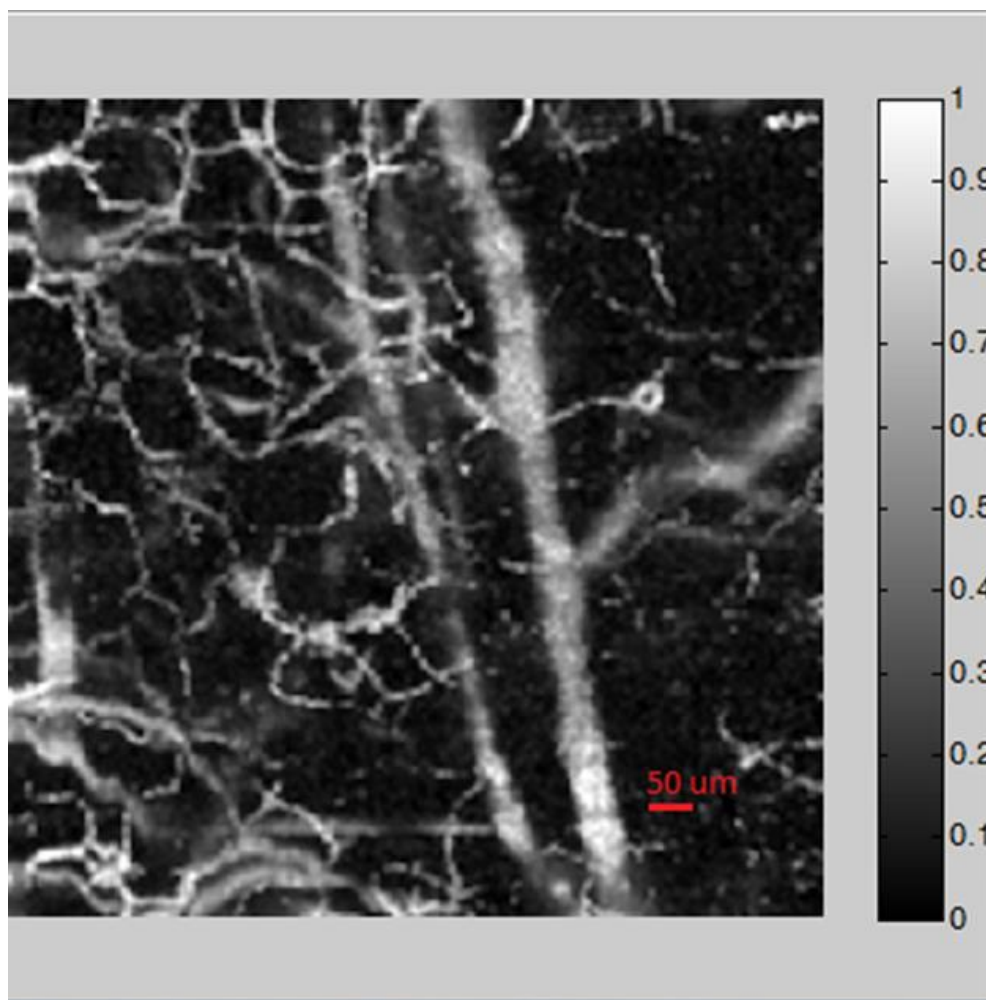
(a)

Fig. 4.10. PAM images of a pieces of mouse ear tissue: (a)without average processing;

(b) after 16 times average processing.
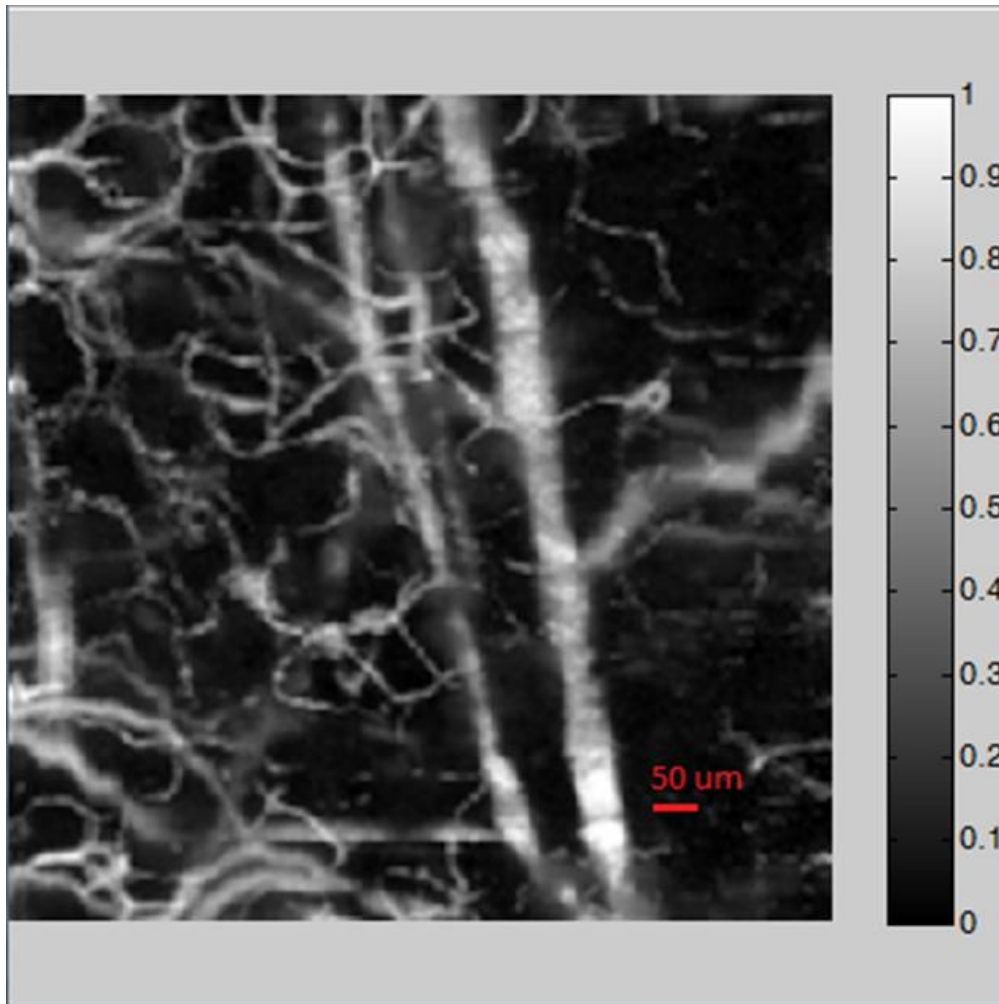
(b)

Fig. 4.10. Continued.

From Fig. 4.10(b) it can be seen that after 16 times average processing, the signal to noise ratio (SNR) of the image was improved. The relationship between average times and the SNRs of the image is shown in Fig. 4.11. With more average times, the noise in the image could be suppressed significantly. However, at the same time, some micro features in the image were missing.
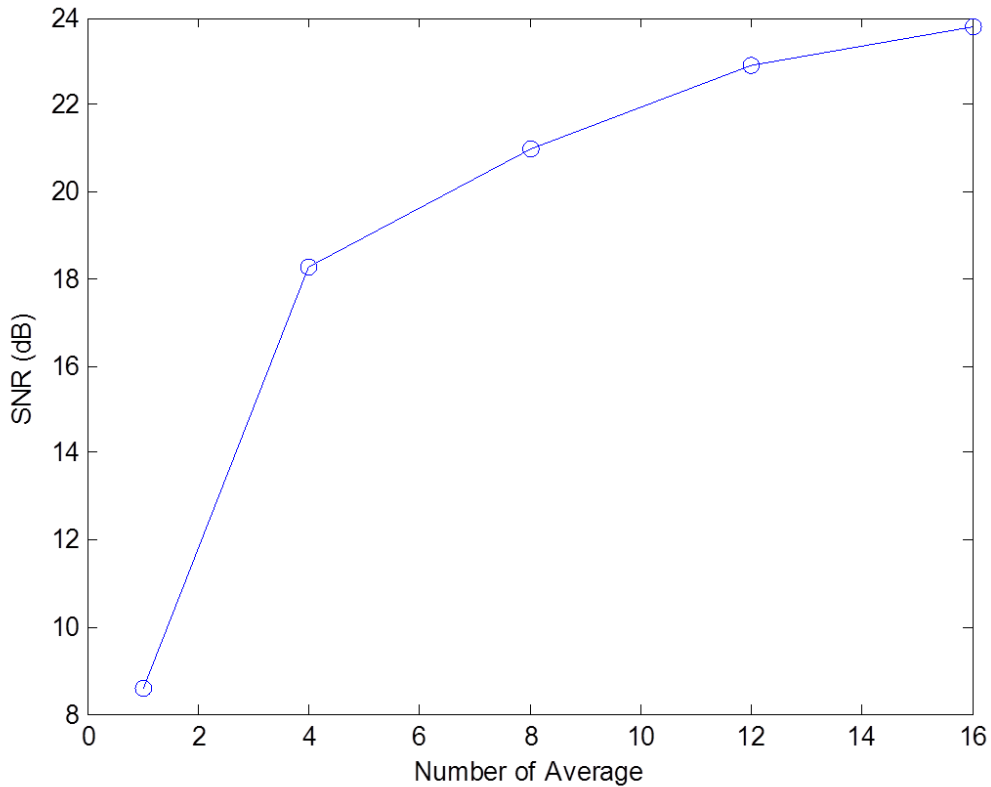
Fig. 4.11. SNR of the photoacoustic image vs. number of average times.

4.4   Summary

A PAM system based on transparent ultrasound transducers was developed. Its imaging performance such as resolution, field of view, and sensitivity uniformity were quantified. In order to verify the feasibility of applying the system to photoacoustic imaging field, animal tissues were imaged using this system. The results proved that the system could be used to conduct photoacoustic microscopy studies on real biomedical samples. In the next section, another popular photoacoustic imaging technique: PAT was studied through using transparent ultrasound transducers.

5. PHOTOACOUSTIC TOMOGRAPHY USING 1D TRANSPARENT PVDF ULTRASOUND TRANSDUCER ARRAY

5.1 Imaging system setup

5.1.1 1D transparent PVDF ultrasound transducer array

Current 1D PAT array probes usually consist of a linear 1D ultrasound transducer array. In this research, a PAT array probe using a curvature 1D ultrasound transducer array was proposed. A diagram showing the geometric configuration of the 1D PAT array probe is Fig. 5.1.
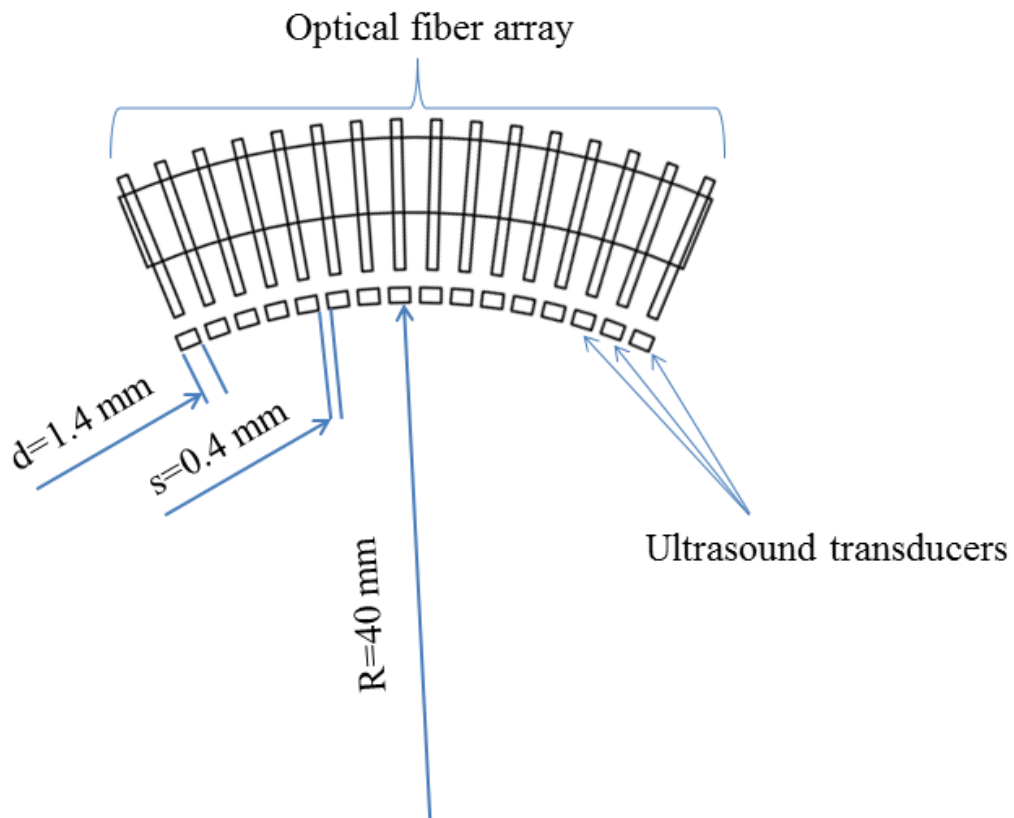
Fig. 5.1. The geometric configuration diagram of the 1D PAT array.

The 1D PAT array consisted of 16 transducer elements. They were uniformly distributed on the edge of a virtual circle whose radius was 40 mm. The width of each transducer element was 1.4 mm, and the spacing between neighboring elements was 0.4 mm. The curvature geometric shape of 1D PAT array helped focus more illumination laser energy to the imaged target, which would improve the strength of the photoacoustic signal.

Behind the transducer elements, there was an array of optical fibers. The direction of each optical fiber was normal to the transducer element in front of it. Pulse laser illumination was delivered through these optical fibers. Since the transducers were transparent, the pulse laser from the optical fibers would shoot through the transducers to the target. Compared with other 1D PAT arrays which used oblique illumination pulse lasers, this laser delivery method improved the efficiency of the pulse laser. The optical fibers were also uniformly distributed on the edge of a circle whose center was same to the virtual circle mentioned in the above description.

The configuration of the whole 1D PAT array probe is shown in Fig. 5.2. The picture of the prototype of this 1D PAT array is shown in Fig. 5.3.
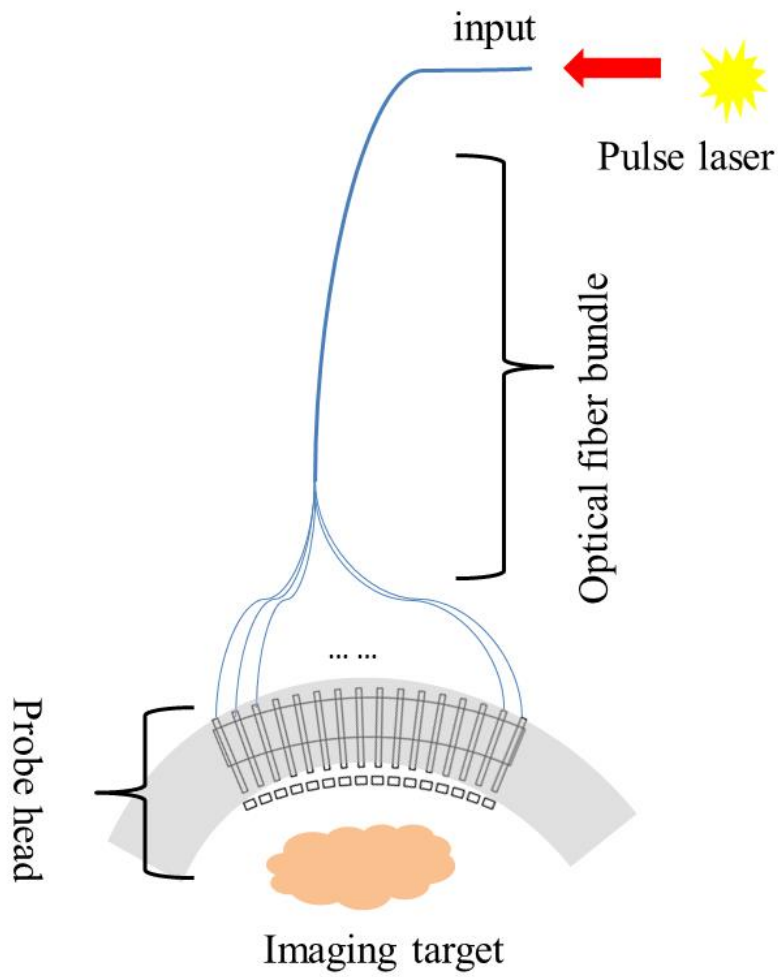
Fig. 5.2. Configuration of the 1D PAT array imaging probe.
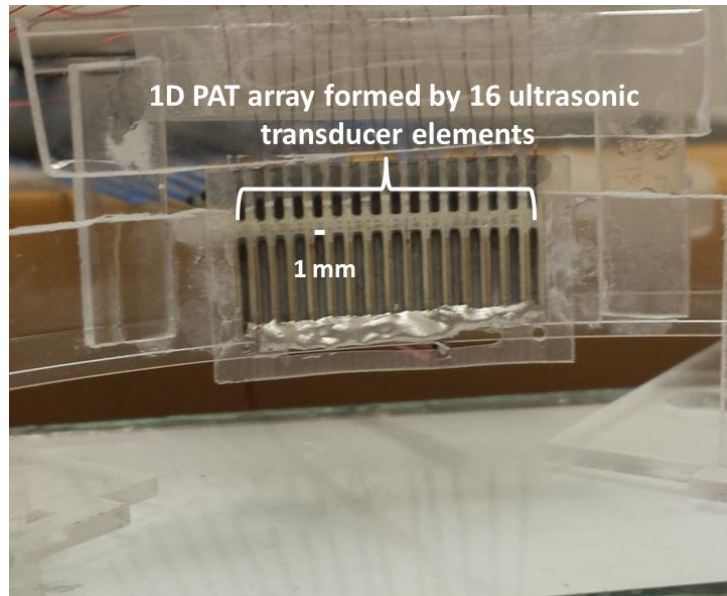
(a)

(b)

Fig. 5.3. 1D PAT array based on transparent ultrasound transducers: (1) front view; (2) top view; (3) back view.
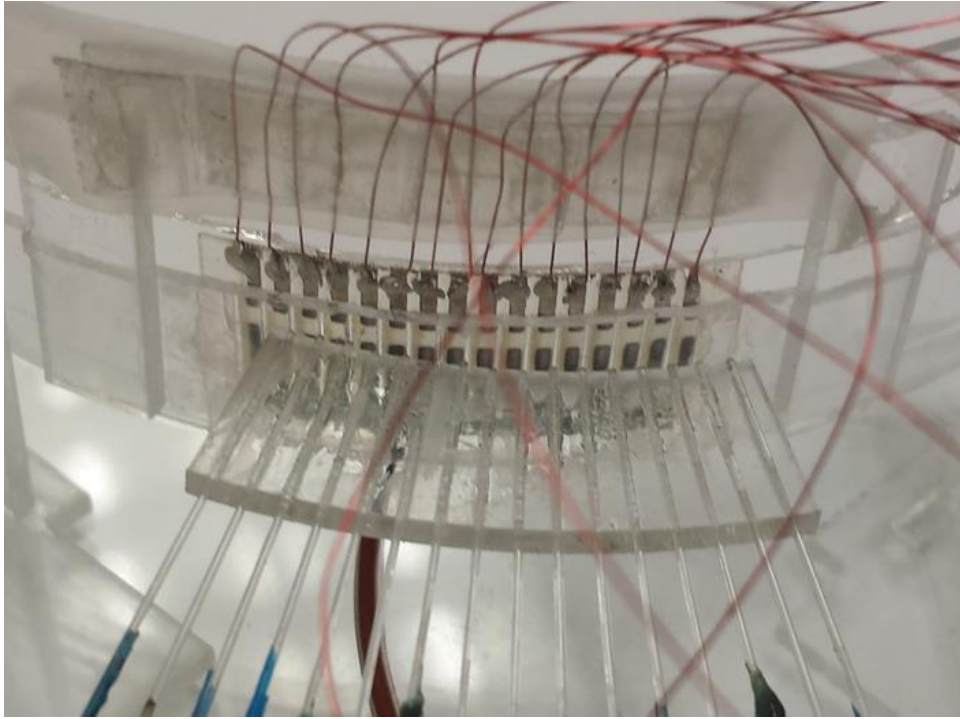
(c)

Fig. 5.3. Continued.

5.1.2   Sensitivity calibration

The 1D PAT array system based on transparent ultrasound transducers were

fabricated. After that, the transducers in the array were soldered with copper wires using

E-solder 3022 and then the array was connected to the data acquisition system through

coaxial cables (diameter: 1 mm, Hirose Electric Co., Ltd.).

During the metal and ITO deposition processes, due to the deposition variation at

different locations of the PVDF film surface, the conductivity of the electrode layers for

16 elements was not uniform. It led to sensitivity non-uniformity problems for the 16

channels. And also when the E-solder 3022 was used to connect the wires to the

electrodes of the transducers, the connection resistance varied from element to element. During the laser illumination process, since all optical fibers shoot out laser pulses at the same time, the laser light from other channels will also generate interference photoacoustic signals. Therefore, a signal sensitivity calibration measurement among the 16 channels was conducted before applying this 1D ultrasound transducer array in PAT systems.

The calibration was conducted following the procedures below. A piece of cubic agar phantom was used as the coupling medium. Its dimension was 2 mm by 2 mm by 3 mm. The thickness of this phantom was 2 mm. On one side of this cube, a piece of black tap was attached, which worked as the imaging target. The opposite side was attached to the surface of one transducer in the array (Fig. 5.4). Then a photoacoustic test was conducted on each transducer element. A black tape target was positioned in the front of each element in the array when it was tested. The pulsed laser was delivered to each element through the optical fiber bundle. The A-line photoacoustic signal was collected and the photoacoustic pulse amplitude was recorded. Using the same target, same test was done on all the 16 transducer elements. Their photoacoustic pulse amplitudes were also recorded. The results are shown in Table 5.1. Based on the above calibration results, the photoacoustic signals can be normalized for different channels.
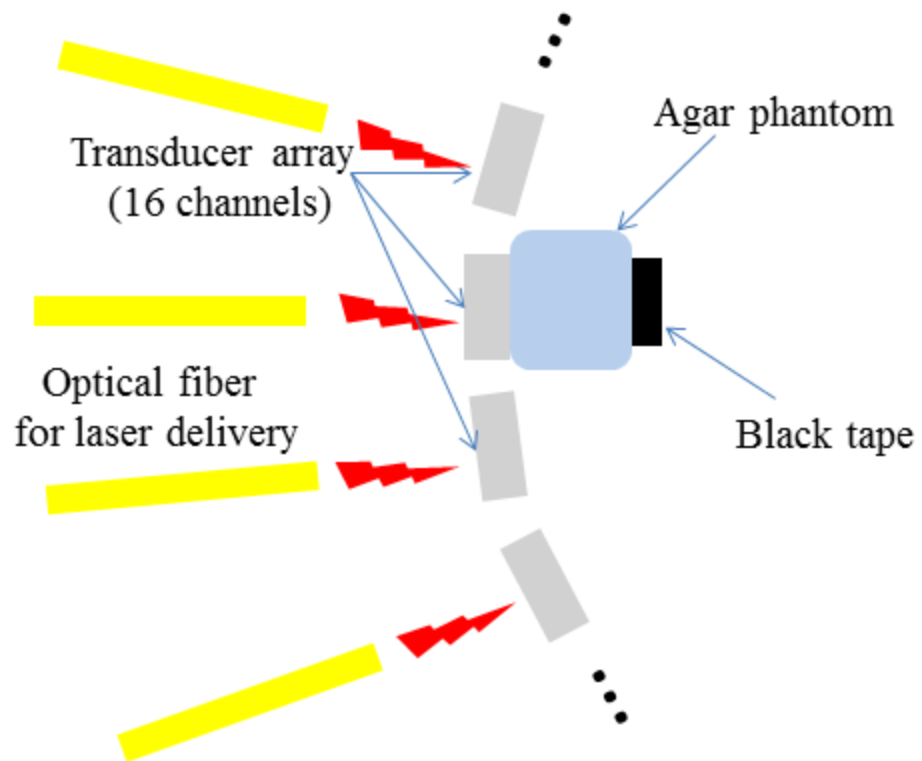
Fig. 5.4. 1D PAT array photoacoustic signal strength calibration setup.

Table 5.1. The photoacoustic pulse amplitudes of 16 channels in the 1D PAT array.

Channel Number	Photoacoustic pulse peak to peak amplitude (mV)
1	12
2	16
3	18
4	24
5	10
6	32
7	22
8	28
9	28
10	26
11	26
12	32
13	26
14	28
15	18
16	50

5.2   Image reconstruction

Using the developed 1D PAT array imaging system, B-mode photoacoustic images of different targets were obtained. In order to get high quality images which

could provide more details about the imaged targets, raw imaging data were further processed with the synthetic aperture focusing technique (SAFT).

SAFT is a classical aperture synthesis method in which one single element acts as both the transmitter and receiver on a full array [35-37]. For example, in order to synthesize an N-element ultrasound transducer array, one transducer element first transmits a short pulse at the location of the first element in the virtual array. Reflected signals are received at the same element and stored. The same process repeats at locations of all N elements, and an N-element array is synthesized. Since in SAFT only one element is fired on every measurement, the delivered acoustic power can be very small. In order to increase the acoustic power, a group of elements are fired at the same time, which leads to the multi-synthetic aperture focusing (MSAF) [38].

For the 16-element 1D ultrasound transducer array system, its imaging process is similar to the single element SAFT. During the imaging process, the laser light from the illumination fiber array shoots through the transparent ultrasound transducer array to the targets. Then the generated photoacoustic signals are received by the array. Fig. 5.5 shows the principles of the single element straight array SAFT.
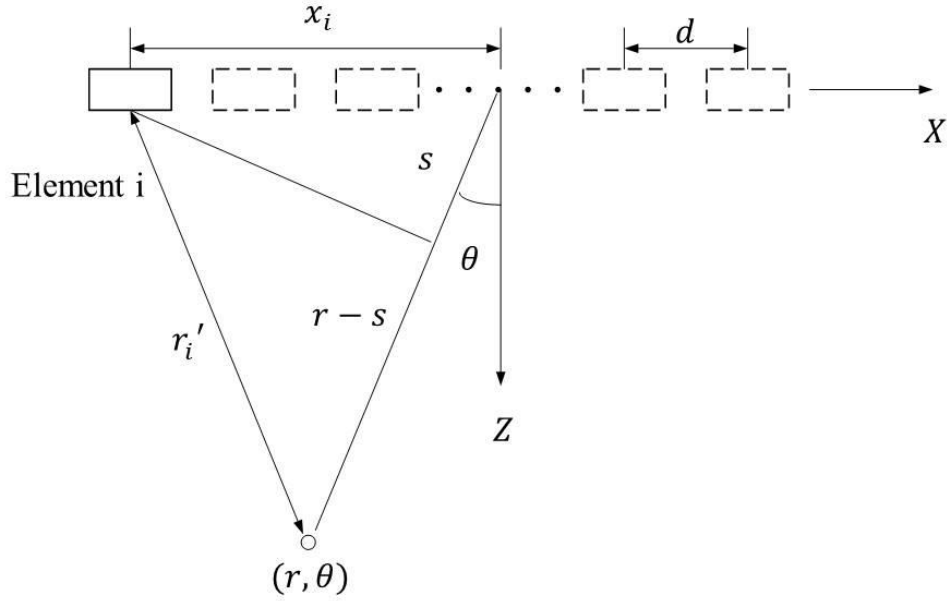
Fig. 5.5. SAFT principles of the single element straight array.

For element i, its round-trip delay is:

$$\tau_i = 2\frac{r - r_i'}{c} \quad (5.1)$$

where

$$r_i' = \sqrt{x_i^2 + r^2 - 2x_i r \sin \theta} \quad (5.2)$$

The steering delay is

$$\tau_i^s = \frac{1}{c} 2x_i \sin \theta \quad (5.3)$$

For the point (r, θ), the A-scan signal is

$$a_{SAFT}(r, \theta) = \sum_{i=0}^{N-1} s_i \left(\frac{2r}{c} - \tau_i \right) = \sum_{i=0}^{N-1} s_i(t - \tau_i) \quad (5.4)$$

where $s_i(t)$ is the signal received at the i'th element and τ_i is the beamforming delay for the i'th active element.

But for the 1D curved ultrasound transducer array, the straight ultrasound transducer array SAFT processing algorithm should be modified to adapt to the curved transducer array. Fig. 5.6 shows the geometric positions of the elements in the developed 1D PAT array.

Fig. 5.6. Geometric positions of the elements in the developed 1D PAT array

In Fig. 5.6, for element i ($i = -8, -7 \ldots - 1, 1 \ldots 7, 8,\ 16\ elements\ in\ total$), its round-trip delay is:
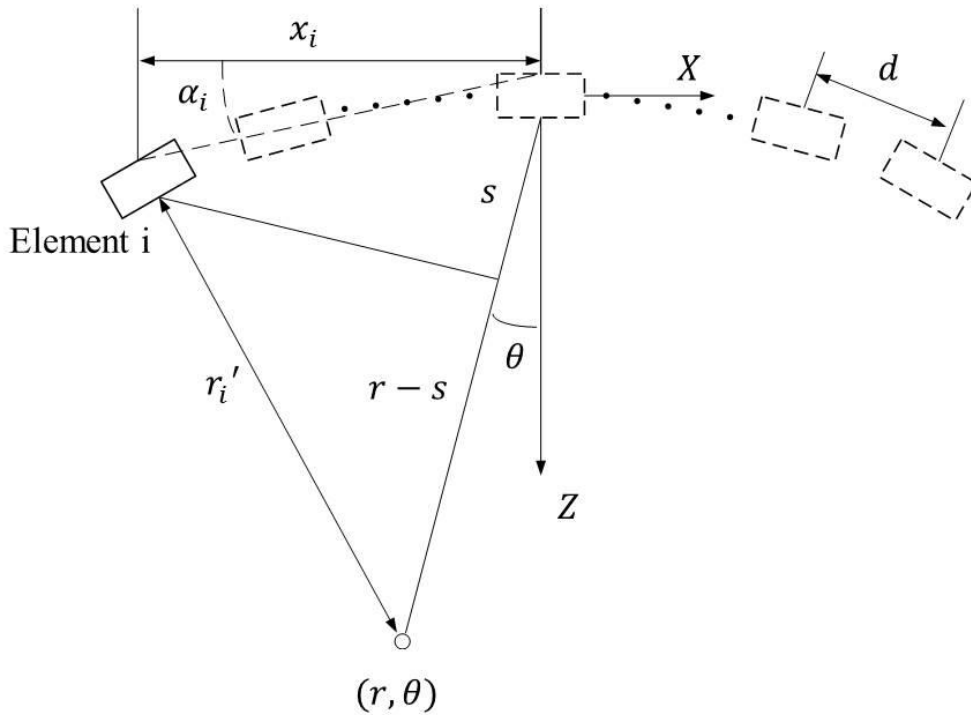
$$\tau_i = 2\frac{r - r_i{}'}{c} \quad (5.5)$$

where

$$r_i{}' = \sqrt{\frac{x_i^2}{\cos^2 \alpha_i} + r^2 - \frac{2x_i r \sin \theta}{\cos \alpha_i}} \quad (5.6)$$

Since all elements are on the edge of a circle whose radius is R = 4 cm,

$$\alpha_i = \frac{(|i| - 0.5) \cdot d}{2R} \quad (5.7)$$

The steering delay is

$$\tau_i^s = \frac{1}{c} \cdot \frac{2x_i \sin \theta}{\cos \alpha_i} \quad (5.8)$$

For the point (r, θ), the A-scan signal is

$$a_{SAFT}(r, \theta) = \sum_{i=0}^{N-1} s_i\left(\frac{2r}{c} - \tau_i\right) = \sum_{i=0}^{N-1} s_i(t - \tau_i) \quad (5.9)$$

where $s_i(t)$ is the Hilbert-transformed photoacoustic signal received at the i'th element and τ_i is the beamforming delay for the i'th active element. Based on the above analysis, for the point (r, θ) in the final image, its intensity can be calculated through the equation (5.9).

5.3 Imaging performance characterization with optical phantom

5.3.1 Spatial resolution

The resolution of a PAT image mainly include: lateral resolution and axial resolution. In order to quantify the lateral resolution, the 1D PAT array system built in the research was used to image an agar phantom containing black targets with different width (Fig. 5.7).
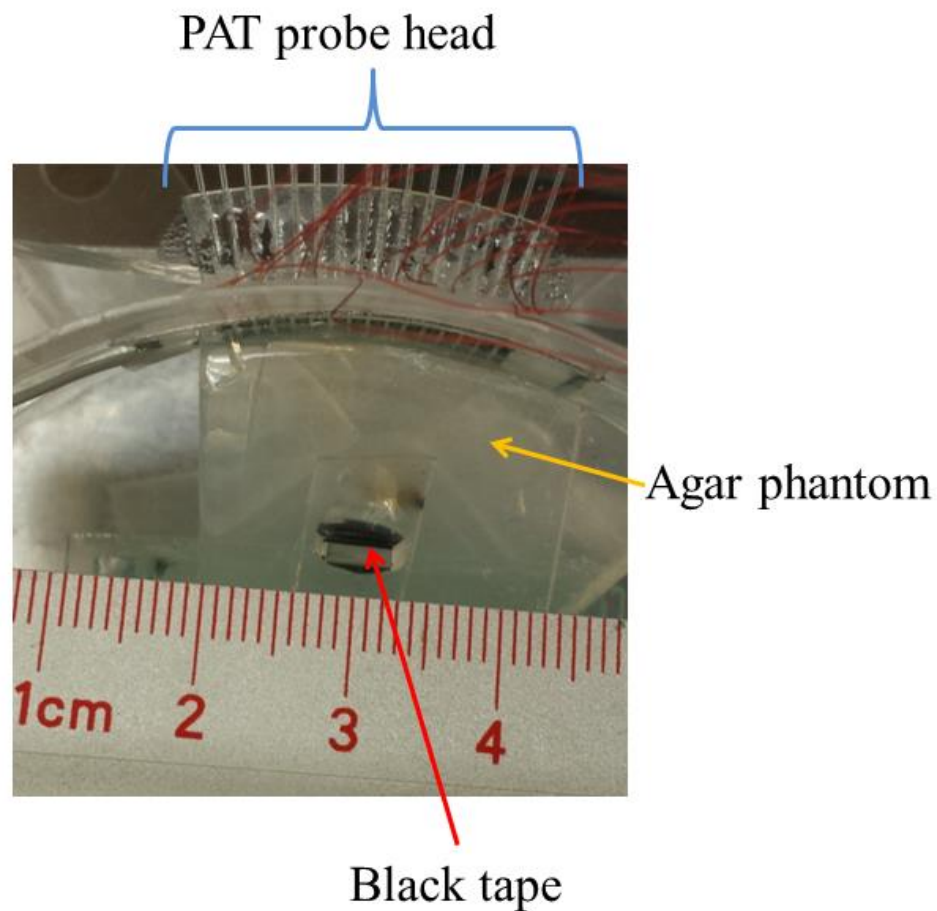

Fig. 5.7. Lateral resolution test setup.
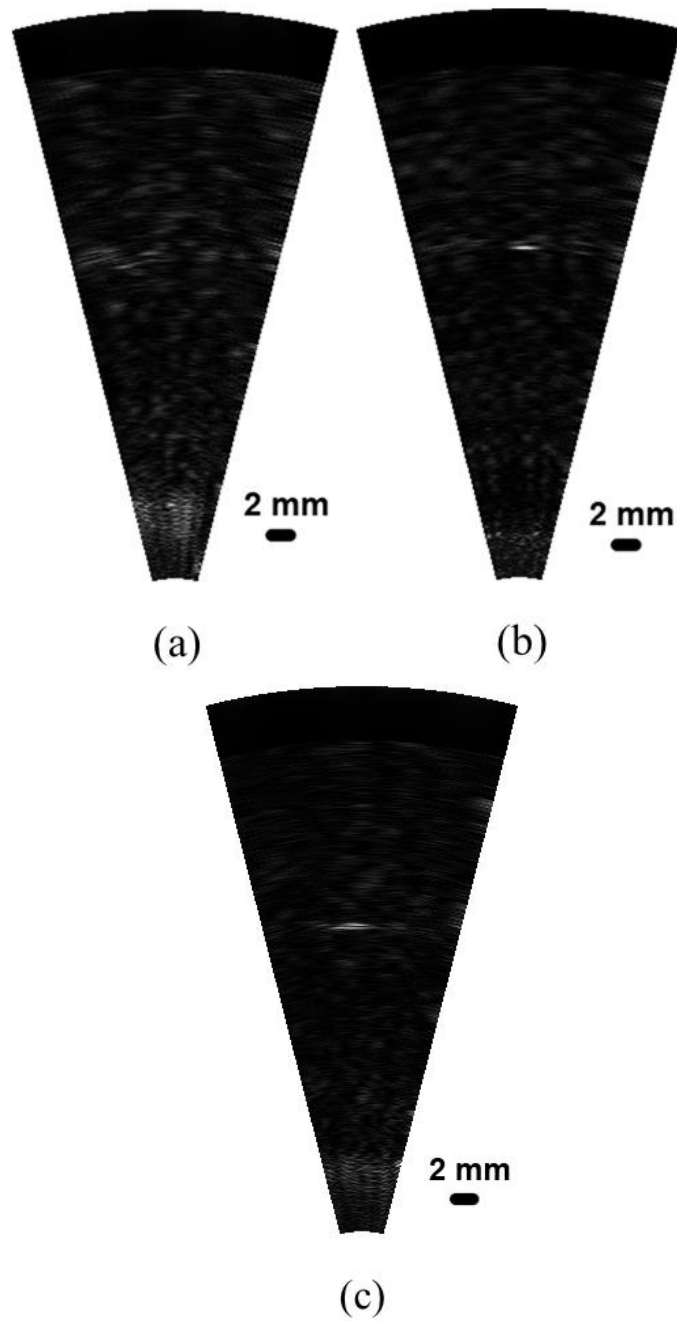
Fig. 5.8. PAT images of three black tapes with different widths: (a) 0.5 mm; (b) 1.0 mm;

(c) 2.0 mm.

The widths of the black tapes were: 0.5 mm, 1 mm and 2 mm. The PAT images of the above 4 targets are shown in the Fig. 5.8.

From the three PAT images it can be seen that if the width of the black tape was smaller than 1 mm, there was no observable object in the PAT image. Above the 1 mm, the objects could be seen in the PAT images. Therefore, the lateral resolution of the PAT imaging array was around 1 mm.

The axial resolution of a 1D PAT array system is determined by the shortest photoacoustic pulse width that could be detected by the transducer element in the array. In order to get this value, the A-line images of one element of the 1D PAT array were obtained and compared. The results are shown in Fig. 5.9. From these results, it can be seen that the shortest photoacoustic pulse width was about 0.1 us. Since the acoustic velocity in agar is about 1500m/s, the axial resolution of the 1D PAT array system was about 1.5 mm.
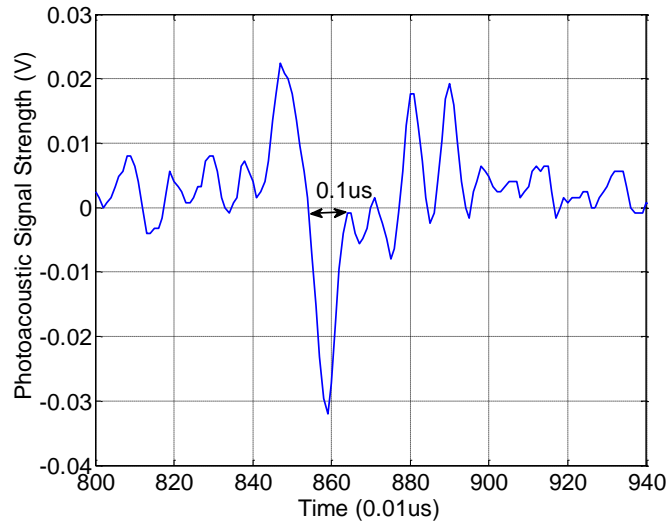
Fig. 5.9. Width of the photoacoustic pulse detected by the 1D PAT array.

5.3.2   Contrast to noise ratio

The contrast to noise ratio (CNR) of the PAT imaging array was measured

through the following test. Three agar phantoms embedded by a small piece of black

tape were made. The black tapes were embedded at different depths: 10 mm, 15 mm and

20 mm. Then they were imaged by the PAT imaging array system. The results are shown

in Fig. 5.10. The CNR was calculated using the following equation:

$$CNR = \frac{|S_A - S_B|}{\sigma_0} \quad (5.10)$$

where S_A is the intensity of the interested region, S_B is the intensity of the background

region and σ_0 is the standard deviation of the background noise level.

94

In the agar phantom, the CNR of the PAT images reached the maximum around the depth 15 mm. Above 15 mm, the image contrast gradually decreased. Table 5.3 shows the CNRs of agar phantom PAT images with targets embedded at different depths.
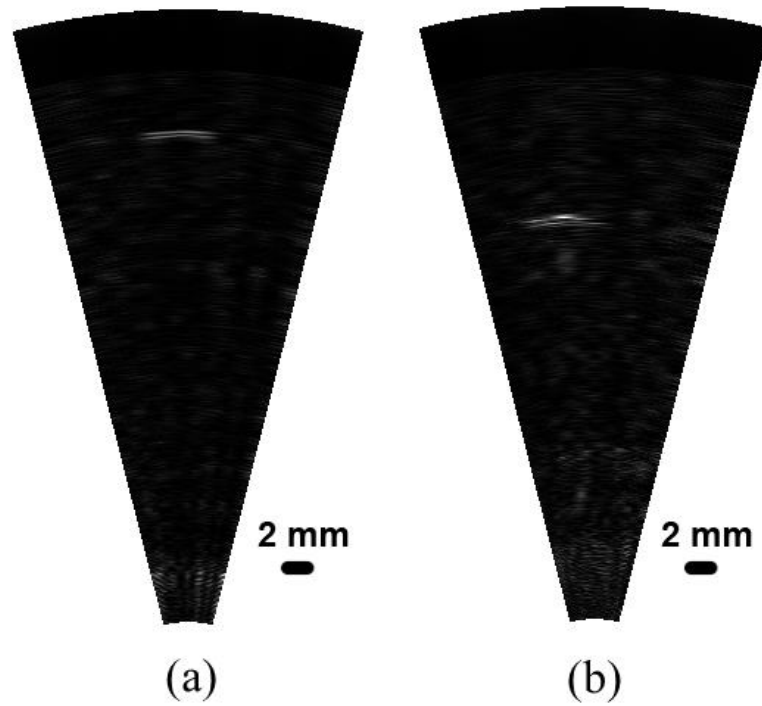
Fig. 5.10. 1D PAT array CNR test results. Targets depths in the phantoms: (a)10 mm; (b)15 mm; (c)20 mm.

(c)
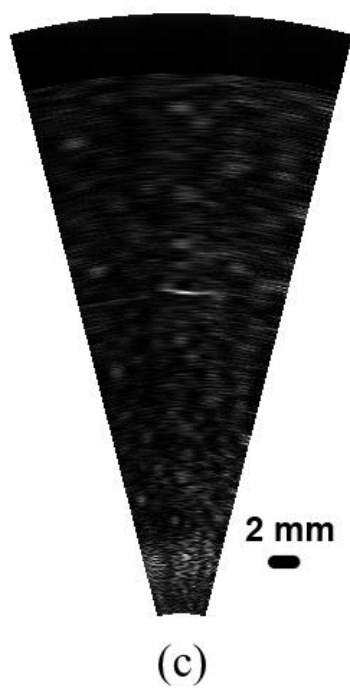
Fig. 5.10. Continued.

Table 5.2. CNR values of agar phantom PAT images with targets embedded at different depths.

Depth of the target in the phantom (mm)	CNR (dB)
5	26.80
10	32.20
15	35.01
20	13.70

5.4   Preliminary ex-vivo imaging experiment

The developed 1D PAT imaging array system has been used to image chicken breast targets. A piece of chicken breast with black tapes was used as a tumor mimicking phantoms for the PAT imaging experiements. The test setup is shown in Fig. 5.11. The black tape was embedded at different depths in the chicken breast. The PAT images of these phantoms show the imaging sensitivity of this PAT imaging system at different depths in real animal tissues.

Fig. 5.11. Setup for chicken breast tissue PAT imaging experiments.

Fig. 5.12. PAT images of black tape-embedded chicken breast samples with different

embedded depths: a) 3 mm; b) 4 mm; c) 7 mm.

b)

4 mm

4 mm

Imaging Target

2 mm

PAT image

c)

7 mm

4 mm

Imaging Target

2 mm
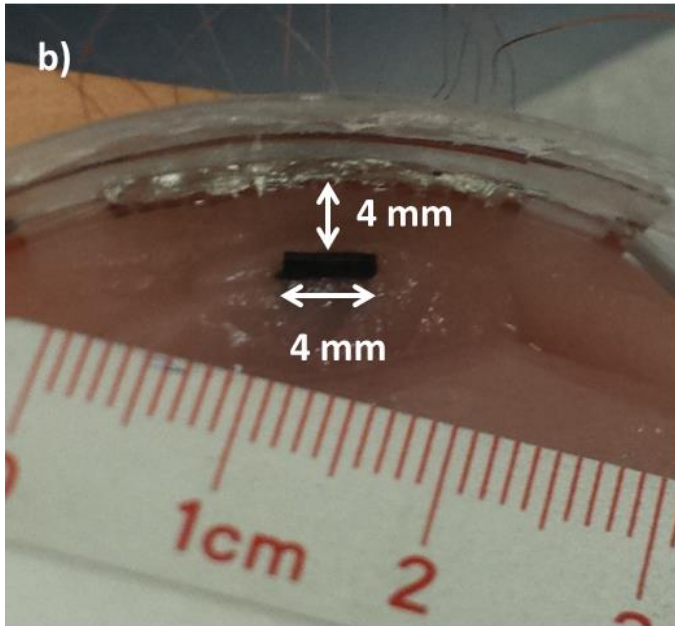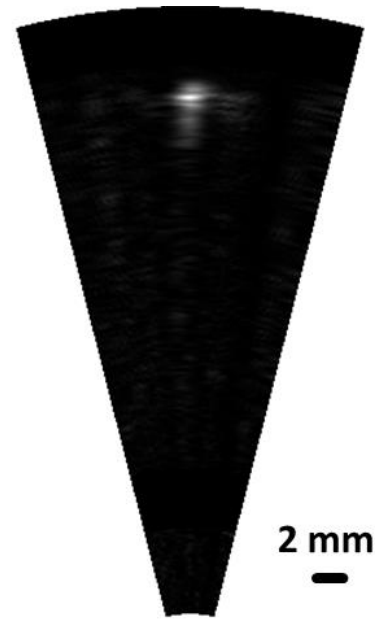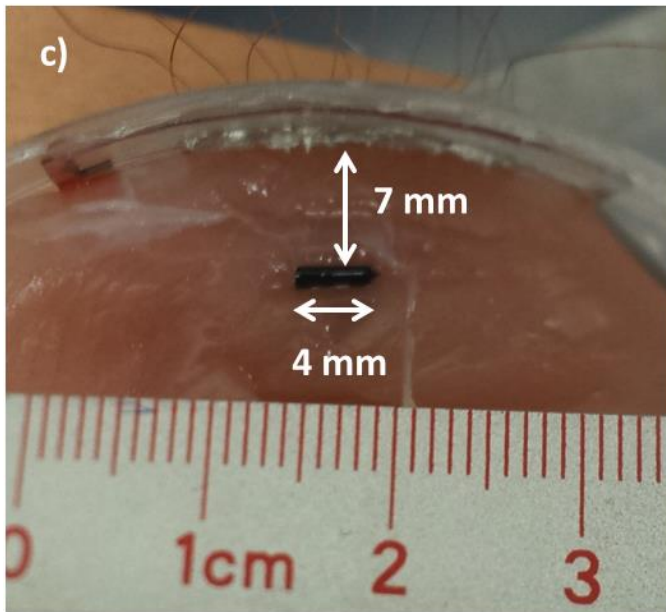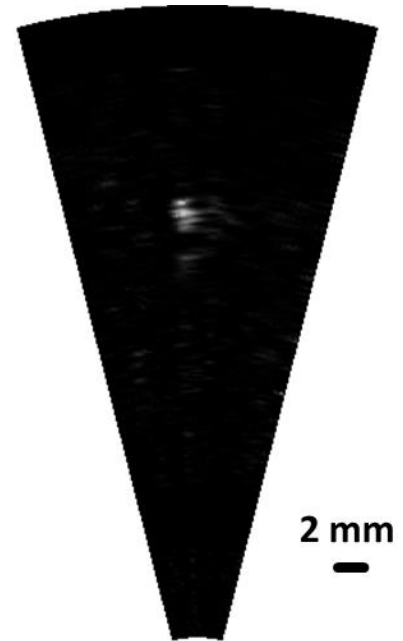
PAT image

Fig. 5.12. Continued.

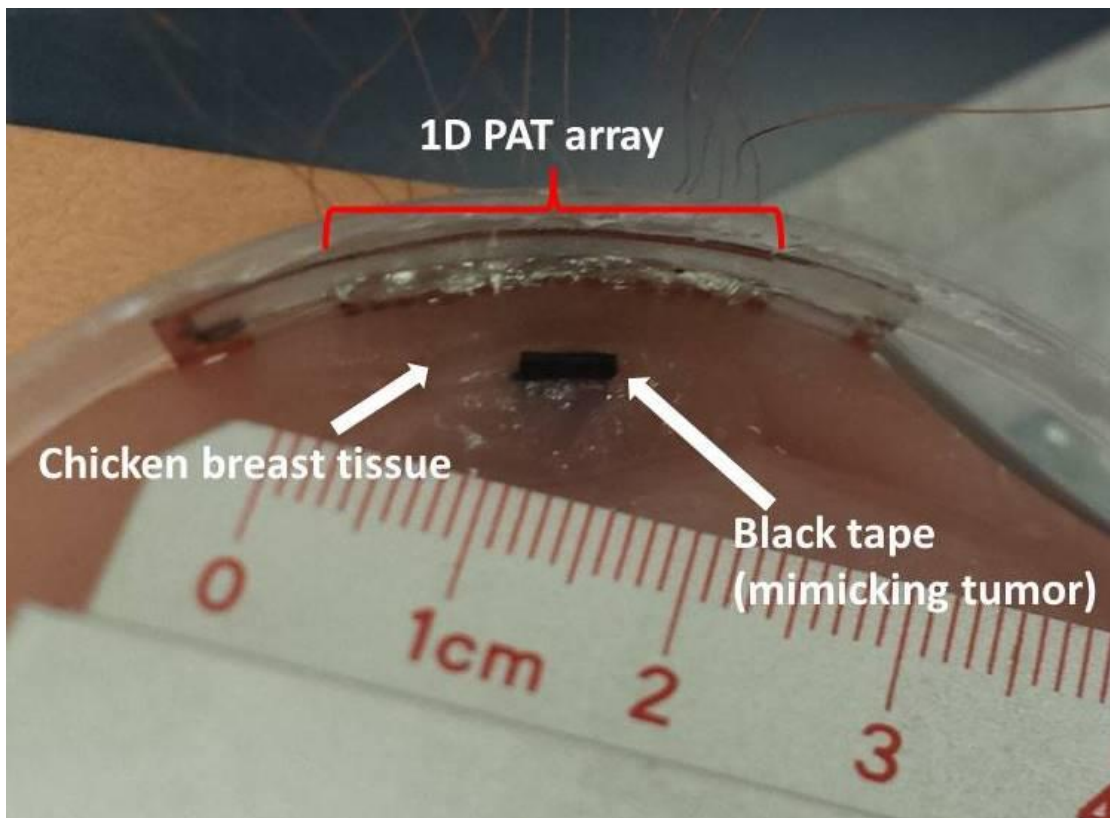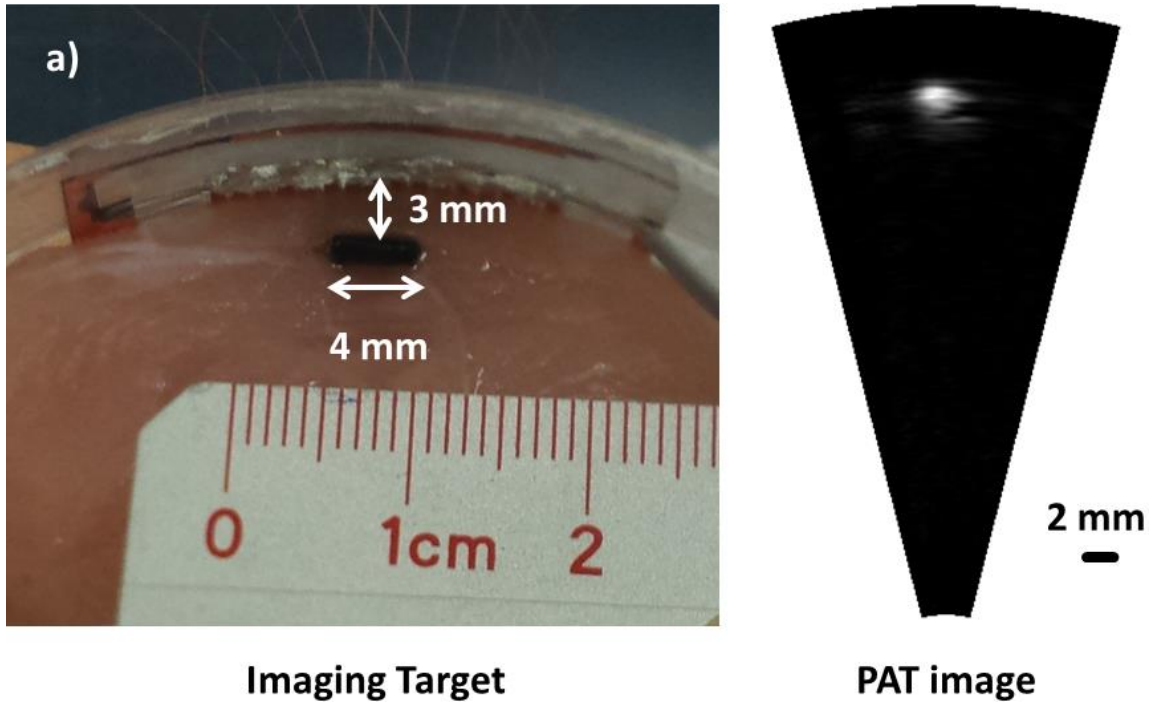Fig. 5.12 shows the PAT images of the black tapes at different depths of the chicken breast tissue. As the depth increased from 3 mm to 7 mm, the intensity of black tape's region in the PAT images decreased. And also, the image distortion became more significant. The black tape's image gradually lost its original shape. As the depth increased, on the one side, the intensity of the illumination light reaching the black tape became weaker due to the scattering in the tissue. And on the other side, the photoacoustic signal also attenuated during the transmission from the black tape to the PAT array. The CNR of these three images all decreased as the black tape's depth increased. Table 5.3. shows the CNRs of these three images. Fig. 5.13 shows the image CNR trend of these PAT images as the embedded depth increases.

Table 5.3. CNR values of three chicken breast PAT images

Depth of the black tape in the chicken breast tissue (mm)	CNR (dB)
3	52.29
4	48.31
7	39.20
15	11.64
20	3.09
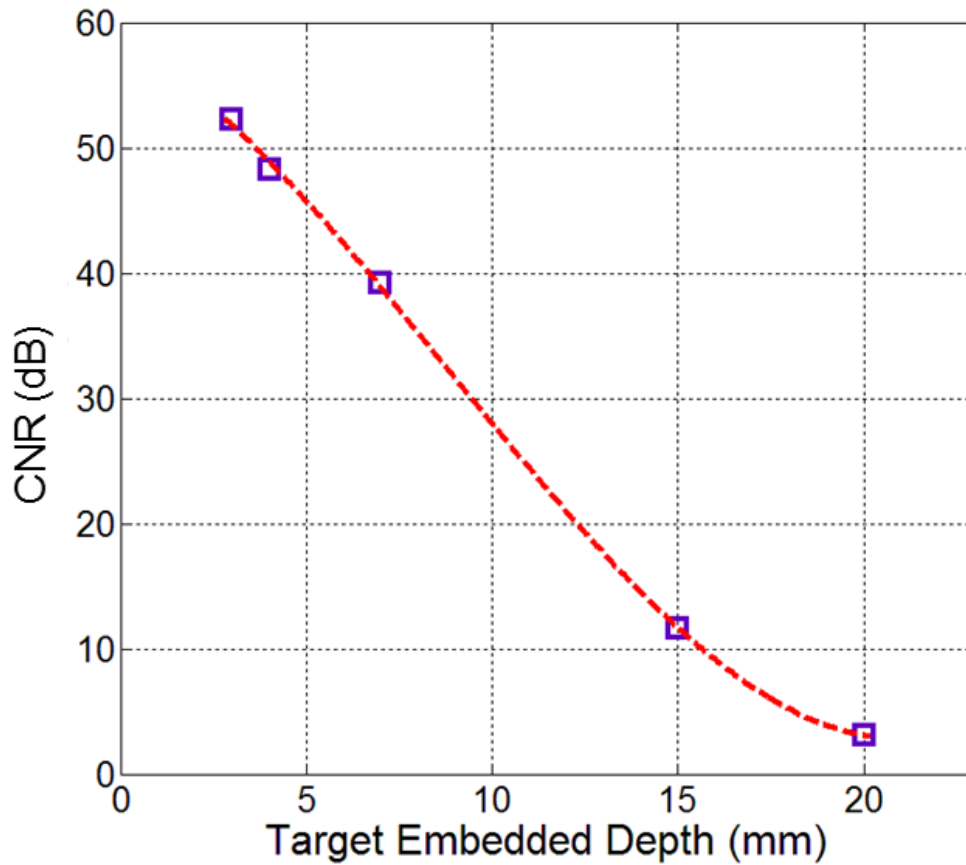
Fig. 5.13. CNR of PAT images of black tape-embedded chicken breast tissues.

5.5   Summary

In this section, a 1-D PAT array imaging system was developed using PVDF transparent ultrasound transducers. The design and fabrication process were introduced first. In order to build an accurate image reconstruction algorithm, SAFT image improvement method was modified based on the features of this 1-D PAT array imaging system. The 1-D PAT array imaging system was used to get PAT images of agar phantoms and also animal tissues. The imaging capabilities of this system were quantified.

6. CONCLUSIONS

In this study, microfabricated PVDF transparent ultrasound transducers for both PAM and PAT have been developed. The bulky traditional PAM and PAT systems have been simplified using the transparent ultrasound transducers. PAM and PAT imaging experiments on both optical phantoms and animal tissues have been conducted. The results demonstrated the capabilities of the new PAM and PAT array imaging systems.

PVDF was selected as the active element material of the transparent ultrasound transducers. Two methods have been developed for fabricating this new type of transducers by using PVDF piezoelectric films and PVDF precursors, respectively. The electronic properties of the developed ultrasound transducers have been measured and studied. Due to the high electrical impedance of PVDF piezoelectric films, two electric impedance matching methods between PVDF transducer and the signal acquisition system have been developed and tested with different PVDF transparent transducers. The test results lay a foundation for the photoacoustic imaging system design based on PVDF transparent transducers in the future.

For the application of this new technology, a PAM system based on the transparent ultrasound transducer has been developed. Compared with traditional PAM systems using general ultrasound transducers, the developed PAM system had a wider imaging view field and smaller and simpler imaging head. The illumination pulse laser could excite the target in the normal direction instead of in the oblique direction, which improved the efficiency of the laser energy delivery. Photoacoustic imaging experiments

based on this PAM system have been conducted on a mouse brain tissue, which showed many micro features, for instance blood vessels, in the tissue.

The second application of the developed transparent transducer is in 1D PAT array imaging system. The PAT array imaging system developed in this research has been used in lab-made phantom and real animal tissues imaging experiments. The results demonstrated its capabilities on fast PAT imaging applications.

Through the development and studies on PVDF transparent ultrasound transducers in this research, a novel solution was established for improving the current photoacoustic related imaging systems. It provided a new concept on building ultrasound transducers especially for photoacoustic imaging applications.

REFERENCES

[1] Wang, Lihong V., and Song Hu. "Photoacoustic tomography: in vivo imaging from organelles to organs." *Science* 335.6075 (2012): 1458-1462.

[2] Wang, Lihong V. "Tutorial on photoacoustic microscopy and computed tomography." *Selected Topics in Quantum Electronics, IEEE Journal of* 14.1 (2008): 171-179.

[3] Wang, Lihong V. "Multiscale photoacoustic microscopy and computed tomography." *Nature photonics* 3.9 (2009): 503-509.

[4] Kim, Chulhong, Christopher Favazza, and Lihong V. Wang. "In vivo photoacoustic tomography of chemicals: high-resolution functional and molecular optical imaging at new depths." *Chemical reviews* 110.5 (2010): 2756-2782.

[5] Esenaliev, Rinat O., Alexander A. Karabutov, and Alexander A. Oraevsky. "Sensitivity of laser opto-acoustic imaging in detection of small deeply embedded tumors." *Selected Topics in Quantum Electronics, IEEE Journal of* 5.4 (1999): 981-988.

[6] Viator, John A., Steven L. Jacques, and Scott A. Prahl. "Depth profiling of absorbing soft materials using photoacoustic methods." *Selected Topics in Quantum Electronics, IEEE Journal of* 5.4 (1999): 989-996.

[7] Li, Changhui, and Lihong V. Wang. "Photoacoustic tomography and sensing in biomedicine." *Physics in medicine and biology* 54.19 (2009): R59.

[8] Yao, Junjie, and Lihong V. Wang. "Photoacoustic tomography: fundamentals, advances and prospects." *Contrast media & molecular imaging* 6.5 (2011): 332-345.

[9] Xu, Minghua, and Lihong V. Wang. "Photoacoustic imaging in biomedicine."*Review of scientific instruments* 77.4 (2006): 041101.

[10] Zhang, Hao F., Konstantin Maslov, George Stoica, and Lihong V. Wang. "Functional photoacoustic microscopy for high-resolution and noninvasive in vivo imaging." *Nature biotechnology* 24.7 (2006): 848-851.

[11] Hu, Song, Konstantin Maslov, and Lihong V. Wang. "Second-generation optical-resolution photoacoustic microscopy with improved sensitivity and speed." *Optics letters* 36.7 (2011): 1134-1136.

[12] Maslov, Konstantin, Hao F. Zhang, Song Hu, and Lihong V. Wang. "Optical-resolution photoacoustic microscopy for in vivo imaging of single capillaries." *Optics letters* 33.9 (2008): 929-931.

[13] Wang, Xueding, Yongjiang Pang, Geng Ku, Xueyi Xie, George Stoica, and Lihong V. Wang. "Noninvasive laser-induced photoacoustic tomography for structural and functional in vivo imaging of the brain." *Nature biotechnology* 21.7 (2003): 803-806.

[14] Song, Liang, Chulhong Kim, Konstantin Maslov, K. Kirk Shung, and Lihong V. Wang. "High-speed dynamic 3D photoacoustic imaging of sentinel lymph node in a murine model using an ultrasound array." *Medical physics* 36.8 (2009): 3724-3729.

[15] Tang, Jianbo, Lei Xi, Junli Zhou, Hua Huang, Tao Zhang, Paul R. Carney, and Huabei Jiang. "Noninvasive high-speed photoacoustic tomography of cerebral

hemodynamics in awake-moving rats." *Journal of Cerebral Blood Flow & Metabolism* 35.8 (2015): 1224-1232.

[16] Zhou, Qifa, Sienting Lau, Dawei Wu, and K. Kirk Shung. "Piezoelectric films for high frequency ultrasonic transducers in biomedical applications." *Progress in materials science* 56.2 (2011): 139-174.

[17] Zhou, Q. F., J. Cannata, and K. Kirk Shung. "Design and modeling of inversion layer ultrasonic transducers using LiNbO$_3$ single crystal."*Ultrasonics* 44 (2006): e607-e611.

[18] Zhou, Q. F., K. K. Shung, Q. Zhang, and F. T. Djuth. "High frequency piezoelectric micromachined ultrasonic transducers for imaging applications." *Defense and Security Symposium*. International Society for Optics and Photonics, 2006.

[19] Guo, Hongkai, Jonathan M. Cannata, Qifa Zhou, and K. Kirk Shung. "Design and fabrication of broadband graded ultrasonic transducers with rectangular kerfs." *Ultrasonics, Ferroelectrics, and Frequency Control, IEEE Transactions on* 52.11 (2005): 2096-2102.

[20] Li, Xiang, Wei Wu, Youngsoo Chung, Wan Y. Shih, Wei-Heng Shih, Qifa Zhou, and K. Kirk Shung. "80-MHz intravascular ultrasound transducer using PMN-PT free-standing film." *IEEE transactions on ultrasonics, ferroelectrics, and frequency control* 58.11 (2011): 2281-2288.

[21] "Piezo film sensors technical manual." *Measurement Specialties, Inc.,* Norristown, PA 19403, figure 1, page 1 (1999).

[22] Sherar, M. D., and F. S. Foster. "The design and fabrication of high frequency poly (vinylidene fluoride) transducers." *Ultrasonic imaging* 11.2 (1989): 75-94.

[23] Snook, Kevin A., Jian-Zhong Zhao, Carlos HF Alves, Jonathan M. Cannata, Wo-Hsing Chen, Richard J. Meyer Jr, Timothy A. Ritter, and K. Kirk Shung. "Design, fabrication, and evaluation of high frequency, single-element transducers incorporating different materials."*Ultrasonics, Ferroelectrics, and Frequency Control, IEEE Transactions on*49.2 (2002): 169-176.

[24] Park, Youn Jung, Yong Soo Kang, and Cheolmin Park. "Micropatterning of semicrystalline poly (vinylidene fluoride)(PVDF) solutions." *European Polymer Journal* 41.5 (2005): 1002-1012.

[25] Xiang, Dan, N. N. Hsu, and G. V. Blessing. "The design, construction and application of a large aperture lens-less line-focus PVDF transducer."*Ultrasonics* 34.6 (1996): 641-647.

[26] Zheng, X. R., P. T. Lai, B. Y. Liu, Bin Li, and Y. C. Cheng. "An integrated PVDF ultrasonic sensor with improved sensitivity using polyimide." *Sensors and Actuators A: Physical* 63.2 (1997): 147-152.

[27] Wang, Yi-Chun, Ching-Hung Huang, Yung-Chun Lee, and Ho-Hsun Tsai. "Development of a PVDF sensor array for measurement of the impulsive pressure generated by cavitation bubble collapse." *Experiments in fluids* 41.3 (2006): 365-373.

[28] Lee, Seongkuk, Evgueni V. Bordatchev, and Marco JF Zeman. "Femtosecond laser micromachining of polyvinylidene fluoride (PVDF) based piezo films." *Journal of Micromechanics and Microengineering* 18.4 (2008): 045011.

[29] Tuna, Ocal, Yusuf Selamet, Gulnur Aygun, and Lutfi Ozyuzer. "High quality ITO thin films grown by dc and RF sputtering without oxygen." *Journal of Physics D: Applied Physics* 43.5 (2010): 055402.

[30] Capineri, Lorenzo, Leonardo Masotti, Marco Rinieri, and Santina Rocchi. "Ultrasonic transducers as a black-box: equivalent circuit synthesis and matching network design." *Ultrasonics, Ferroelectrics, and Frequency Control, IEEE Transactions on* 40.6 (1993): 694-703.

[31] Kim, Hyeoungwoo, Shashank Priya, Harry Stephanou, and Kenji Uchino. "Consideration of impedance matching techniques for efficient piezoelectric energy harvesting." *Ultrasonics, Ferroelectrics, and Frequency Control, IEEE Transactions on* 54.9 (2007): 1851-1859.

[32] Toda, Minoru, and Mitchell Thompson. "Novel multi-layer polymer-metal structures for use in ultrasonic transducer impedance matching and backing absorber applications." *Ultrasonics, Ferroelectrics, and Frequency Control, IEEE Transactions on* 57.12 (2010): 2818-2827.

[33] Pangraz, S., and W. Arnold. "Bandwidth of inhomogeneously polarized PVDF-films and their use in the design of efficient ultrasonic transducers."*Ferroelectrics* 93.1 (1989): 251-257.

[34] Hu, S., R. Sohn, Z-H. Lu, B. Soetikno, Q. Zhong, J. Yao, K. Maslov, J. M. Arbeit, and L. V. Wang. "Multi-contrast photoacoustic microscopy." *SPIE BiOS*. International Society for Optics and Photonics, 2012.

[35] Karaman, Mustafa, Pai-Chi Li, and Matthew O'Donnell. "Synthetic aperture imaging for small scale systems." *Ultrasonics, Ferroelectrics, and Frequency Control, IEEE Transactions on* 42.3 (1995): 429-442.

[36] Doctor, S. R., T. E. Hall, and L. D. Reid. "SAFT—the evolution of a signal processing technology for ultrasonic testing." *NDT international* 19.3 (1986): 163-167.

[37] Schickert, Martin, Martin Krause, and Wolfgang Müller. "Ultrasonic imaging of concrete elements using reconstruction by synthetic aperture focusing technique." *Journal of Materials in Civil Engineering* 15.3 (2003): 235-246.

[38] Bercoff, J., M. Tanter, L. Sandrin, S. Catheline, and M. Fink. "Ultrafast compound imaging for 2D displacement vector measurements: Application to transient elastography and color flow mapping." *Ultrasonics Symposium, 2001 IEEE*. Vol. 2. IEEE, 2001.